UC San Diego

UC San Diego Electronic Theses and Dissertations

Title

Design and Investigation of an Optical Intraocular Pressure Measurement System for Monitoring Eye Pressure

Permalink

https://escholarship.org/uc/item/6p66q0jb

Author

Phan, Alex

Publication Date

2018

Peer reviewed|Thesis/dissertation

eScholarship.org Powered by the California Digital Library
University of California

UNIVERSITY OF CALIFORNIA SAN DIEGO

Design and Investigation of an Optical Intraocular Pressure Measurement System for Monitoring Eye Pressure

A dissertation submitted in partial satisfaction of the

requirements for the degree

Doctor of Philosophy

in

Engineering Sciences (Mechanical Engineering)

by

Alex Minh Giang Phan

Committee in charge:

Professor Frank E. Talke, Chair
Professor Shaya Fainman
Professor James Friend
Professor Juan Lasheras
Professor Geert W. Schmid-Schoenbein

2018

Copyright

Alex Minh Giang Phan, 2018

All rights reserved.

The Dissertation of Alex Minh Giang Phan is approved, and it is acceptable in quality and form for publication on microfilm and electronically:

_____

_____

_____

_____

_____
Chair

University of California San Diego

2018

DEDICATION

To my family and friends.

TABLE OF CONTENTS

SIGNATURE iii
DEDICATION iv
TABLE OF CONTENTS v
LIST OF ACRONYMS x
LIST OF FIGURES xi
LIST OF TABLES xvii
ACKNOWLEDGEMENTS xviii
VITA xxii
ABSTRACT OF DISSERTATION xxiv
Chapter 1 Introduction 1
1.1 Glaucoma 1
1.1.1 The Pathophysiology of Glaucoma 1
1.1.2 Current Standard of Care 5
1.2 State of the Art 7
1.2.1 Commercially Available Pressure Sensors 7
1.2.2 Types of Intraocular Pressure Sensors 9
1.2.3 Active Implants 10
1.2.4 Passive Implants 11
1.3 Dissertation Objective 13
1.4 Organization of Dissertation 13
Chapter 2 Design of an Implantable Intraocular Pressure Sensor 16
2.1 Design Parameters and Requirements 16
2.2 Intraocular Pressure Measurement System 17
2.3 Principle of Operation 18
2.3.1 Interferometry 18
2.3.2 Operation Principle of the IOP Sensor 21
2.4 Conditions for Obtaining Quality Fringes 23
2.4.1 Temporal Coherence 24
2.4.2 Spatial Coherence 25
2.5 Diaphragm Consideration 26
2.5.1 Material 26

2.5.2 Shape of Diaphragm 27
2.6 Analytical Model and Simulation 29
2.6.1 Square Diaphragm Deflection 29
2.6.2 Fresnel Reflection and Thin Film Interferometry 30
2.6.3 Sensor Modeling 31
2.7 Summary 34
Chapter 3 Sensor Fabrication and Testing 35
3.1 Fabrication of IOP Sensor 35
3.1.1 Overview of Fabrication Process 35
3.1.2 Design of SU-8 Bonding Pattern 37
3.1.3 Glass Substrate 39
3.1.4 Silicon Nitride Diaphragm 42
3.1.5 Bonding 43
3.1.6 Packaging 44
3.2 Benchtop Testing of IOP Sensor 45
3.2.1 Experimental Setup 45
3.2.2 In vitro Experiment Using Silicone Cornea 47
3.2.3 Ex vivo Experiment using Rabbit Cornea 50
3.2.4 Discussion 51
3.3 Summary 52
Chapter 4 Effects of Temperature, Incident Angle, and Substrate Coating 54
4.1 Introduction 54
4.2 Effects of Temperature 54
4.2.1 Experimental Design 55
4.2.2 Results 57
4.2.3 Discussion 58
4.3 Effects of Incident Angle 59
4.3.1 Experimental Design 59
4.3.2 Results 60
4.3.3 Discussion 62
4.4 Effects of Substrate Coating Thickness 62
4.4.1 Definition of Visibility 62
4.4.2 Optimization of Visibility 63

4.4.3 Experimental Design and Results 64
4.4.4 Discussion 66
4.5 Summary 67
Chapter 5 Optical Handheld Reader 69
5.1 Introduction 69
5.2 Light Source 69
5.2.1 Safety Considerations 69
5.2.2 Light Source Selection 70
5.3 First Generation Handheld Reader 72
5.3.1 Configuration and Assembly 72
5.3.2 Experimental Testing 73
5.3.3 Discussion 76
5.4 DSLR Handheld Reader 76
5.4.1 Configuration and Construction 76
5.4.2 Experimental Testing 79
5.4.3 Discussion 80
5.5 Mobile Device Attachment and Android App 80
5.5.1 Configuration and Construction 81
5.5.2 Smartphone Application on Android Platform 85
5.5.3 Experimental Testing 87
5.5.4 Discussion 90
5.6 Summary 91
Chapter 6 Ex vivo Investigation of an Optical Intraocular Pressure Sensor 92
6.1 Introduction 92
6.1.1 Implantation Sites 92
6.1.2 Cataract and Intraocular Lens 93
6.1.3 Capsular Tension Ring 94
6.2 Intraocular Lens 95
6.2.1 Sensor Fabrication and Integration 96
6.2.2 In vitro calibration 97
6.2.3 Implantation 99
6.2.4 Ex vivo Experiment 99
6.2.5 Discussion 101

6.3 Capsular Tension Ring 102
6.3.1 Sensor Integration and Implantation – Flat Position 103
6.3.2 Ex vivo Experiment - Flat Position 104
6.3.3 Sensor Integration and Implantation - Angled Position 106
6.3.4 Ex vivo Experiment - Angled Position 107
6.3.5 Discussion 107
6.4 Iris Claw 109
6.4.1 Sensor Integration and Implantation 109
6.4.2 Ex vivo Experiment 110
6.4.3 Discussion 111
6.5 Summary 112
Chapter 7 Implantation of an Optical Pressure Sensor in Live Rabbits 114
7.1 Introduction 114
7.1.1 iCare tonometer 114
7.1.2 Rabbits 115
7.2 First Round of Implantation 115
7.2.1 Sensor Preparation 116
7.2.2 Sensor Implantation 117
7.2.3 Sensor Calibration 118
7.2.4 IOP Measurements 119
7.2.5 Twelve Hour Study 123
7.2.6 10-day Study 124
7.2.7 Discussion 125
7.3 Second Round of Implantation 128
7.3.1 Intraocular Lens with Circular Sensor 128
7.3.2 Long term study 130
7.3.3 Transient study 133
7.3.4 Histology Study 134
7.3.5 Discussion 135
7.4 Summary 137
Chapter 8 Image Processing 139
8.1 Image Correlation 139
8.2 Power Spectrum Analysis 141

8.3 Diaphragm Deflection Mapping 143
8.4 Summary 145
Chapter 9 Conclusion and Future Direction 146
9.1 Conclusion 146
9.2 Future Direction 149
References 151

LIST OF ACRONYMS

CMRR	Center for Memory and Recording Research
CTR	Capsular Tension Ring
DSLR	Digital Single Lens Reflex
FWHM	Full Width at Half Maximum
IOL	Intraocular Lens
IOP	Intraocular Pressure
KPro	Keratoprosthesis
PECVD	Plasma-Enhanced Chemical Vapor Deposition

LIST OF FIGURES

Figure 1.1: Aqueous humor drainage pathways of (a) healthy eye and (b-c) glaucomatous eye [35]. 2
Figure 1.2: An image representation of the progressive impact of glaucoma over time [48]. 3
Figure 1.3: Schematic of how elevated eye pressure could affect the optic nerve in glaucoma patients [49]. 4
Figure 1.4: Possible pathways that are affected by elevated intraocular pressure [50]. 4
Figure 1.5: Force-balance schematic representation of Goldmann applanation technique. 6
Figure 1.6: Types of IOP sensors available commercially and in the literature. 7
Figure 1.7: Sensimed Triggerfish contact lens with components labeled (left). Triggerfish contact lens in use by patient (middle). Pressure readout coil inductively acquiring data (right). [78] 8
Figure 1.8: Implandata pressure transducer (left) [80] and implant location of the sensor (right) [81]. 9
Figure 1.9: Implandata pressure transducer wireless readout concept [82]. 9
Figure 1.10: Pressure sensor proposed by Ghaed et al. (left) and corresponding electrical components schematic (right) [95]. 10
Figure 1.11: Pressure sensing concept proposed by Chen et al. using an RLC circuit [98-99]. 12
Figure 2.1: Optical intraocular pressure measurement system with implanted sensor and a portable handheld reader. 18
Figure 2.2: Example of interference fringes in different applications [111-112]. 18
Figure 2.3: The Michelson interferometry utilizes two mirrors to interfere light at the beam splitter and captures the fringes using a detector. 19
Figure 2.4: Configuration of the Fizeau interferometer. The system is comprised of a reference flat surface, a test flat surface, detector, and light source. 20
Figure 2.5: Schematic of sensor components: glass substrate, spacer and flexible diaphragm. 21
Figure 2.6: Schematic of light reflections at the sensor cavity. Incident angle θ_i is 0°. Light paths are drawn at an angle for illustration purposes. 22
Figure 2.7: Schematic of sensor operation. Diaphragm deformation under (a) low pressure and (c) high pressure. Simulated resulting concentric interference patterns (from top view) under monochromatic light for (b) low pressure and (d) high pressure. 23
Figure 2.8: Illustrations of interference patterns generated from monochromatic light sources with different coherent characteristics: (a) high temporal and spatial coherence, (b) poor temporal and high spatial coherence and (c) high temporal and poor spatial coherence [124]. 25
Figure 2.9 Schematic of typical fabrication steps for diaphragm using standard MEMS technique: (a-c) square diaphragm and (d-f) circular diaphragm. Front and back side of the diaphragm: (g-h) square diaphragm and (i-j) circular diaphragm. 28

Figure 2.10: Selectivity of wet etching of silicon substrate: <100> plane is etched at a much faster rate than <111> plane [134]. 29
Figure 2.11: Schematic of light reflections at the sensor interfaces. Incident angle $\Theta_i = 0$. Light paths are drawn at an angle for illustration purposes. 30
Figure 2.12: Deflection profile of a silicon nitride diaphragm (t = 200 nm, a = 250 μm, E = 270 GPa, $\nu = 0.27$, $\sigma = 135$ MPa) under a pressure load of P = 20 mmHg. 33
Figure 2.13: Simulated fringe patterns at various pressures: 10 mmHg, 20 mmHg, 30 mmHg and 40 mmHg (from left to right). 33
Figure 3.1: Schematic of the 2-stage bonding technique: SU-8 was first patterned on the glass substrate. SU-8 bonded the SiN diaphragm to the glass substrate in first bonding stage and medical grade epoxy enclosed the SU-8 layer and sealed off the sensor cavity in the second bonding stage. 36
Figure 3.2: Various designs of SU-8 patterns for cavity wall and cavity channel (top row), and pictures of corresponding fabricated SU-8 patterns on glass (bottom row). 38
Figure 3.3: Fabrication limit of the width of the channel. 38
Figure 3.4: Heating and cooling procedure for the soft bake and the post bake processes. 40
Figure 3.5: Glass substrate after processing: (a) surface profile using Dektak and (b) photograph of a diced glass substrate. 41
Figure 3.6: SU-8 patterns on glass substrate using (a-d) manufacturing recommended procedure and (e-h) modified procedure. 42
Figure 3.7: Photographs of Norcada silicon nitride diaphragm: (a) square and (b) circular [147]. 43
Figure 3.8: Photographs of bonding alignment setup using silicone mold (left) and custom-built clamping device for bonding (right). 43
Figure 3.9: Photographs of the 2-stage bonding process: (a) aligned sensor components (b) after SU-8 bonding (stage 1), (c) epoxy bonding (stage 2), and sensor after bonding. 44
Figure 3.10: (a) Photograph of sensor (b) Schematic of sensor (c) Photograph of sensor under monochromatic light (d) SEM photograph of cross section of the sensor (epoxy filling was used to preserve the cavity of the sensor during cross section dicing). 45
Figure 3.11: (a) Photograph of experimental setup (left) (b) Schematic of experimental setup (right). 46
Figure 3.12: (a) Silicone cornea (b) rabbit cornea (c) sensor mounted in the artificial anterior chamber. 47
Figure 3.13: Images of interference patterns obtained from in-vitro experiment at pressure load of (a) 0 mmHg (b) 20 mmHg (c) 40 mmHg (d) 60 mmHg. 48
Figure 3.14: Maximum deflection of the sensor diaphragm as a function of applied pressure. 49
Figure 3.15: Measured pressure versus applied pressure for in-vitro (silicone cornea) pressure measurements using the optical pressure sensor. 49

Figure 3.16: Measured pressure versus applied pressure for ex-vivo (rabbit cornea) pressure measurements using the optical pressure sensor. 51
Figure 4.1: Schematic (left) and photograph of experimental setup (right). 56
Figure 4.2: Effect of temperature on the maximum diaphragm deflection at a fixed pressure load. 57
Figure 4.3: Calibration curves of the same sensor from 0 mmHg – 40mmHg at 24°C and 37°C. 58
Figure 4.4: Experimental setup for the incident angel experiment using load cell and a goniometer. Incident angles (measure from the horizontal axis) of 90°, 93°, and 96° are shown here. 59
Figure 4.5: Sensor readout at various incident angles: (a) 0° incident angle (b) 3° incident angle (c) 6° incident angle (d) 7° incident angle. 60
Figure 4.6: Intensities of fringe pattern along the diagonal line of the diaphragm at various incident angles: (a) 0° incident angle (b) 3° incident angle (c) 6° incident angle (d) 7° incident angle 61
Figure 4.7: Effect of incident angle on pressure measurements. 61
Figure 4.8: Schematic of interfering light with silicon nitride coating on the bottom surface of the glass substrate. 63
Figure 4.9: Visibility, V, and intensity of reflected light waves from the surface of the glass, I_1, and diaphragm, I_2, as a function of coating thickness. Highest visibility of the interference pattern was achieved for a silicon nitride coating thickness in the range from 50 to 100 nm. 64
Figure 4.10: Images of interference pattern obtained from setup with glass substrate with varying silicon nitride coating thickness. 65
Figure 4.11: Intensities of the fringe patterns obtained from different coating thicknesses. 66
Figure 5.1: Interference patterns generated using different light sources: laser light source (left), halogen light with 1 nm laser line filter (middle), 635 nm LED with 5 nm laser line filter (right). 71
Figure 5.2: Portable handheld reader for optical pressure measurement system. 72
Figure 5.3: Portable handheld reader for optical pressure measurement system. 73
Figure 5.4: Experimental set up to evaluate the handheld reader. 74
Figure 5.5: Fringe pattern of the same sensor at 20 mmHg pressure captured using the bench top lab setup (left) and the handheld reader (right). 75
Figure 5.6: In-vitro pressure measurement using the handheld reader with a CMOS camera and a smartphone camera. 75
Figure 5.7: Schematic of the DSLR handheld reader. 77
Figure 5.8: Adaptor for DSLR optical handheld reader 78
Figure 5.9: Photograph of the DSLR handheld reader. 78
Figure 5.10: Measured pressure versus applied pressure for in vitro pressure measurements using the DSLR handheld reader. 79
Figure 5.11: Images of interference patterns obtained from in-vitro experiment using the DSLR reader at pressure load of (a) 0 mmHg (b) 20 mmHg (c) 40 mmHg (d) 60 mmHg. 80

Figure 5.12: Schematic of custom lens system of the smartphone handheld reader. Interference fringes from the sensor (right) are directed to the phone camera (left) through the lens system. 82
Figure 5.13: Ray trace diagram of the optical system simulated using Zemax. The sensor is placed on the right side of the diagram and the phone is placed on the left side of the diagram. 82
Figure 5.14: Distortion field plot of the optical system simulated using Zemax. The maximum distortion of 2.42% was simulated for a field of 1.4 x 1.4 mm.. 83
Figure 5.15: Schematic (top) and photograph (bottom) of the smartphone handheld reader 84
Figure 5.16: Process flow diagram of the IOP smartphone app 86
Figure 5.17: Screenshots of the main functions of the IOP app: (L) Home screen with options to take new measurement or load the measurement log, (C) Image processing to determine the pressure value, and (R) IOP measurement log. 87
Figure 5.18: Experimental setup to evaluate the smartphone reader. The IOP sensor is mounted in a pressure control artificial anterior chamber. The smartphone reader is position directly above the chamber to capture the response of the sensor. 88
Figure 5.19: Typical image of the sensor captured using the smartphone reader in a static setup (top). Visibility plot of the corresponding interference pattern (bottom). 89
Figure 5.20: Measured pressure versus applied pressure for in vitro pressure measurements using the smartphone handheld reader. 90
Figure 6.1: A cross sectional image of the anterior segment of a human eye captured using optical coherence tomography [153]. 93
Figure 6.2: Illustration of a cataract surgery [156]: (a) phacoemulsification process of removing the native lens, (b) inserting the artificial lens using an IOL injector and (c) position the IOL in the capsular bag. 94
Figure 6.3: Schematic of how a CTR provides structure support to a capsular bag that has weak or defective region of zonules. 95
Figure 6.4: (a) Schematic of optical IOP sensor and (b) cross sectional view and dimensions of the sensor. 96
Figure 6.5: Photographs of (a) fabricated IOP sensor, (b) sensor integrated to Acrysof Multipiece IOL and (c) sensor integrated to Artisan Phakic IOL. 97
Figure 6.6: Schematic and photograph of experimental setup using artificial anterior chamber. 98
Figure 6.7: Sensor diaphragm deflection as a function of pressure. 99
Figure 6.8: Photographs of IOP sensors integrated to (a) Acrysof Multipiece IOL and (b) Artisan Phakic IOL post implantation. 99
Figure 6.9: Ex-vivo experimental setup. 20-gauge needle was used to connect the pressure regulator to the posterior chamber of the rabbit eye. 100
Figure 6.10: Measured versus applied pressure for ex-vivo measurements. Measurement taken using sensor integrated to an Acrysof Multipiece IOL. 100

Figure 6.11: Measured versus applied pressure for ex-vivo measurements. Measurement taken using sensor integrated to an Artisan Phakic IOL. 101
Figure 6.12: Schematic of the capsular tension ring implantation approach. The sensor is integrated to an CTR and placed in the sulcus space. Iridectomy procedure provides an opening for direct optical access to the sensor. 103
Figure 6.13: Photograph of (a) capsular tension ring end loop, (b) CTR end loop bonded to the back side of the IOP sensor, (c) IOP sensor integrated to a capsular tension ring. 103
Figure 6.14: Photograph of the sensor-CTR unit post implantation. Outline of the CTR is shown in green. 104
Figure 6.15: Differences in sensor orientation on the capsular tension ring (CTR). 105
Figure 6.16: Photograph of the IOP sensor bonded to the capsular tension ring at a 45° angle. Side view of the unit (left) and isometric view of the unit (right).. 106
Figure 6.17: Photograph of sensor after implantation (left) and appearance of interference fringes when monochromatic light was directed to the sensor (right). 106
Figure 6.18: Ex vivo IOP measurements using an IOP sensor mounted on a capsular tension ring at a 45° angle..... 107
Figure 6.19: Light ray trace diagram as light travels through the cornea and arrives at the IOP sensor. The sensor is placed at a horizontal position (left). The sensor is placed at a 45º angle (right)..... 108
Figure 6.20: (a) Iris claw cut out from Ophtec Artisan lens, (b) IOP sensor integrated to the iris claw and (c) IOP sensor implanted on the surface of the iris..... 110
Figure 6.21: Ex vivo experiment using the iris claw. 110
Figure 6.22: Render image of the IOP sensor and the vertical iris claw (left) and proposed implant location of the IOP sensor and iris claw in the eye (right)..... 111
Figure 7.1: Photographs of the IOP sensors integrated to modified intraocular lenses.. 117
Figure 7.2: Photographs of (a) the rabbit eye before implantation (b) the phacoemulsification process of removing the native lens, (c) the IOP-sensor unit being inserted into the capsular bag. 118
Figure 7.3: Photographs of the implanted sensor in rabbit #1 (left) and rabbit #2 (right). 118
Figure 7.4: Comparison of sensor calibration before and after implantation. 119
Figure 7.5: Photographs of the IOP sensors in rabbit eyes 3-week post implantation. .. 120
Figure 7.6: Image of fringe pattern was captured, analyzed and compared with the calibration curve to determine IOP. 121
Figure 7.7: Photograph of DSLR optical reader. 122
Figure 7.8: Photograph of implanted IOP sensor: (a) ambient light, (b) monochromatic light..... 122
Figure 7.9: IOP measurement using iCare rebound tonometer..... 123
Figure 7.10: 12-hour in-vivo IOP measurements using interferometric IOP sensor and iCare tonometer. 124
Figure 7.11: Intraocular pressure profile of the rabbit over a 10-day period obtained using the implanted IOP sensor. 125
Figure 7.12: Comparison of pressure readings from IOP sensor and iCare tonometer after correction for iCare readings. 127

Figure 7.13: (a) Circular IOP sensor, (b) soft IOL with a circular cutout and (c) IOP sensor integrated to IOL. 129
Figure 7.14: (a) Alcon Monarch II delivery system and (b) size comparison of Monarch cartridges: A – 3.2 mm, B – 3.0 mm, C – 2.8 mm and D – 2.2 mm [166].129
Figure 7.15: (a) IOL during injection, (b) IOL immediately after injection and (c) IOL 5 minutes after injection. 130
Figure 7.16: IOP of the left eye and right eye (implanted sensor) were monitor daily using the TonoVet for a duration of 23 days. 131
Figure 7.17: Average maximum deflection of the sensor increased linearly over time due to drift. 132
Figure 7.18: Comparison of the long-term pressure measurements using the IOP sensor and the TonoVet. 132
Figure 7.19: Induced artificial high pressure using intravitreal saline injection. Eye pressure monitored using the IOP measurement system and the TonoVet tonometer for a one-hour period. 133
Figure 7.20: Images of the H&E staining of the rabbit eye post-implantation: (a) whole globe and (b-c) ciliary apparatus including the ciliary processes and the iris. 135
Figure 8.1: Correlation of interference patterns with the database for five different pressure loads from 10 to 50 mmHg. 140
Figure 8.2: Interference patterns at different pressure loads and their corresponding power spectrum plots. 141
Figure 8.3: Average pixel intensity of the power spectrum of the fringe patterns as a function of applied pressure from 0-60 mmHg (1 mmHg step size). 143
Figure 8.4: Image processing approach using diaphragm deflection: (a) isolate a cross section of the fringe pattern, (b) determine the locations of peaks and troughs, (c) map the deflection of the diaphragm along the cross section and (d) 3D reconstruction of the deflection profile of the diaphragm. 145

LIST OF TABLES

Table 2.1: Example of temporal coherence length of various light sources. 24
Table 2.2: Burst Pressure (PSI) for various Norcada silicon nitride diaphragms [128]. .. 27
Table 2.3: Modeling parameters for the monochromatic light source and the silicon nitride diaphragm 32
Table 5.1: Approaches to generate monochromatic light. 70

ACKNOWLEDGEMENTS

I want to begin this acknowledgement by saying words can't begin to describe how grateful I am to have such supportive faculty, lab members, and engineering community throughout my academic career. I have learned so much from everyone and am appreciative of their time, patience, and guidance during my Ph.D. journey. This dissertation would not have been possible without this amazing and strong community of people.

First, I would like to express my sincere gratitude to Professor Talke, my academic advisor. With Professor Talke's mentorship, I learned so much about engineering and the importance of impactful research. He challenged me with a project that tested my ability to be resourceful and think outside the box. After decades of teaching and research, Professor Talke's enthusiasm and love for science continues to inspire his students; something I really admire and can only hope to aspire towards as I continue my academic career. After years of learning under Professor Talke, I grew as an engineer and researcher, and will never forget the lessons I learned during my time in his lab.

Second, I would like to thank Phuong, my co-researcher and great friend. She came to our lab in 2013 as an undergraduate student and has grown alongside me as we both learned to navigate the unknown terrains in research. She has grown from a quiet undergraduate student to a confident and strong engineer, researcher, and leader. Without her, the lab would still be a junkyard of old experiments and projects with me in the corner attempting to do research. It is worth noting the contributions she's made to the project, which includes but is not limited to: research, cleaning and organizing the lab, recruiting and organizing an amazing team, always thinking of the next step for the project, writing

grants, and of course, always keeping me on track. Thank you so much for your help on this project! You have helped me grow so much as well, thank you for the feedback and opportunities.

I wish to express my appreciation for Dr. Camp, Dr. Weinreb and Dr. Melles, whose medical insight helped shape the feasibility of this project. I greatly appreciate the time you take out of your schedules to meet with us and provide us with the feedback we need to make progress on the project. Special thanks to Dr. Camp for performing all the surgeries and ex vivo implantations throughout this project.

I would like to thank Ben Suen, a lab member and friend whose resourcefulness and bottomless sea of knowledge never fails to astonish me. He has helped find so many critical components to my experiments that I would have never been able to find. In addition to Ben, I would like to mention the great help from other former and current lab members throughout this project: Dr. Young Seo, Dr. Youyi Fu, Karcher Morris, Scott Garner, Tan Trinh, Oren Gotlib, and Christoph Schade. Without all these great personalities, the lab would not be as unique and interesting.

Also, of great support to this project were Alexander Kief, Millien Dhorne, Julian Trumpp, Jörg Schröter, Kerrianne Stewart, Buu Truong, and Ella Stimson. Without this team of great engineers, the project would not have such depth and success. Each of these members contributed to an aspect of this project and worked closely with me to overcome engineering and research challenges.

Iris Villanueva and Ray Descoteaux were very big contributors to my success during the past several years due to their dedication and supportive roles. Thank you to Iris for all of her support and taking care of our lab finances and grants. I appreciate your

commitment to helping the CMRR family and will miss your presence after your retirement. Thank you to Ray as he has taken the time to machine and develop many of the experimental apparatus used in my project. His patience and persistence were a cornerstone to making my experimental setups possible. Thank you so much for your help, Ray. Special thanks to the entire CMRR staff, you all have been wonderful to work with and I am really grateful for all of your contribution to our building.

My life changed trajectory as a result of involvement with the ECE department and I would like to thank Professor Nguyen for opening teaching opportunities for me. I learned a great deal being an instructor and will continue to learn and build my teaching career. On this note, I would like to also thank my LabVIEW teaching team: Eric Ho, Matthew Kohanfars, Buu Truong, Adrienne Chang, and Angela Xu. Thank you all for your contribution to this endeavor and dedication to help students become well rounded engineers.

Finally, I would like to also thank my parents whose unconditional support endured my ups and downs during this journey. They had waited so long for me to finish my degree and see me achieve my dreams. They have labored all of their lives and sacrificed so much to ensure my future and success. Thank you so much for your love, patience, perseverance, encouragement, support, and sacrifice.

Chapter 2, in part is a reprint of the material as it appears in " Design of an Optical Pressure Measurement System for Intraocular Pressure Monitoring," Phan, Alex, Phuong Truong, Julian Trumpp, and Frank E. Talke, *IEEE Sensors Journal*, vol. 18, no. 1, 2018, pp. 61–68. The dissertation author was the primary investigator and author of this paper.

Chapter 3, in part is a reprint of the material as it appears in " Design of an Optical Pressure Measurement System for Intraocular Pressure Monitoring," Phan, Alex, Phuong Truong, Julian Trumpp, and Frank E. Talke, *IEEE Sensors Journal*, vol. 18, no. 1, 2018, pp. 61–68. The dissertation author was the primary investigator and author of this paper.

Chapter 4, in part is a reprint of the material as it appears in "Optimization of an interferometric pressure sensor for intraocular pressure measurements," Phan, Alex, Phuong Truong, Julian Trumpp, and Frank E. Talke, *2018 ASME Information Storage and Processing Systems,* Aug. 29 – 30, 2018, San Francisco, CA. The dissertation author was the primary investigator and author of this paper.

Chapter 6, in part is a reprint of the material as it appears in "Optical intraocular pressure measurement system for glaucoma management," Phan, Alex, Phuong Truong, Alexander Kief, Milien Dhorne, Andrew Camp, Robert N. Weinreb, and Frank E. Talke, *2017 IEEE Healthcare Innovations and Point of Care Technologies (HI-POCT)*, Bethesda, MD, 2017, pp. 188-191. The dissertation author was the primary investigator and author of this paper.

Chapter 7, in part is a reprint of the material as it appears in "A Wireless Handheld Pressure Measurement System for in vivo Monitoring of Intraocular Pressure in Rabbits," Phan, Alex, Phuong Truong, Andrew Camp, Kerrianne Stewart, Benjamin Suen, Robert N. Weinreb, and Frank E. Talke, *In Preparation for Publication*. The dissertation author was the primary investigator and author of this paper.

VITA

06/2011	Bachelor of Science in Bioengineering University of California, San Diego, La Jolla, CA, USA
2009 – 2012	Associate Scientist, Cancer and Structural Biology Dept. Pfizer Global Research & Development, La Jolla, CA, USA
2013	Engineering Aid at Center for Memory and Recording Research University of California, San Diego, La Jolla, CA, USA
2014 – 2016	Teaching and Research Assistant for UCSD Mechanical Engineering Department University of California, San Diego, La Jolla, CA, USA
06/2014	Master of Science in Engineering Sciences (Mechanical Engineering) University of California, San Diego, La Jolla, CA, USA
2017 – Present	Research Assistant at Center for Memory and Recording Research and Instructor for UCSD Electrical and Computer Engineering Department University of California, San Diego, La Jolla, CA, USA
09/2018	Doctor of Philosophy in Engineering Sciences (Mechanical Engineering) University of California, San Diego, La Jolla, CA, USA

PUBLICATIONS

Journal Papers

Phan, Alex, Phuong Truong, Andrew Camp, Kerrianne Stewart, Benjamin Suen, Robert N. Weinreb, and Frank E. Talke, "A Wireless Handheld Pressure Measurement System for in vivo Monitoring of Intraocular Pressure in Rabbits," *In Preparation for Publication.*

Phan, Alex, Phuong Truong, Julian Trumpp, and Frank Talke, "Design of an Optical Pressure Measurement System for Intraocular Pressure Monitoring," *IEEE Sensors Journal*, vol. 18, no. 1, pp. 61-68, Jan. 1, 2018.

Zhang, Chuanwei, Alex Phan, Young Seo, Andrey Ovcharenko, Min Yang, and Frank Talke, "Effect of a Void on the Heat Transfer in the Head Disk Interface," *Microsystem Technologies*, Mar. 2015.

Conference Papers

Phan, Alex, Phuong Truong, Frank Talke, "Optimization of an interferometric pressure sensor for intraocular pressure measurements," *2018 ASME Information Storage and Processing Systems,* Aug. 29 – 30, 2018, San Francisco, CA.

Phan, Alex, Phuong Truong, Andrew Camp, Robert Weinreb, and Frank Talke, "In vivo Investigation of an Interferometric Pressure Measurement System for Glaucoma Management," *2018 ARVO Annual Meeting,* Apr. 29 – May 03, 2018, Honolulu, HI.

Phan, Alex, Phuong Truong, Alexander Kief, and Frank Talke, "Development of a function-augmented Boston Keratoprosthesis for intraocular pressure measurement," *7th International Conference on Mechanics of Biomaterials and Tissues,* Dec. 10-14, 2017, Waikoloa, HI.

Phan, Alex, Phuong Truong, Alexander Kief, Millien Dhorne, Andrew Camp, Robert Weinreb, and Frank Talke, "Optical intraocular pressure measurement system for glaucoma management," *2017 IEEE Healthcare Innovations and Point of Care Technologies (HI-POCT)*, Bethesda, MD, 2017, pp. 188-191.

Zhang, Chuanwei, Young Seo, Alex Phan, and Frank Talke, "Effect of a Disk Asperity and a Void on the Heat Transfer in the Head Disk Interface," *2014 ASME Information Storage and Processing Systems,* June 23 – 24, 2014, Santa Clara, CA.

PATENTS

Phan, Alex, Phuong Truong, Robert Weinreb, Juan Lasheras, and Frank Talke, "Optical Intraocular Pressure Sensor and Sensing Method," The Regents of the University of California, assignee. Patent Application WO2016/064867A2.

ABSTRACT OF DISSERTATION

Design and Investigation of an Optical Intraocular Pressure Measurement System for Monitoring Eye Pressure

by

Alex Minh Giang Phan

Doctor of Philosophy in Engineering Sciences (Mechanical Engineering)

University of California, San Diego, 2018

Professor Frank E. Talke, Chair

Glaucoma is a neurodegenerative disease that affects 65 million people worldwide, causing progressive optic nerve damage over time and irreversible blindness. Elevated intraocular pressure (IOP) in the eye has been considered one of the leading modifiable risk factors of the disease. Standard care relies on indirect eye pressure measurements in a physician's office as one metric to determine therapeutic treatments. Such infrequent single-point measurements are inadequate to fully represent and characterize the patterns associated with disease. In this dissertation we investigate and develop a novel optical-

based pressure sensing system capable of measuring IOP on a frequent or semi-continuous basis.

First, the IOP sensor design requirements were established with the aim of measuring pressure using a passive approach with high sensitivity and repeatability. By using the principle of interferometry and diaphragm deflection, the changes in intraocular pressure were determined through interferometric fringes and maximum diaphragm deflection. Next, studies were conducted to investigate the effects of temperature, incident angle, and substrate coating in order to characterize the behavior of the sensor. In addition, a handheld reader was developed to wirelessly obtain optical information from the sensor. Three generations of handheld readers were developed to enable measurements from live and awake rabbits once the sensor was implanted in vivo. The IOP sensor was evaluated ex vivo using rabbits in order to determine the optimal implant method and anchoring approach. Cataract surgery was performed ex vivo in rabbit eyes to replace the native lens with a modified intraocular lens (IOL) carrying the IOP sensor. Finally, the sensor was further valuated through in vivo studies using New Zealand white rabbits. Cataract surgery was performed on the rabbits to implant the sensor. The study showed that IOP measurements were obtainable in vivo. The presence of the sensor had no observable impact on the rabbits' inflammatory response, suggesting that the system is biocompatible.

Throughout the study, various image processing algorithms were developed in MATLAB to analyze fringe images by employing mathematical models and built-in image analysis functions.

Chapter 1

Introduction

1.1 Glaucoma

Glaucoma to date is one of most common causes of permanent blindness worldwide. The disease affects various demographics, namely individuals of African or Hispanic descent, individuals ages 40 to 80 years old, or individuals who are genetically predisposed to developing the disease [1-10]. The growing population of those affected by glaucoma expected to reach 80 million by 2030 as the population continues to age [11-12]. Compared to other eye diseases such as age-related muscular degeneration, diabetic retinopathy, cataract, and refractive error, glaucoma is the leading cause of irreversible blindness worldwide [13-17]. Elevated intraocular pressure (IOP) continues to be the primary risk factor for glaucoma due to its association with optic nerve damage. For approximately 60 million people worldwide suffering from this disease, careful monitoring and lowering of eye pressure are essential to preventing optic nerve deterioration and further loss of vision [18-22].

1.1.1 The Pathophysiology of Glaucoma

Glaucoma is defined as a neurodegenerative disorder that affects the optic nerve [23-25]. The slow, progressive, and incurable disease is characterized by the deterioration and death of retinal ganglion cells (RGC) over time [26-27]. In normal human eye, ocular

fluid known as aqueous humor is produced at the ciliary body and is removed through drainage canals known as the trabecular meshwork as shown in Figure 1.1a [28-29]. When one or more of these passages are constricted or unable to drain, the buildup of aqueous humor in the anterior chamber can lead to an increase in pressure in the eye. Over time, retinal ganglion cells begin to deteriorate leading to permanent visual field loss [30-32]. Depending on the cause of drainage failure, glaucoma can be classified into various types: open-angle glaucoma (Figure 1.1b), closed-angle glaucoma (Figure 1.1c), normal tension glaucoma, congenital glaucoma, secondary glaucoma, and many others [33-34].

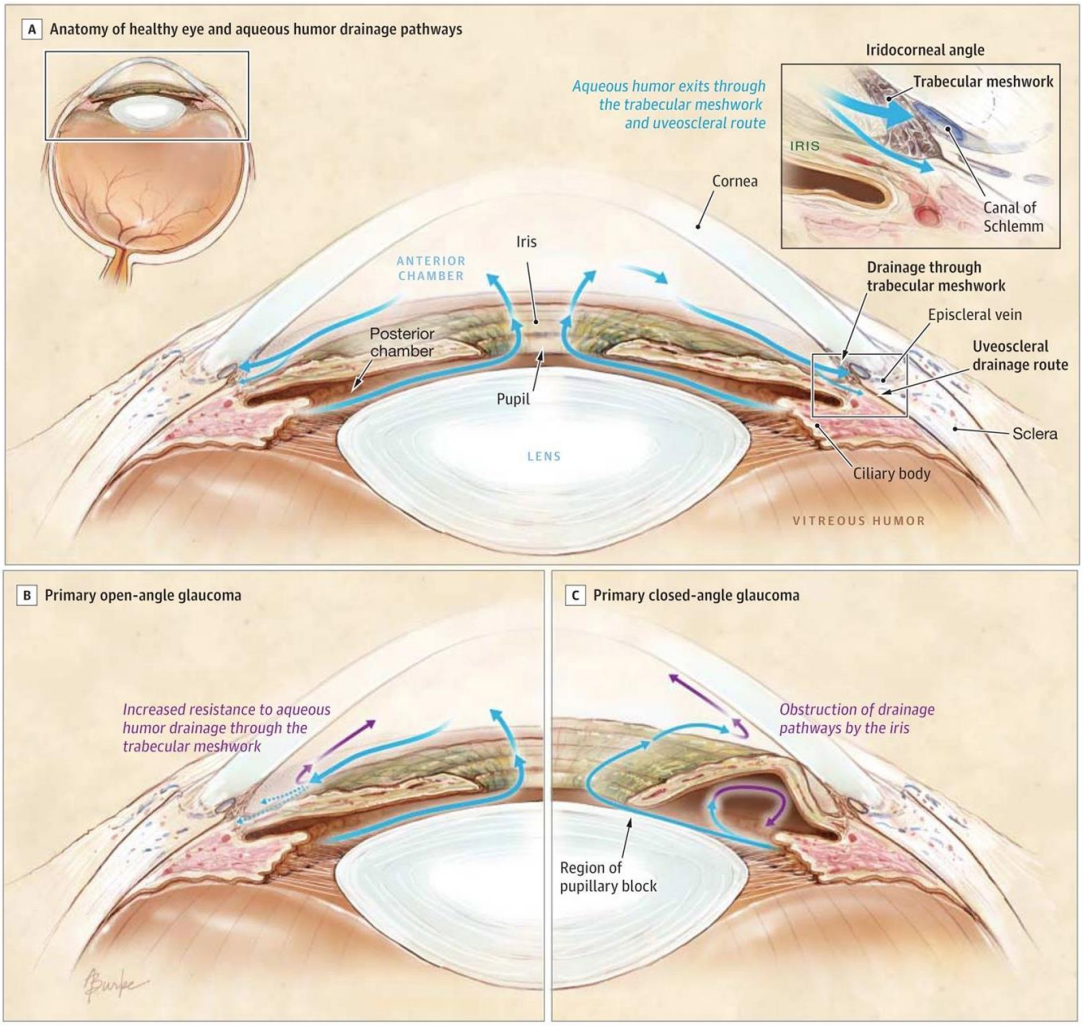

Figure 1.1: Aqueous humor drainage pathways of (a) healthy eye and (b-c) glaucomatous eye [35].

The disease is progressive and gradual over the course of years, remaining undetected by many patients until later stages. As the disease progresses, the patient experiences visual field loss as shown in Figure 1.2. Currently, there is no known direct cause for glaucoma. Research shows multiple potential factors contributing to the disease, including cranial pressure, genetics, ocular blood circulation, biomechanics, disease and many other contributors [36-42]. Elevated pressure has been identified to be the number one modifiable risk factor for the disease with many treatment plans centered around reducing and monitoring eye pressure [43-45]. While it is still unknown whether or not elevated eye pressure is directly connected to glaucoma, research has shown elevated eye pressure could cause mechanical damage, growth factor reduction, increase in glutamate, and interference in other signaling pathways that lead to retinal ganglion cells exhibiting apoptosis (Figure 1.4) [46-47].



Figure 1.2: An image representation of the progressive impact of glaucoma over time [48].

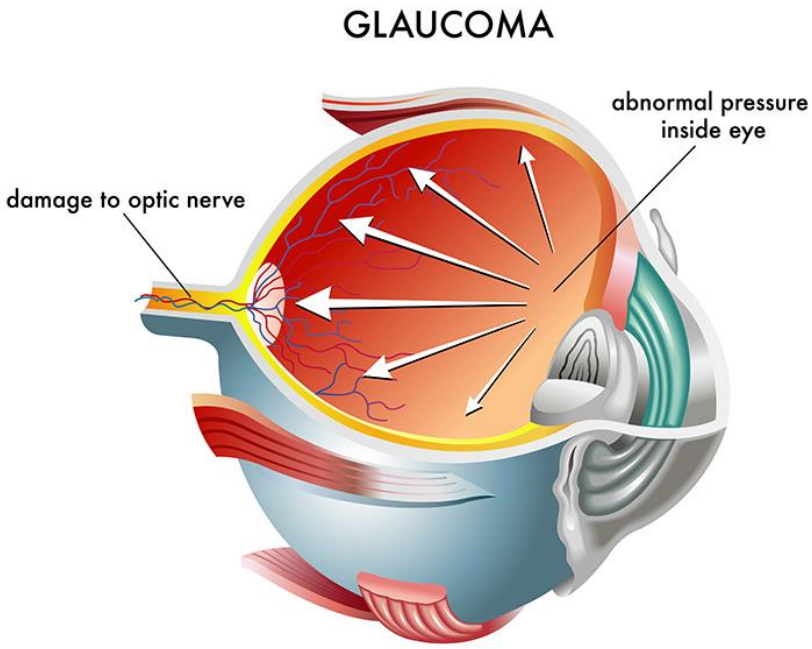

Figure 1.3: Schematic of how elevated eye pressure could affect the optic nerve in glaucoma patients [49].

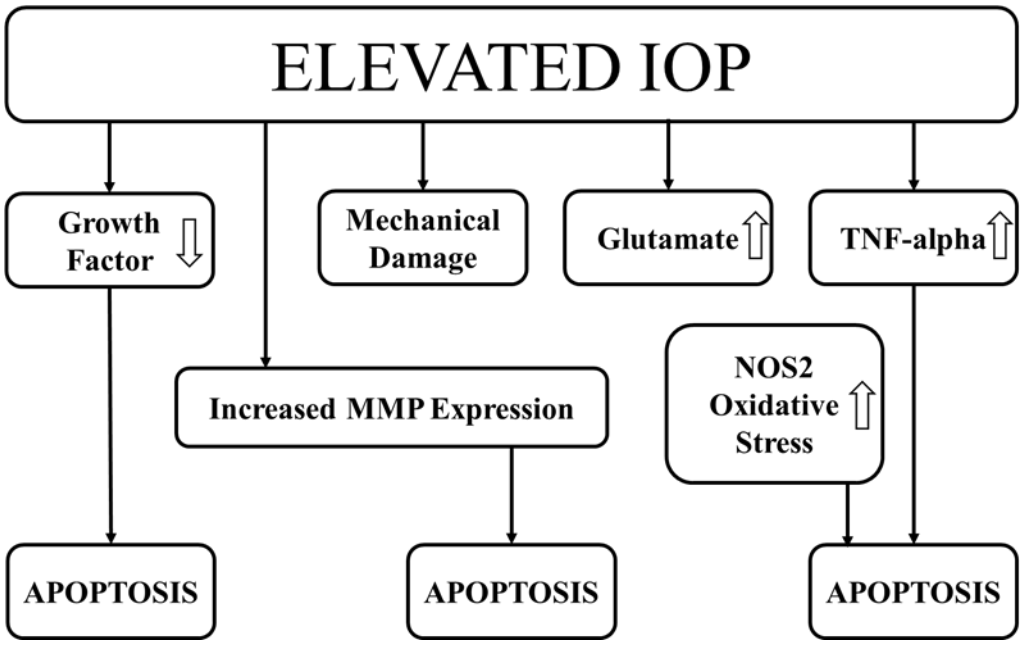

Figure 1.4: Possible pathways that are affected by elevated intraocular pressure [50].

As a result of the unknown direct impacts that lead to glaucoma, elevated eye pressure has been a topic of scientific evaluation and research in the past few decades [51-52].

1.1.2 Current Standard of Care

Currently, standard care for glaucoma consists of clinical examinations comprised of indirect IOP measurements, visual field tests, and optic nerve imaging. Clinical IOP measurements presently utilize indirect pressure measurement techniques to determine pressure. For example, the Goldmann tonometer, the current gold standard for measuring intraocular pressure, is an applanation technique that provides an indirect pressure measurement based on the amount of force required to flatten the corneal surface [53-54]. This measurement method is susceptible to error due to the variation of corneal thickness, shape, and stiffness that may vary over time as a patient ages or differ from patient to patient [55-57]. As a result, the recorded accuracy is limited to ±2 mmHg and can vary by as much as 2 – 3 mmHg with consecutive measurements obtained minutes apart [58]. Similarly, other standard indirect measurement techniques available such as rebound tonometry, indentation tonometry, dynamic contour tonometry, and pneumatic applanation tonometry are all susceptible to the same errors as Goldmann applanation [59].

In addition, studies recorded in the literature have also demonstrated the importance of frequent pressure measurements to determine optimal therapeutic treatments. It is well known that intraocular pressure fluctuates throughout the day, analogous to blood pressure, and can increase or decrease depending on lifestyle, activities, diet, time of day,

and genetics [60]. In 24-hour monitoring studies, the literature has reported cases of rises in intraocular pressure at night that can lead to worsening symptoms of glaucoma [61-63]. To manage the condition, glaucoma treatments focus on reducing elevated eye pressure, the only modifiable risk factor associated with disease [64]. Presently, eye pressure is obtained only a few times a year despite its importance in therapy [65]. Clinical measurements can only provide isolated single-point values and are unable to capture the full profile of a patient's intraocular pressure. The inability to frequently measure pressure limits the physician's capability to create personalized treatment plants for patients [66].

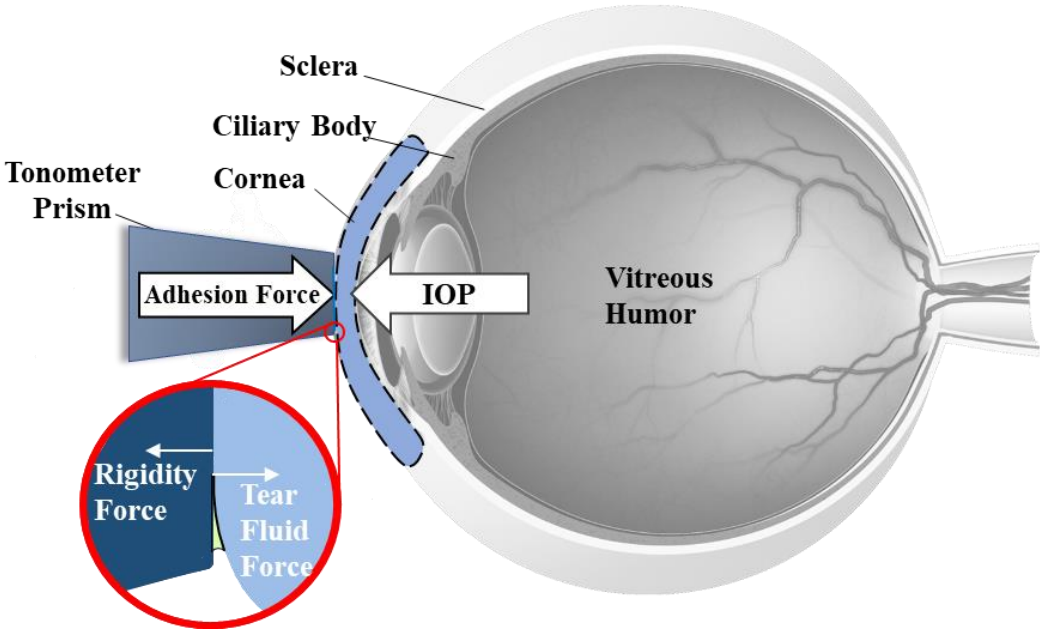

Figure 1.5: Force-balance schematic representation of Goldmann applanation technique.

Thus, in order to improve glaucoma care, there is a pressing need for frequent, direct, and reliable IOP measurements to understand the relationship between elevated eye pressure and optic nerve damage [67].

1.2 State of the Art

In recent years, invasive and non-invasive pressure sensing devices have been developed to enable pressure monitoring frequently, accurately, and reliably [68]. While sensors in the literature vary in approach and implantation method, many can be categorized to fall within the hierarchy of passive or active approaches shown in Figure 1.6.

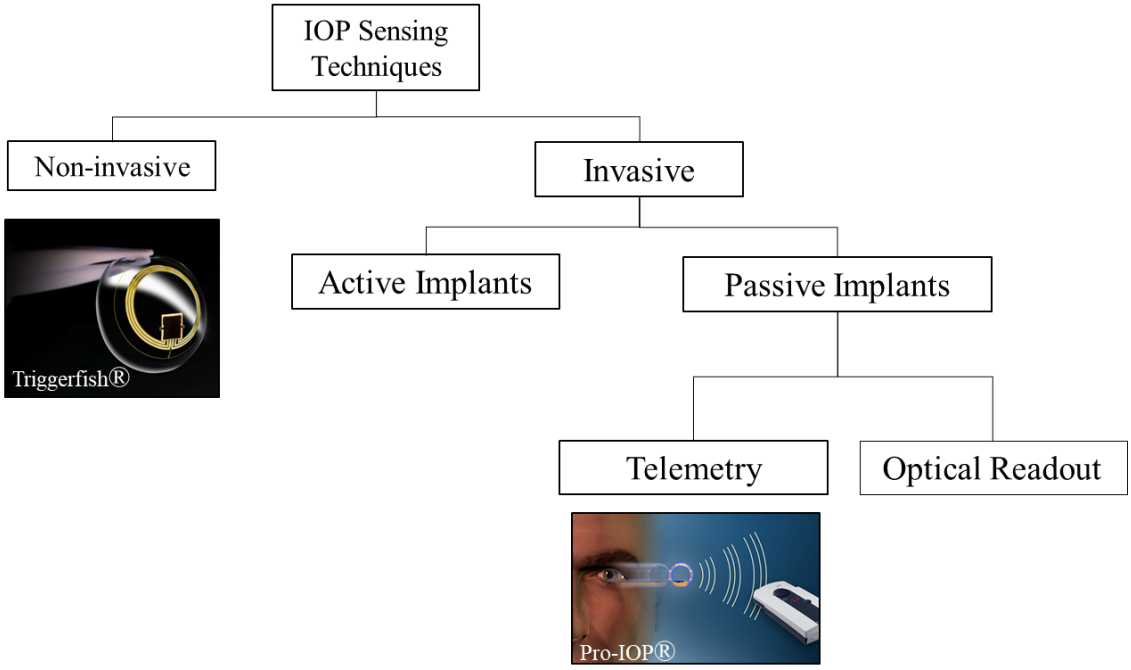

Figure 1.6: Types of IOP sensors available commercially and in the literature.

1.2.1 Commercially Available Pressure Sensors

To date, there are two commercially available pressure sensors: Sensimed's Triggerfish IOP contact lens sensor and Implandata's pressure transducer. Both sensors utilize passive approaches and an inductive coupling circuit to acquire pressure data [69-70].

As shown in Figure 1.7, the Triggerfish contact lens utilizes an embedded strain gauge and circular antenna coil to telemetrically send pressure data. The strain gauges measure the change in corneal curvature and indirectly relate the change to pressure values. While non-invasive, the Triggerfish contact lens has a limited usage of 24 hours as a result of complications that may arise from long-term use. In addition, as a non-invasive approach, the Triggerfish contact lens is prone to errors experienced by the tonometry methods due to varying corneal biomechanics [71-76].

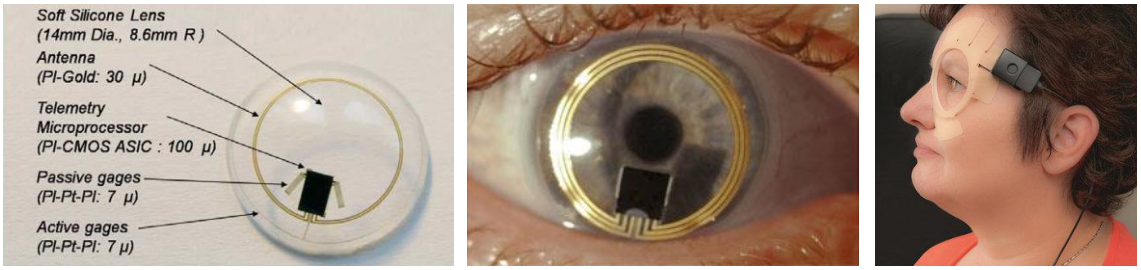

Figure 1.7: Sensimed Triggerfish contact lens with components labeled (left). Triggerfish contact lens in use by patient (middle). Pressure readout coil inductively acquiring data (right). [78]

The pressure transducer by Implandata is an invasive passive pressure sensor that utilizes an RLC integrated circuit to determine pressure changes based on changes in capacitance. As shown in Figure 1.8, the device also integrates an inductive coil antenna in order to telemetrically transmit or acquire resonant frequency information. Frequency data acquired can be correlated with pressure during post-processing. The device is designed to be implanted in the sulcus space behind the iris. In order to obtain a feasible readout distance, the device has a very large form factor due to a large antenna size, limiting its implant location, size, and reader size and placement [79].

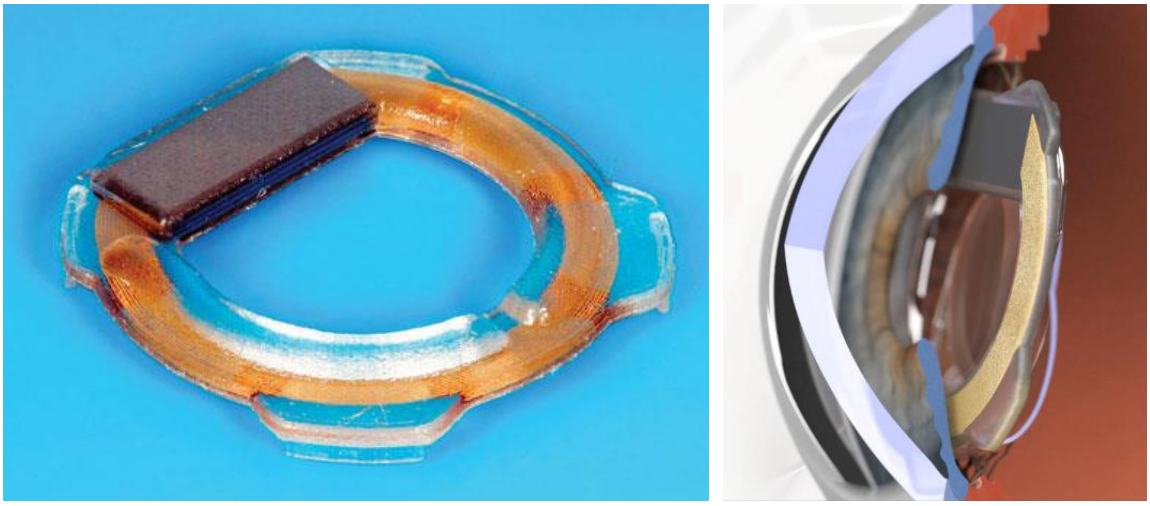

Figure 1.8: Implandata pressure transducer (left) [80] and implant location of the sensor (right) [81].



Figure 1.9: Implandata pressure transducer wireless readout concept [82].

1.2.2 Types of Intraocular Pressure Sensors

Two types of sensing approaches are described in the literature: passive sensing and active sensing. In active sensing approaches, the device requires a power or battery source in order to operate [83-84]. Many piezo resistive, capacitive, and resonance methods

fall under the umbrella of active sensing approaches [85-87]. Passive sensing approaches are devices that do not require a power source in order to operate [88-90]. Many passive sensors operate using optical or inductive coupling, thus requiring no battery to function [90-94].

1.2.3 Active Implants

In the past two decades, a number of active approaches have been developed, many primarily based on capacitive, piezo resistive, and resonance approaches in order to measure pressure. Active sensors commonly include microprocessors, transmitters, and transducers in order to operate or output signals. The sensor proposed by Ghaed et al., for example, correlates changes in IOP with capacitance and transmits the information wirelessly using a transceiver unit (Figure 1.10). The device employs solar cells to recharge the power source, requiring approximately 2 hours of sunlight daily in order to operate [95].

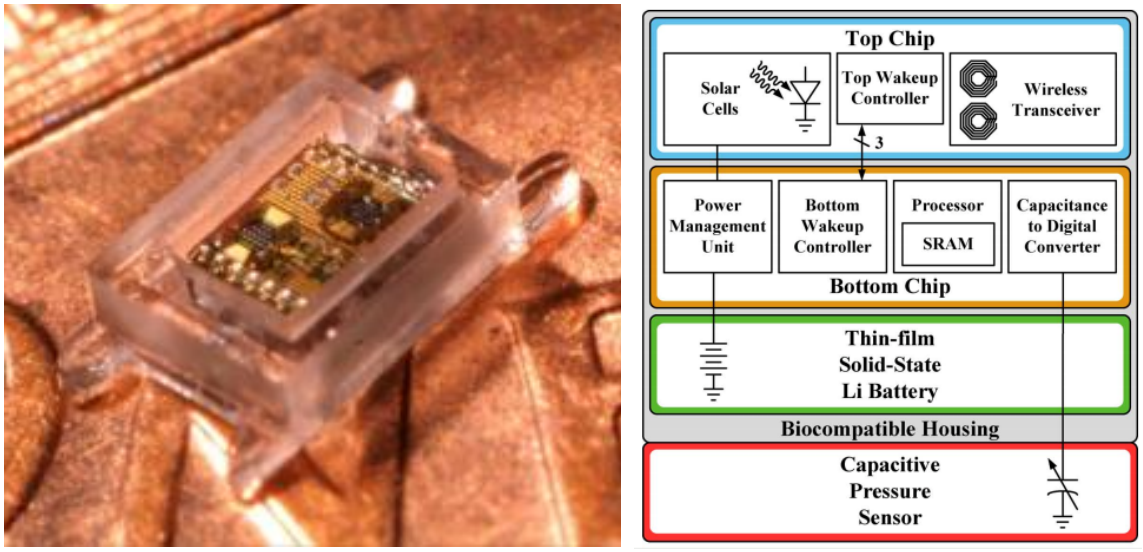

Figure 1.10: Pressure sensor proposed by Ghaed et al. (left) and corresponding electrical components schematic (right) [95].

Similarly, Ritzq et al. have proposed an active approach that utilizes a battery powered piezoresistive pressure transponder to measure pressure [96]. As a result of their complex electrical circuitry, components, and power source, many active implants face limitations on form factor. In comparison to passive sensors, active sensors are typically larger, bulkier, and more challenging to implant. As a result, these types of sensors are not desirable in implantable devices due to the large form factor, limited readout distance, and use of battery. Recently, new approaches have emerged using passive sensing, which require no internal power supply to operate.

1.2.4 Passive Implants

Unlike active sensors, passive pressure sensors do not generally use complex components or internal circuitry. Passive devices commonly rely on physical or mechanical principles to sense pressure and transmit information by optical means or inductive coupling. Araci et al., for example, proposed measuring pressure using changes in a gas-liquid interface [97]. As pressure increases, the force balance between the gas interface and liquid interface changes in position and is tracked. By detecting the position of the interface with respect to channel markers, they acquired measurements by relating marker location to pressure. Chen et al. [98-99] proposed various capacitive sensing designs that employ RLC circuits to passively measure pressure (Figure 1.11). The design utilizes a flexible coil or spiral tube that changes in capacitance when pressure is applied. An inductive circuit is used to measure the change in resonant frequency and determine pressure [100].

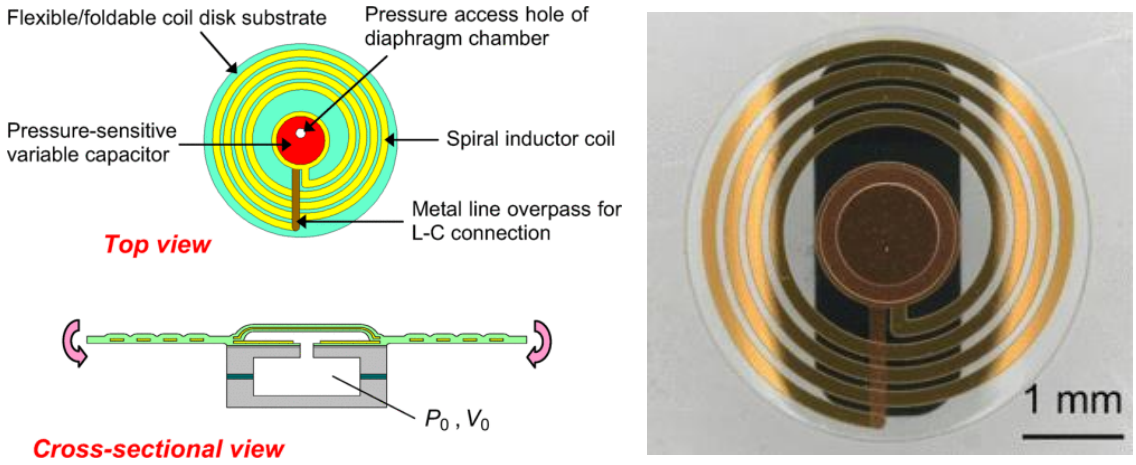

Figure 1.11: Pressure sensing concept proposed by Chen et al. using an RLC circuit [98-99].

Ghannad-Rezaie et al. utilized changes in the intensity ratios of quantum dot layers in a membrane to measure pressure with a 2 mmHg error [101-102]. While novel, their approach has limited accuracy in comparison to previously proposed sensors in the literature [101-102].

While limited in readout range, passive sensors provide a promising method to measuring intraocular pressure wirelessly, frequently, and do not require a power source. Their simple design characteristics enable potential to reduce their form factor over time while maintaining sensing capabilities.

More recently, Lee et al. proposes a method to measure pressure based on the spectral reflectance of a nanodot array [103-104]. While their method of measurement can achieve high accuracy, utilizes very specialized spectrometers to acquire optical readout. This aspect can be challenging to achieve practical application for patient point of care and clinical use.

Generally, passive sensors provide a promising method to measuring intraocular pressure wirelessly, frequently, and do not require a power source. Their simple design characteristics enable potential to reduce their form factor over time while maintaining sensing capabilities.

1.3 Dissertation Objective

The objective of this dissertation is to demonstrate the ability to obtain direct and frequent intraocular pressure measurements using a passive optical approach based on the principles of interferometry and diaphragm deflection. Due to its versatility as a measurement technique, interferometry is used in both scientific and industrial applications ranging from biomedical diagnostics [105] to disk drive technology [106] for determining small changes in distance. Previously, Hastings et al. [107] have patented the potential use of interferometry to measure intraocular pressure, showing its promising applications in biomedical devices. Totsu et al. [108], employed the use of Febry-Perot interferometry to measure blood pressure using fiber-optics. However, no studies on the design and performance of an implantable interferometric intraocular pressure sensing device or system have been published in the literature.

1.4 Organization of Dissertation

Chapter 1 provides an overview and motivation of the dissertation. Glaucoma and the pathology of the disease are discussed. The history of the state of the art is also discussed providing literature on existing active and passive implants.

Chapter 2 is a systems level overview of the optical intraocular pressure sensing approach. The design parameters and principle of operation are established, paving way for justification of the materials selection and analytical model of the device.

Chapter 3 is a discussion on sensor fabrication and preliminary bench top testing with rabbit cornea. In vitro and ex vivo experiments are conducted to validate proof of concept.

In *chapter 4*, the effects of temperature, incident angle, and substrate coating are studied. Each of the external factors are isolated to study their effect on sensor behavior and readout capability.

Chapter 5 is a detailed discussion of the three generations of handheld readers that were developed in order to obtain optical data from the sensor. With each generation, additional features were added to increase field of view, stabilization, autofocusing, and Android app integration.

Chapter 6 is a comprehensive study on various implant carriers to anchor the sensor. In this study, further proof of concept is conducted to verify feasibility of implanting the sensor. The sensor was implanted using three types of carriers: intraocular lens, capsular tension ring, and the iris claw. Ex vivo results were obtained for each carrier type and surgical observations were recorded.

Chapter 7 reports on in vivo results and discusses implantation of the sensor into New Zealand white rabbits. The rabbits underwent cataract surgery followed by 3 months of intraocular pressure monitoring to study the sensor's capability to measure intraocular pressure in vivo.

In *chapter 8*, image processing algorithms are discussed to demonstrate how interferometric data is correlated with pressure values. Algorithms were developed in MATLAB, employing mathematical models that characterize diaphragm deflection and built-in image analysis functions.

Chapter 9 presents a summary of the dissertation together with concluding remarks. Future directions of the study are provided with suggestions regarding how the sensing system can be improved. In addition, other potential sensor carriers are discussed along with future large-scale animal studies.

Chapter 2

Design of an Implantable Intraocular Pressure Sensor

2.1 Design Parameters and Requirements

There are many design requirements that govern the engineering aspect of an implantable intraocular pressure sensor. The challenges faced by sensors proposed in the literature primarily focus on validating and evaluating the design criteria that determine the feasibility and efficacy of the sensor in the eye environment. Among the many engineering considerations, it is important to demonstrate and characterize the following parameters in an implantable pressure sensor: long-term stability, implantability, system biocompatibility, sensitivity, accuracy (resolution), selectivity, reproducibility, sensor drift, hysteresis, operating life, small form factor, and operating range.

The parameters listed encompass both active and passive sensors in the IOP device space. In this dissertation, we focus on passive sensors as they have more desirable characteristics (no complex internal circuitry; no power source) than active sensors. In the context of the engineering parameters listed above, our proposed sensor must be passive, biocompatible, maintain long-term stability in the eye, accurate (less than ± 1 mmHg error), have reproducible measurements, exhibit a small form factor (sub millimeter cubed), have

near zero hysteresis, and operate within the physiologically relevant pressure range of 0 mmHg – 60 mmHg.

Throughout this dissertation, each parameter will be addressed in a series of experiments that validate our proposed optical interferometric pressure sensor.

2.2 Intraocular Pressure Measurement System

Intraocular pressure measurement systems proposed in the literature are typically limited by system design and implementation due to size, sophisticated data acquisition method, and readout distance. To overcome those challenges, our proposed intraocular pressure measurement system utilizes an optical approach in which measurements can be obtained wirelessly and passively.

As shown in Figure 2.1, the system is comprised of a submillimeter ($< 1\ mm^3$) size implantable pressure sensor and an optical readout unit. To ensure ease of implantation and fixed orientation, the sensor is anchored on an intraocular lens or capsular tension ring (carrier). Once the sensor is implanted, the optical reader can optically measure pressure by generating and capturing interference patterns from the IOP sensor. This is achieved through the configuration of a monochromatic light source, a lens system, and a camera shown in Figure 2.1.

The design of the IOP measurement system enables ease of integration and usage in practical settings such as clinical offices (integrated with slit lamps) or patient point-of-care settings (as a portable handheld reader).

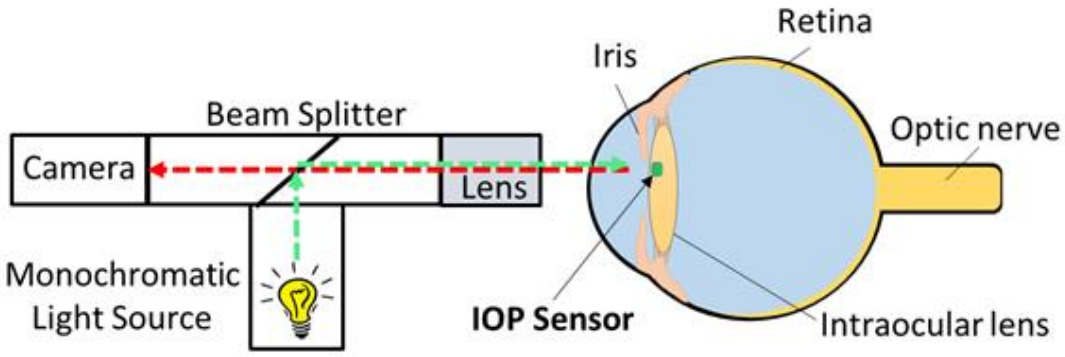

Figure 2.1: Optical intraocular pressure measurement system with implanted sensor and a portable handheld reader.

2.3 Principle of Operation

2.3.1 Interferometry

Interferometry is a method in which electromagnetic waves are superimposed to generate constructive or destructive interference (resultant waves with larger, smaller, or same amplitude) [109-110]. The superposition of the waves results in fringes as shown in Figure 2.2.

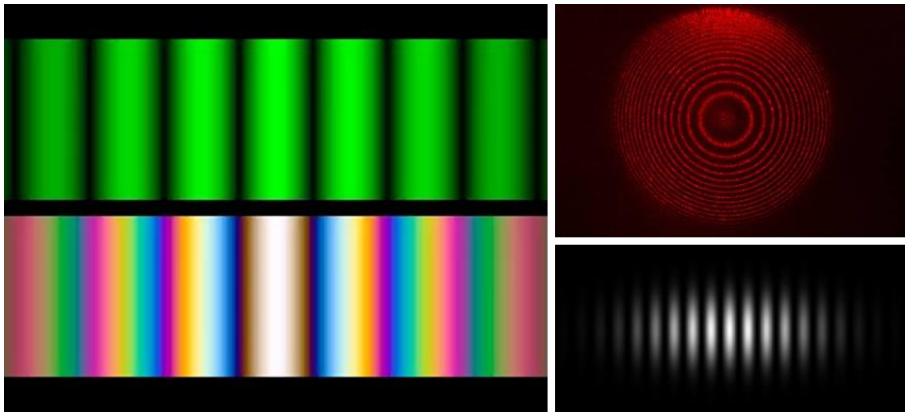

Figure 2.2: Example of interference fringes in different applications [111-112].

Since its discovery in the 1800s by Thomas Young, an English physician, interferometry has been an integral aspect in many applications requiring sensitive measurements of changes in distance [113-114]. Interferometers can be found for example in telescopes (astronomy), hard disk drive research, optical coherence tomography, chemistry, quantum mechanics, biomolecular interactions, surface profiling, and optometry [115-119].

There are various classes of interferometers depending on the configuration of the reference surface, light source, beam splitter, and test surface. The most common types of interferometer are Michelson, Fizeau, Fabry Perot, Mach-Zehnder, Linnik, and Twyman-Green interferometers [120-121]. Each interferometer varies in configuration, light source, and components to generate interference fringes.

The most common interferometer is the Michelson interferometer as shown in Figure 2.3.

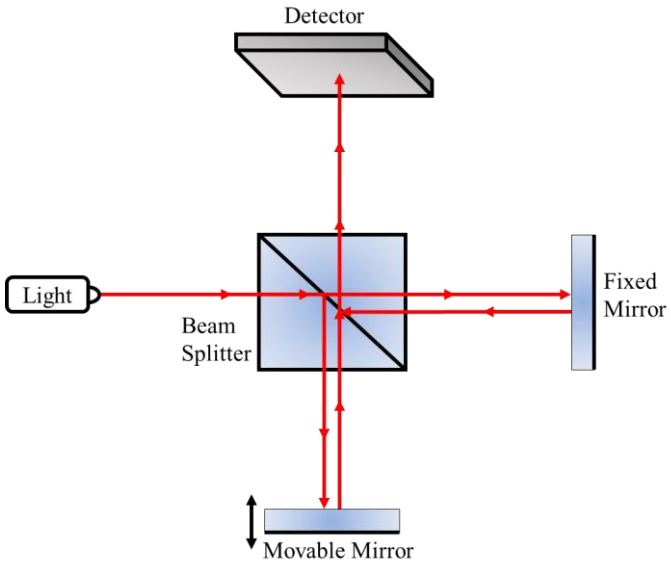

Figure 2.3: The Michelson interferometry utilizes two mirrors to interfere light at the beam splitter and captures the fringes using a detector.

In this configuration, the Michelson interferometer consists of a light source, a beam splitter that splits the light wave, a reference mirror and a reflecting sample surface, and a detector that captures the interference occurring at the beam splitter.

Among all the types of interferometers, the Fizeau interferometer was selected in our work as the operating principle of the sensor due to its simple configuration and ease of coupling with membrane deflection.

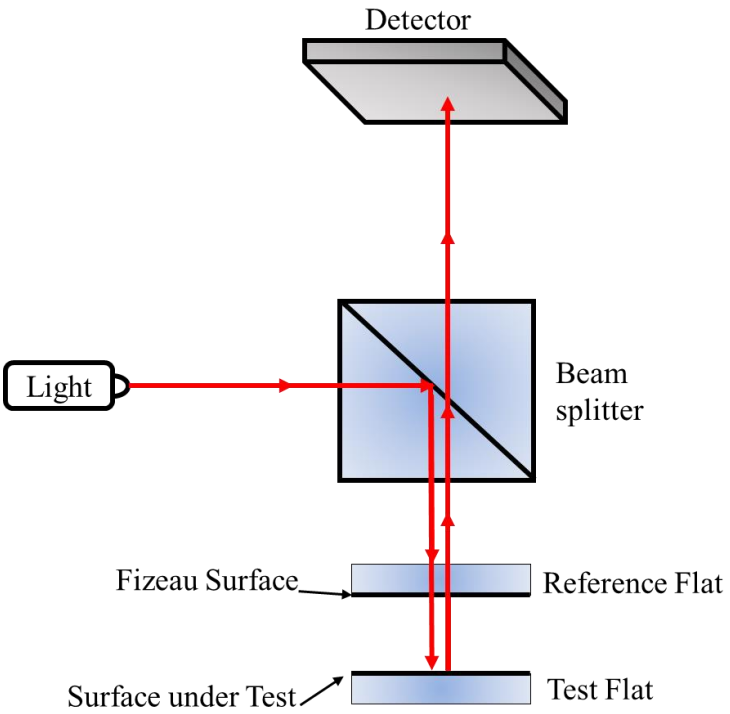

Figure 2.4: Configuration of the Fizeau interferometer. The system is comprised of a reference flat surface, a test flat surface, detector, and light source.

Figure 2.4 shows the configuration of a typical Fizeau interferometer. Light traveling from the light source passes through a beam splitter reflects off the top surface of the test flat and the bottom surface of the reference flat. Both reflected beams interfere with each other and generate fringes which are captured by the detector.

2.3.2 Operation Principle of the IOP Sensor

As shown in Figure 2.5, the IOP sensor consists of a flexible diaphragm, a rigid glass substrate and a spacer to form a cavity of height *h*. As the external pressure increases, the diaphragm deflects inward, reducing the gap distance *d(x,y)*.

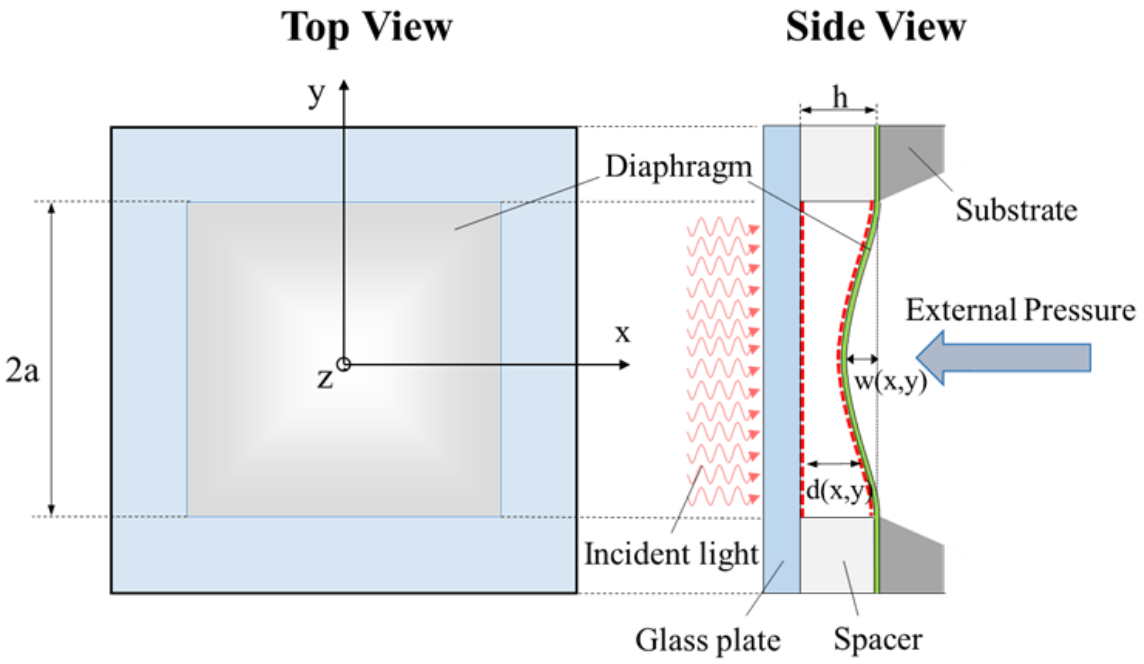

Figure 2.5: Schematic of sensor components: glass substrate, spacer and flexible diaphragm.

The principle of Fizeau interferometry is depicted with respect to the optical sensor shown in Figure 2.6. Monochromatic light with coherence length $L_c > 2h$ is directed at the sensor cavity. Interference of light reflected from the bottom surface of the glass substrate (R1) and the top surface of the diaphragm (R2) results in bright and dark fringes depending on the spacing *d(x,y)* and the phase difference $\Delta\phi(x,y)$ between the two interfering light beams. The phase difference $\Delta\phi(x,y)$ is a function of the path difference of the two light beams and can be expressed as a function of the gap distance *d(x,y)* as

$$\Delta\phi(x,y) = \frac{4\pi}{\lambda} d(x,y) + \pi \qquad 2.1$$

where λ is the wavelength of the incident light and π is the phase shift occurring at the top surface of the diaphragm, i.e., at the transition from an optically thin medium to an optically thick medium.

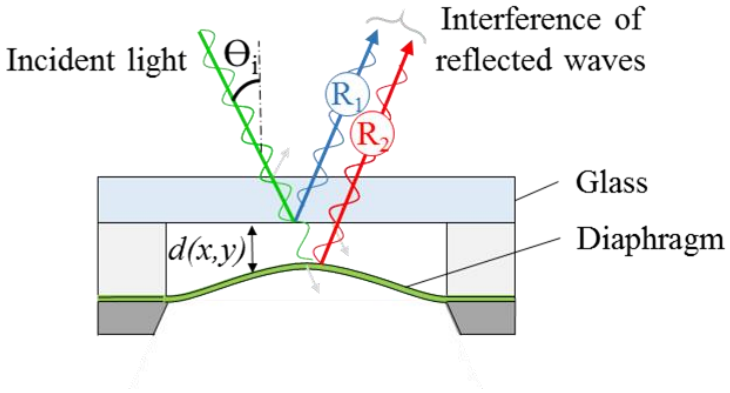

Figure 2.6: Schematic of light reflections at the sensor cavity. Incident angle θ_i is 0°. Light paths are drawn at an angle for illustration purposes.

The gap distance is defined as $d(x,y) = h - w(x,y)$, where h is the spacer thickness and $w(x,y)$ is the diaphragm deflection. Thus, as the gap distance $d(x,y)$ varies across the deflected diaphragm, interference fringes of difference intensity can be observed. The change in fringe pattern can be utilized to determine the applied pressure *P*.

In Figure 2.7 (a) and (b), a typical interference pattern is shown for a "low pressure" condition in which a small deflection of the diaphragm correlates with a small number of fringes. In Figure 2.7 (c) and (d), a fringe pattern is shown for a "high pressure" case, where a larger deflection of the diaphragm correlates with a higher number of fringes.

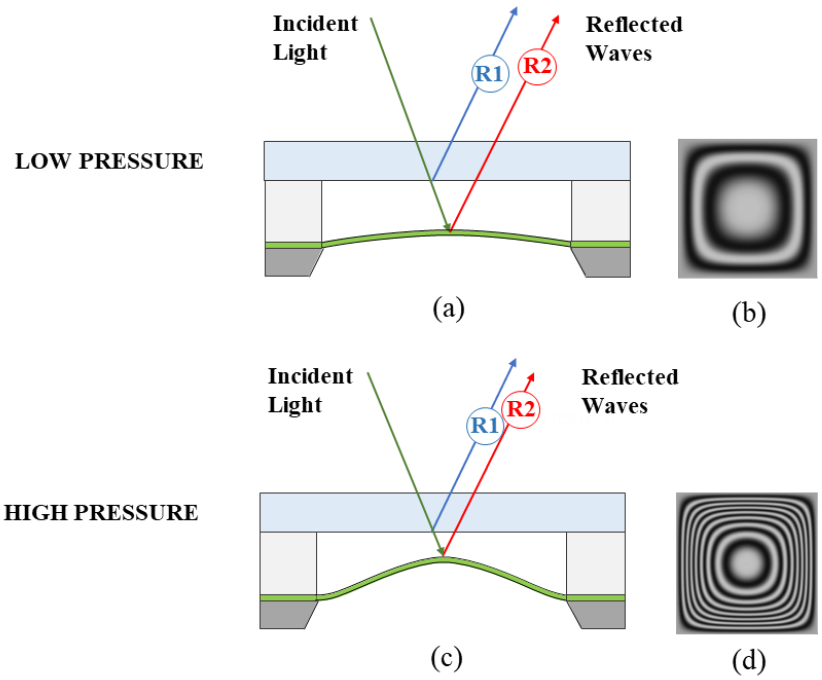

Figure 2.7: Schematic of sensor operation. Diaphragm deformation under (a) low pressure and (c) high pressure. Simulated resulting concentric interference patterns (from top view) under monochromatic light for (b) low pressure and (d) high pressure.

2.4 Conditions for Obtaining Quality Fringes

There are several conditions that influence the appearance and the quality of the interference fringes from the sensor described above. As the two reflected waves interfere with each other, interference fringes can only be observed if they are coherent with each other. Both temporal coherent and spatial coherent conditions must be satisfied within the region of interest. The surface roughness of the diaphragm and the glass substrate must be sufficiently small for high optical performance [122]. Visibility, a measurement of the quality of the interference fringes, is also a very important parameter in characterizing the fringes. We will discuss more about visibility and optimization of visibility in Chapter 4.

2.4.1 Temporal Coherence

Temporal coherence is used to characterize how well two light beams interfere with each other over time. Though two beams can originate from the same light source, their phases and amplitudes can deviate from the nominal values over time. As this happens, their correlation decreases significantly, and the beams become incoherent. Temporal coherence is proportional to the central wavelength, λ, and inversely proportional to the spectral bandwidth, Δλ, of the light source. The temporal coherence length, L_c, the coherence time, t_c, are determined using the following equations:

$$L_c = \frac{\lambda^2}{\Delta\lambda} \tag{2.2}$$

$$t_c = \frac{L_c}{c} \tag{2.3}$$

where c is the speed of light [123].

Table 2.1: Example of temporal coherence length of various light sources.

Light Source	**λ (nm)**	**Δλ (nm)***	**L_c**
HeNe Laser	632.8	< 0.001	> 40 mm
LED (1 nm)	632.8	1	400 µm
LED (10 nm)	632.8	10	40 µm
Broadband LED	430-660	~200	~1 µm

*Spectral bandwidth is measured at full width at half maximum (FWHM) of the spectrum

2.4.2 Spatial Coherence

The two light waves reflecting from the cavity of the sensor must also be spatially coherent to create interference. In an ideal monochromatic point source, the characteristics of the light waves are identical except for the optical path difference. Hence, the visibility of the fringe pattern remains spatially constant. However, in application, monochromatic light sources are not ideal point sources, and there exists phase variations across the beam profile of the light source. As a result, the quality of the interference fringes spatially degrades depending on the uniformity of the wavefront of the light source.

Illustrations of interference patterns generated from monochromatic light sources with different coherent characteristics are shown in Figure 2.8.

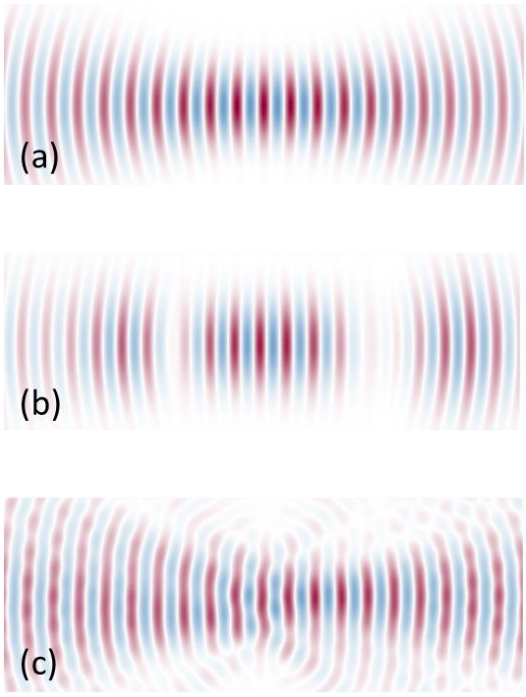

Figure 2.8: Illustrations of interference patterns generated from monochromatic light sources with different coherent characteristics: (a) high temporal and spatial coherence, (b) poor temporal and high spatial coherence and (c) high temporal and poor spatial coherence [124].

2.5 Diaphragm Consideration

2.5.1 Material

In micro-electro-mechanical system (MEMS) and micro-opto-mechanical system (MOMS) devices, diaphragms are used in a variety of ways, namely as barriers, filters, sensors, or actuators [125-126]. Applications of diaphragms as sensing elements in pressure transducers are of interest when developing an IOP sensor. When a diaphragm mechanically deflects under a pressure load, one can measure and relate the displacement to the applied pressure using physical (strain gauges, piezo-resistors, capacitance) or optical means (interferometry, photoelasticity). Depending on the required operating range of the sensor, diaphragm material selection varies across applications. For instance, capacitive pressure sensors are typically comprised of a silicon, silicon dioxide, silicon nitride, or steel diaphragm [127].

In our unique application to develop an interferometric IOP sensor, design parameters require the diaphragm to be tear resistant, biocompatible, and have optical characteristics (refractive index, transmittance) and surface characteristics capable of generating interference patterns. Since the physiological pressure range is relatively small (0 – 60 mmHg), the diaphragm of the pressure sensor is desired to be thin to increase sensitivity.

Among the various diaphragm materials such as polymers, metals, and silicon, silicon nitride was selected to be used as the material for the diaphragm of the IOP sensor due to its desirable features that fulfill the optical and mechanical design criteria.

The important features of silicon nitride include its strength and the capability to withstand high pressure loads. Table 2.2 shows typical burst pressure for silicon nitride diaphragm (Norcada) at various sizes and thicknesses [128]. Mechanical and optical characteristics of the diaphragm heavily depend on the fabrication methods used to process the material. In our application, it was ideal to utilize diaphragms with low residual stress (<250 MPa) to achieve a high deflection range, and low surface roughness (rms < 0.5 nm) for best optical properties.

Finally, silicon nitride is considered a biocompatible material (FDA approved) and has been tested in biological environments [129-131].

Table 2.2: Burst Pressure (PSI) for various Norcada silicon nitride diaphragms [128].

	1 mm x 1 mm	1.5 mm x 1.5 mm	2 mm x 2 mm
100 nm	40	25	20
200 nm	60	50	40
500 nm	70	60	50

2.5.2 Shape of Diaphragm

During the development of the IOP sensor, we considered both square diaphragms and circular diaphragms. There are different advantages and disadvantages of each of the two shapes. From an optical stand point, both circular and square diaphragms can generate interference fringes that can be captured and analyzed. From a mechanical point of view, using a circular diaphragm with the same area as a square diaphragm offers some advantages when subjected under the same pressure load: (1) a circular diaphragm deflects more symmetrically and experiences lower stress along the edges, (2) the maximum

defection at the center of a circular diaphragm is slightly larger than that of a square diaphragm which improves the sensitivity of the sensor. Therefore, a circular diaphragm is preferred for applications that are concerned with maximum deflection [132]. On the other hand, a square diaphragm is the preferred choice from a fabrication point of view. Although, both diaphragms are generally made using standard MEMS techniques (e.g., thin film deposition, etching), the fabrication process is very different. Figure 2.9 outlines the typical fabrication steps in making a square [133] and a circular diaphragm [134].

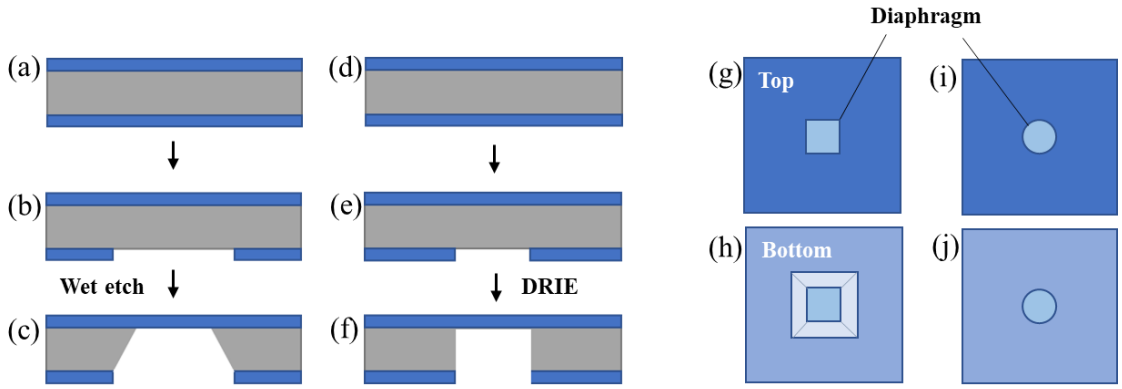

Figure 2.9 Schematic of typical fabrication steps for diaphragm using standard MEMS technique: (a-c) square diaphragm and (d-f) circular diaphragm. Front and back side of the diaphragm: (g-h) square diaphragm and (i-j) circular diaphragm.

To fabricate a square diaphragm, substrates are submerged in etchants with high selectivity to silicon (e.g., KOH, EDP) to remove material from the back side. This process is commonly referred to as wet etching. Due the crystal lattice structure of silicon, the wet etching process is highly anisotropic as shown in Figure 2.10. The etch rates of each of the lattice plane differ by several order of magnitudes. This leads to the formation of a square cavity and a square diaphragm.

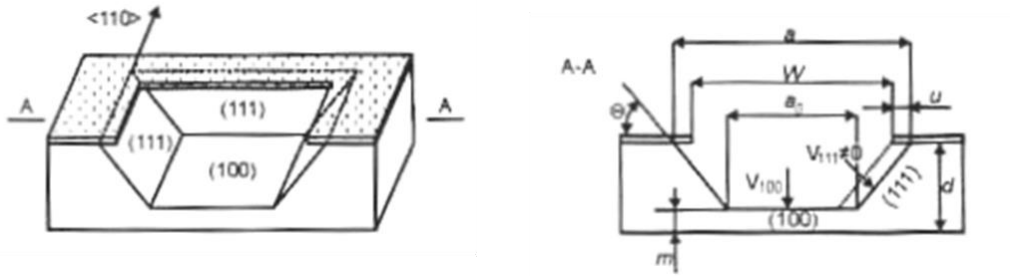

Figure 2.10: Selectivity of wet etching of silicon substrate: <100> plane is etched at a much faster rate than <111> plane [134].

Fabrication of circular diaphragms typically requires the use of deep reactive ion etching (DRIE) to remove silicon in the perpendicular direction to the substrate. This technique can produce very high aspect ratio features with essentially any desired shapes. The main drawback is that it is slow and expensive. Therefore, circular diaphragms are specifically made only for certain applications and generally not commercially available.

Because of the above reasons, square diaphragm was used exclusively early in the development process of the IOP sensor and the circular diaphragm was implemented in the later stages.

2.6 Analytical Model and Simulation

In this section, we discuss the analytical models and simulation of the deflection of both diaphragms. Analytical models for thin film diaphragms have been studied extensively in the literature [135-136].

2.6.1 Square Diaphragm Deflection

The deflection *w(x,y)* of a square SiN diaphragm can be determined using the shape function approach presented by Rahman et al. [137] and is given by

$$w(x,y) = w_0\left(1-\frac{x^2}{a^2}\right)^2\left(1-\frac{y^2}{a^2}\right)^2\left[1+2.46\left(\frac{x^2+y^2}{a^2}\right)^n+1.12\left(\frac{x^2+y^2}{a^2}\right)^n\right] \quad (2.4)$$

In Equation (2.4), the maximum deflection $w_0 = w(0,0)$ at the center of the membrane is related to the applied pressure by

$$P = \left[3.45\left(\frac{\sigma_0 t}{a^2}\right)\right]w_0 + \left[4.06\left(\frac{Et^3}{(1-v^2)a^2}\right)\right]w_0 + \left[1.994\,\frac{1-0.271v}{1-v}\left(\frac{Et}{(1-v)a^4}\right)\right]{w_0}^3 \quad (2.5)$$

where t, E, and ν are the thickness, Young's modulus, and Poisson's ratio of the diaphragm, respectively [138]. The first term in Equation (2.5) represents the contribution of the residual stress σ_0 from the fabrication process. The second and third terms account for bending stiffness and in-plane strain from the deformation of the diaphragm, respectively.

2.6.2 Fresnel Reflection and Thin Film Interferometry

A schematic of the light pathways at the sensor interfaces is shown in Figure 2.11. The interfaces are labeled from 1 to 4. R_1, R_2, R_3 and R_4 denote the fraction of light reflected at each interface. We assume that the incident light angle $\Theta_i = 0$.

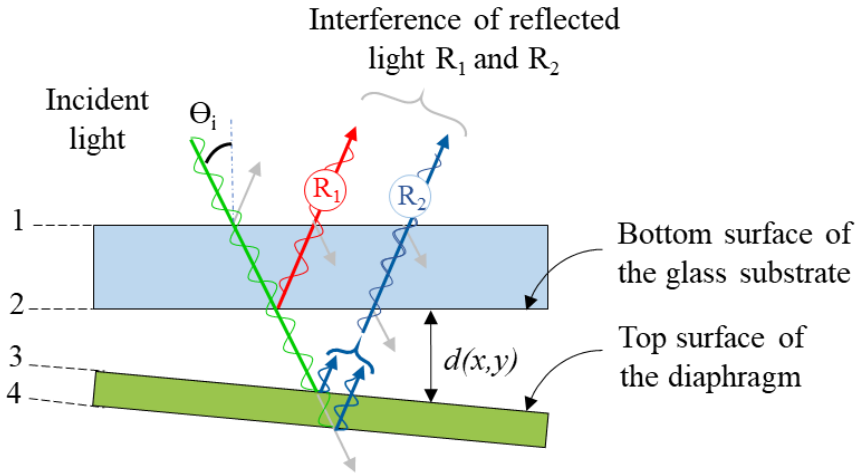

Figure 2.11: Schematic of light reflections at the sensor interfaces. Incident angle $\Theta_i = 0$. Light paths are drawn at an angle for illustration purposes.

When light travels through the glass substrate, the fractions of light reflected from the top and bottom surface of the substrate (interfaces 1 and 2) are given by:

$$R_1 = R_2 = \left(\frac{n_a - n_g}{n_a + n_g} \right)^2 \tag{2.6}$$

where n_a, n_g, n_d are the refractive indices of air and glass, respectively [139]. When light travels through the SiN diaphragm, thin film interference phenomena must be considered since the thickness of the SiN diaphragm lies within the wavelength and the coherence length of the light source. In this case, the light reflected from interface 4 interferes with the light reflected from interface 3 creating a resultant reflection. The resultant reflection from the SiN diaphragm R_{34} is given by: [139]

$$R_{34} = \frac{R_3^2 + R_4^2 + 2\sqrt{R_3 R_4}\cos\left(\frac{2\pi n_d t_d}{\lambda}\right)}{1 + R_3^2 + R_4^2 + 2\sqrt{R_3 R_4}\cos\left(\frac{2\pi n_d t_d}{\lambda}\right)} \tag{2.7}$$

where λ is the wavelength of the incident light, t is the thickness of the SiN diaphragm, n_d is the refractive index of silicon nitride, and R_3 and R_4 are given from Equation (2.6).

2.6.3 Sensor Modeling

In this section, we discuss the simulated mechanical and optical responses of the IOP sensor. Table 2.3 shows the parameters of the monochromatic light source and material properties of the diaphragm used in the simulation.

Table 2.3: Modeling parameters for the monochromatic light source and the silicon nitride diaphragm

Monochromatic Light Source	**Silicon Nitride (SiN) Diaphragm**
Central Wavelength λ = 632.8 nm	Young's Modulus E = 270 GPa
Spectral bandwidth $\Delta\lambda$ = 1 nm	Poisson's Ratio ν = 0.27
	Residual Stress σ = 135 MPa

In this model, we focused on the response of the SiN diaphragm and neglected the pressure inside the cavity of the sensor and its effect on the response of the sensor. Using equations (2.4) and (2.5), the deflection profile $w(x, y)$ and the maximum deflection w_0 of the square SiN diaphragm for a pressure load P were determined. Material properties of the silicon nitride were obtained from the technical data sheet of a commercially available diaphragm (Norcada): Young's modulus E = 270 GPa, Poisson's ration ν = 0.27 and fabrication residual stress σ = 135 MPa. The dimensions of the diaphragm are t = 200 nm and a = 250 μm. Figure 2.12 shows the deflection profile of the silicon nitride diaphragm under a pressure load of P = 20 mmHg. The maximum deflection w_0 at the center of the diaphragm is 1.66 μm. Figure 2.13 shows simulated fringe patterns observed when a monochromatic light (λ = 632.8 nm) is directed at the sensor at various pressures from 10 mmHg to 40 mmHg.

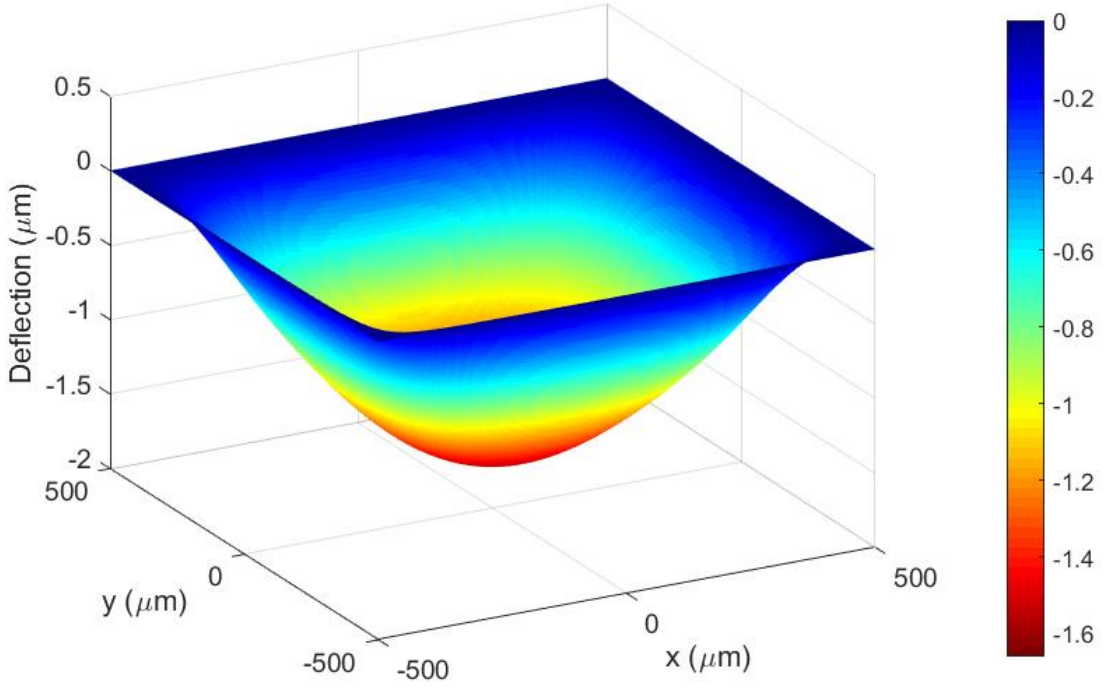

Figure 2.12: Deflection profile of a silicon nitride diaphragm (t = 200 nm, a = 250 μm, E = 270 GPa, ν = 0.27, σ = 135 MPa) under a pressure load of P = 20 mmHg.

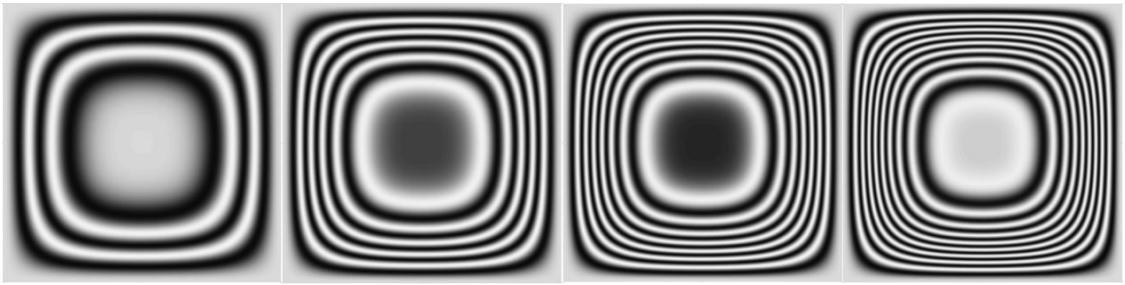

Figure 2.13: Simulated fringe patterns at various pressures: 10 mmHg, 20 mmHg, 30 mmHg and 40 mmHg (from left to right).

2.7 Summary

In this chapter, we proposed an intraocular pressure measurement system comprised of an implantable sensor and an optical reader. By applying a combination of principle of interferometry and mechanical deflection, we were able to develop a purely optical battery-free sensor. As monochromatic light directed at the cavity of the sensor, reflective waves at top and bottom the cavity of the sensor interfere with each other to form interference fringes. The handheld reader is used to wirelessly and optically capture these fringe patterns for analysis to determine the pressure.

Temporal and spatial coherence is also discussed with respect to fringe visibility to guide material selection and cavity dimension of the sensor. A model of mechanical and optical response of the sensor was developed based on the theory of diaphragm deflection and interferometry to validate the concept of measuring pressure using an opto-mechanical approach.

Chapter 2, in part is a reprint of the material as it appears in " Design of an Optical Pressure Measurement System for Intraocular Pressure Monitoring," Phan, Alex, Phuong Truong, Julian Trumpp, and Frank E. Talke, IEEE Sensors Journal, vol. 18, no. 1, 2018, pp. 61–68. The dissertation author was the primary investigator and author of this paper.

Chapter 3

Sensor Fabrication and Testing

3.1 Fabrication of IOP Sensor

The interferometric IOP sensor was fabricated using common MEMS processes, e.g., photolithography and PECVD. The sensor consists of three main components: a transparent substrate, a thin diaphragm and a spacing layer. In this section, we will discuss a novel 2-stage bonding technique used to integrate these components together to make the sensor. The main fabrication process consists of patterning the glass substrate with SU-8 (a photoresist), bonding the substrate to the SiN diaphragm and dicing the sensor to final size.

3.1.1 Overview of Fabrication Process

In a typical capacitive or piezoelectric pressure senor, the reference cavity is preferred to be in vacuum. This would increase the sensitivity of the sensor and avoid any thermal effects caused by the presence of gas inside the cavity. However, having low pressure or vacuum inside the cavity of the sensor would not be ideal for an interferometric pressure sensor. Low internal pressure would cause the diaphragm of the sensor to deflect inward significantly under atmospheric pressure. This would produce a large number of fringes, which would make distinguishing bright and dark fringes during image processing

challenging. Therefore, a 2-stage bonding approach was developed to fabricate the IOP sensor in such a way that the pressure in the cavity of the sensor remains close to atmospheric pressure. As a result, zero offset of the sensor under no-load conditions is minimal.

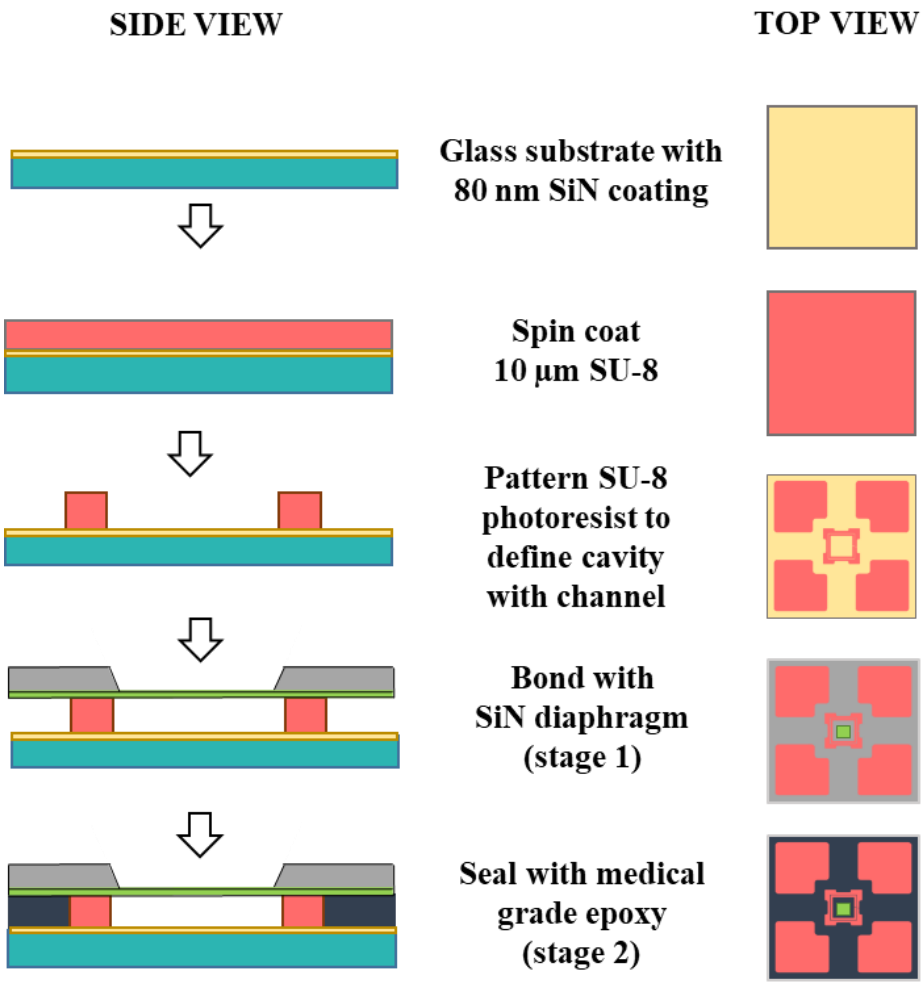

Figure 3.1: Schematic of the 2-stage bonding technique: SU-8 was first patterned on the glass substrate. SU-8 bonded the SiN diaphragm to the glass substrate in first bonding stage and medical grade epoxy enclosed the SU-8 layer and sealed off the sensor cavity in the second bonding stage.

In the first bonding stage, SU-8 photoresist was used to define the cavity wall of the sensor on the glass substrate (Figure 3.1). A small channel was included in the SU-8 wall to allow pressure to equilibrate between the inside and outside of the cavity. Next, we

aligned and bonded the diaphragm to the glass substrate under high pressure and temperature. After the first bonding stage, the pressure inside the cavity remained at atmospheric pressure. In the second bonding stage, medical grade epoxy was used to enclose the outer surface of the SU-8 wall and seal the cavity of the sensor. This bonding stage occured slowly at room temperature, ensuring the pressure inside the cavity of the sensor to remain close to atmospheric pressure.

Design of the SU-8 bonding pattern and details of each of the fabrication steps will be discussed in the following sections.

3.1.2 Design of SU-8 Bonding Pattern

SU-8 photoresist has been used for many different applications ranging from support structures [140] to bonding materials [141] and sensing elements [142]. SU-8 has been shown to have good thermal property (glass transition temperature > 200°C), excellent chemical stability and good mechanical property [143-144]. Unlike common photoresists, SU-8 has very high viscosity, which allows for fabrication of very high aspect ratio structures.

In this research, SU-8 was patterned on glass substrate to serve two functions: (1) define the dimensions of the cavity and (2) acts as bonding layer between the diaphragm and the substrate. A thin channel was incorporated into the SU-8 wall of the cavity to allow pressure to equilibrate at the end of the first bonding stage, which is performed at high temperature.

Several designs for channel path and cavity wall were considered to minimize the SU-8 footprint but at the same time provide enough stability during the high-pressure

bonding process. As shown in Figure 3.2, various designs were drawn in AutoCAD, printed on transparency masks (CAD/Art Services) and used in the photolithography process to make the SU-8 patterns on glass substrates.

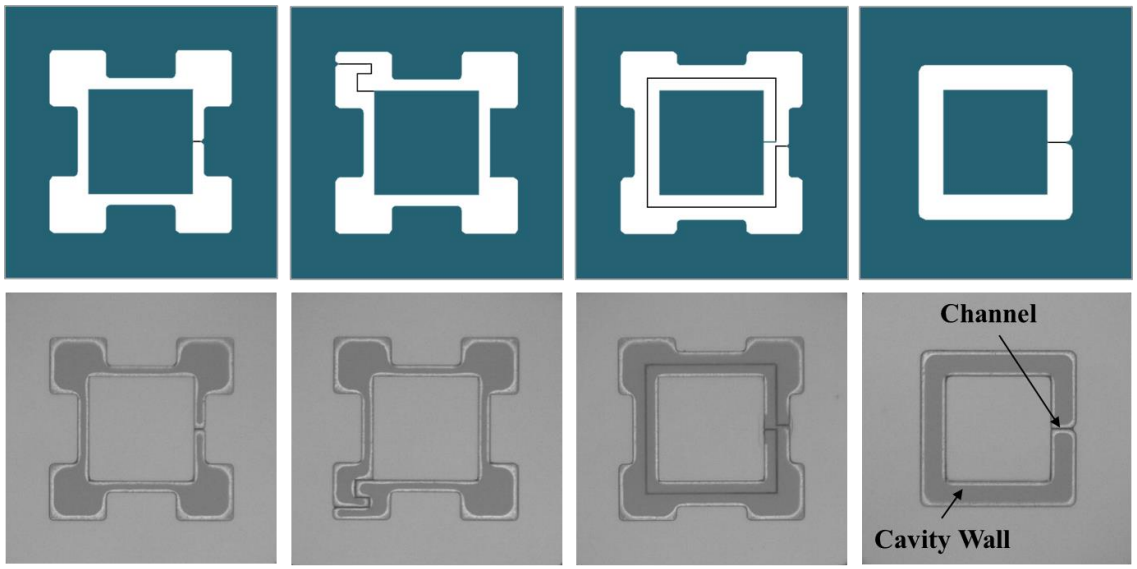

Figure 3.2: Various designs of SU-8 patterns for cavity wall and cavity channel (top row), and pictures of corresponding fabricated SU-8 patterns on glass (bottom row).

The width of the channel should be minimized to prevent the flow of epoxy into the cavity in the second bonding stage. The optimal channel width on the transparency mask was found to be 10 µm since smaller dimensions led to incomplete channel clearances as shown in Figure 3.3.

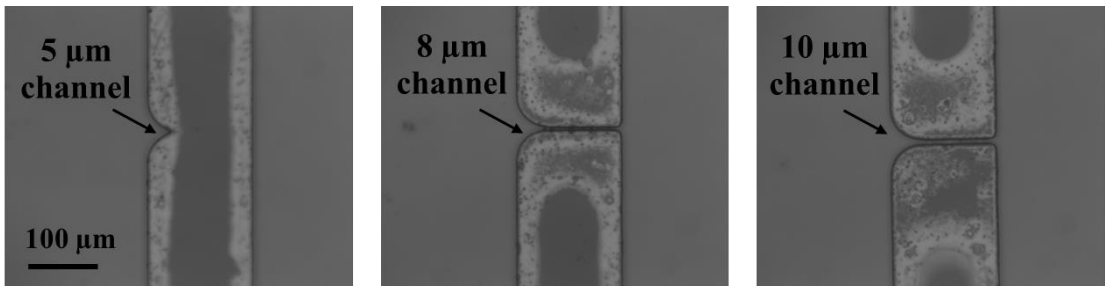

Figure 3.3: Fabrication limit of the width of the channel.

3.1.3 Glass Substrate

We used 200 μm Borofloat 33 glass 4" wafer (University Wafer, Inc.) in all of our substrate fabrication. The glass wafer was first cleaned using acid piranha solution, a 3:1 mixture of H_2SO_4 and H_2O_2. This process removes any organic contaminants and residues on the glass wafer and facilitates stronger adhesion of subsequent coating steps. Next, an 80 nm film of silicon nitride was deposited onto the glass wafer using PECVD (plasma enhanced chemical vapor deposition) Oxford Plasma Lab 80. After a dehydration bake at 180°C for 15 minutes, SU-8 2010 photoresist (Micro Chem) was spun on the glass wafer in two steps to create a uniform coating layer: 500 rpm for 10 seconds and 3000 rpm for 30 seconds. SU-8 is known to have weak adhesion to glass wafers [145-146] due to the thermal coefficients mismatch between the photoresist and the glass wafer. Therefore, it is very important to ramp the temperature up and down very slowly during the soft bake process to improve the adhesion between the two materials. We developed and used a modified baking process rather than of following the manufacture recommended procedure for baking SU-8. The wafer was placed on the hot plate at 45°C and the temperature was increased to 65°C. After the wafer was soft baked at 65°C for 5 min, the temperature was again increased slowly to 90°C. After a baking period of 10 minutes, the hot plate was turned off and the wafer was left on the plate to cool down to 60°C (about 20 minutes). The wafer was then taken off the hot plate and let to cool down to room temperature. Next, the exposure process was performed using a mask aligner (EVG6200) at 13W for 30 seconds. Post exposure bake was performed using the same heating and cooling procedure as the soft bake process. A diagram of this heating and cooling process is shown in Figure 3.4.

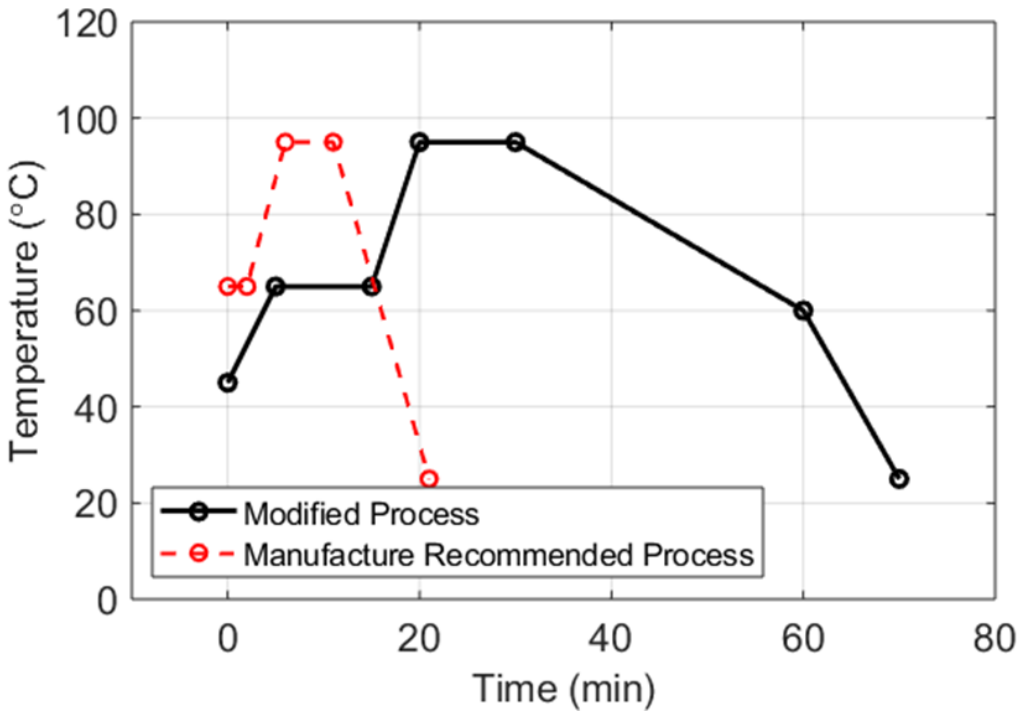

Figure 3.4: Heating and cooling procedure for the soft bake and the post bake processes.

After the wafer was cooled back down to room temperature, it was submerged in SU-8 developer for 3 min with light agitation for developing. The wafer was rinsed with SU-8 developer for another 10 seconds and cleaned with isopropanol alcohol for 30 seconds. After blow-drying using N_2, a stylus profilometer (Dektak 150) was used to verify the uniformity and thickness of the 10 µm SU-8 layer. The glass wafer was then diced down to 5x5 mm square substrates using wafer saw dicing (DISCO) as shown in Figure 3.5.

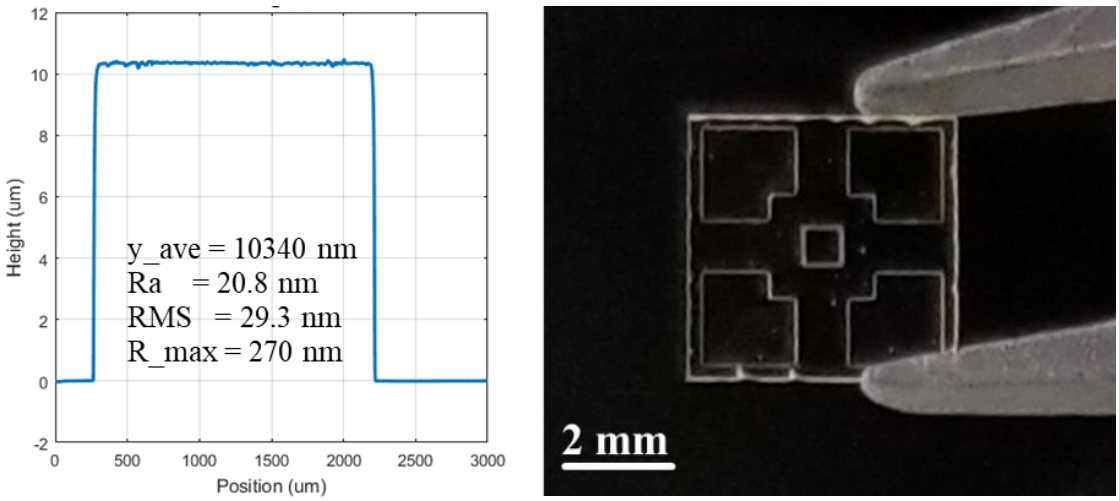

Figure 3.5: Glass substrate after processing: (a) surface profile using Dektak and (b) photograph of a diced glass substrate.

Figure 3.6 shows the SU-8 patterns on the glass substrate after processing using the manufacture recommended procedure and the modified procedure. The appearance of interference patterns shown in Figure 3.6 (a-d) indicates the present of an air gap between the SU-8 film and the glass substrate, i.e., the photoresist layer was peeling off. Ramping and stepping the soft bake and post bake temperature allowed the solvent in the SU-8 photoresist to evaporate out of the coating layer at a more controlled rate. This process helped reduce edge bead effect and, more importantly, increase adhesion of SU-8 to glass. Figure 3.6 (e-h) shows a uniform pattern SU-8 coated on top of the glass substrate when using the modified baking process.

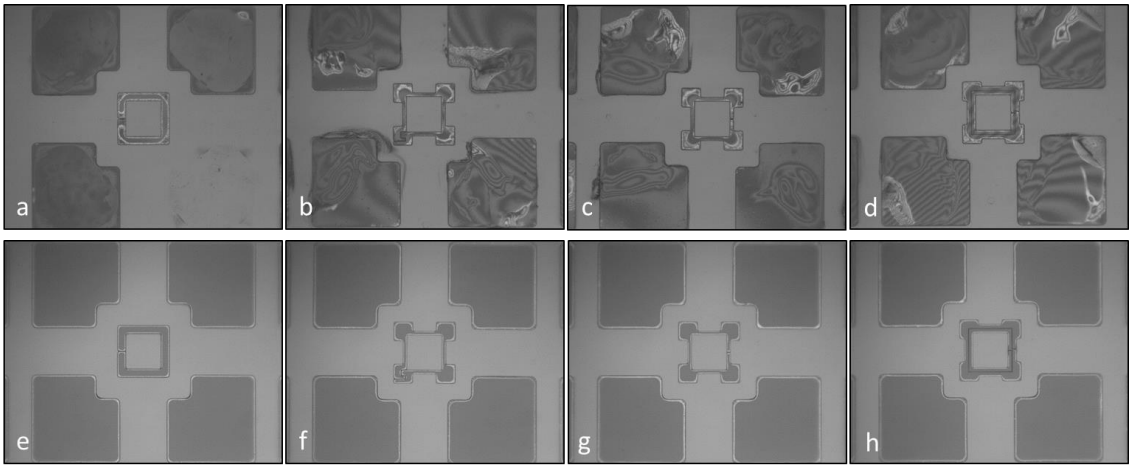

Figure 3.6: SU-8 patterns on glass substrate using (a-d) manufacturing recommended procedure and (e-h) modified procedure.

3.1.4 Silicon Nitride Diaphragm

Silicon nitride was selected to fabricate the IOP sensor diaphragm because of its superior mechanical, optical and biocompatible properties. Norcada Inc. is specialized in manufacturing thin diaphragms for transmission electron microscopy (TEM) and X-Ray microscopy. They offer a wide selection of SiN diaphragms mounted on silicon substrates that are well suited for fabricating the IOP sensor. We used both square and circular SiN diaphragms at various thicknesses (50-200 nm) and dimensions (250-600 μm) from Norcada in our studies. The diaphragms were mounted on 5 x 5 x 0.2 mm silicon substrates. Figure 3.7 shows photographs of typical square and circular diaphragms used in our sensor fabrication.



Figure 3.7: Photographs of Norcada silicon nitride diaphragm: (a) square and (b) circular [147].

3.1.5 Bonding

The next step in the fabrication process is to bond the SiN diaphragm to the diced glass substrate via a 2-stage bonding procedure. In the first stage, the 5 x 5 mm SiN diaphragm was first aligned to the 5 x 5 mm glass substrate using a silicon mold as shown in Figure 3.8. A custom-built clamping device was made to hold the sensor components together under a 2 MPa pressure load.

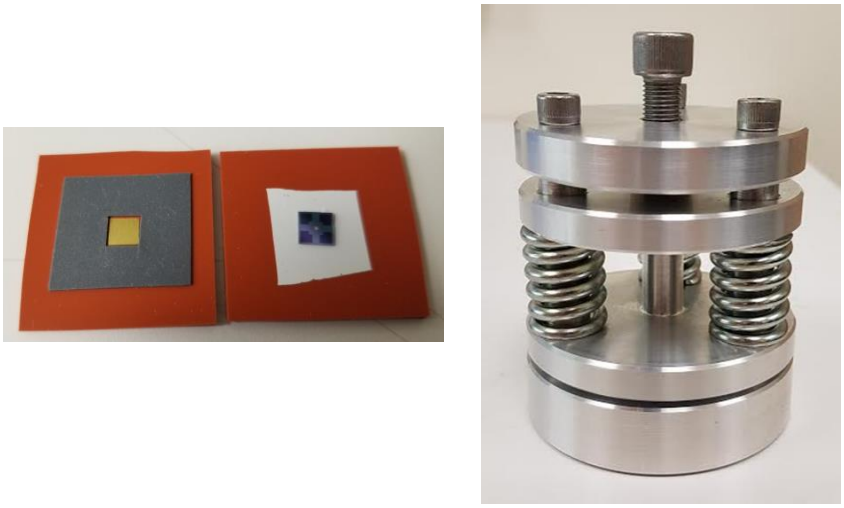

Figure 3.8: Photographs of bonding alignment setup using silicone mold (left) and custom-built clamping device for bonding (right).

While keeping under the pressure, the sensor components were then heated up to 110°C for 2 hours using a convection oven. Under this bonding condition, the SU-8 film acted as an adhesive layer and bonded the glass substrate and the silicon substrate together. Next, medical-grade epoxy (EPO-TEK 301-2) was applied on the outer edge of the sensor. As shown in Figure 3.9. the medical epoxy flowed in the gap between the glass and silicon substrate and closed up the bonding channel and reinforced the bonding strength between components. After two days, the epoxy was fully cured at room temperature.

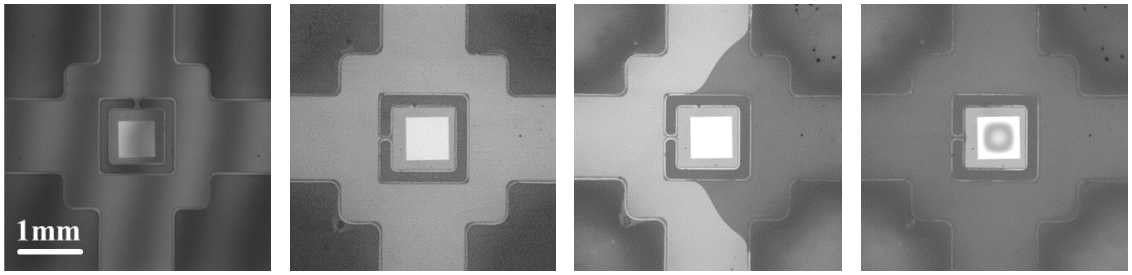

Figure 3.9: Photographs of the 2-stage bonding process: (a) aligned sensor components (b) after SU-8 bonding (stage 1), (c) epoxy bonding (stage 2), and sensor after bonding.

3.1.6 Packaging

Once the components were bonded together, the sensor was diced to a smaller size to reduce the footprint using a Disco Automatic Dicing saw (DAD3220). A diamond coated circular blade was used to dice the sensor in 200 μm steps. The dicing process can be considered as a bonding strength test as the sensor had to overcome the large shear force generated during blade dicing. For square diaphragm sensors, we only need four cut lines. However, for circular diaphragm sensors, we used 12 cut lines to create a near circular sensor footprint. Photographs of the sensor are shown in Figure 3.10. Finally, the sensor was coated with a 1 μm Parylene-C layer (SCS Labcoter 2), a biocompatible polymer commonly used in encapsulation processes for implantable devices [148].

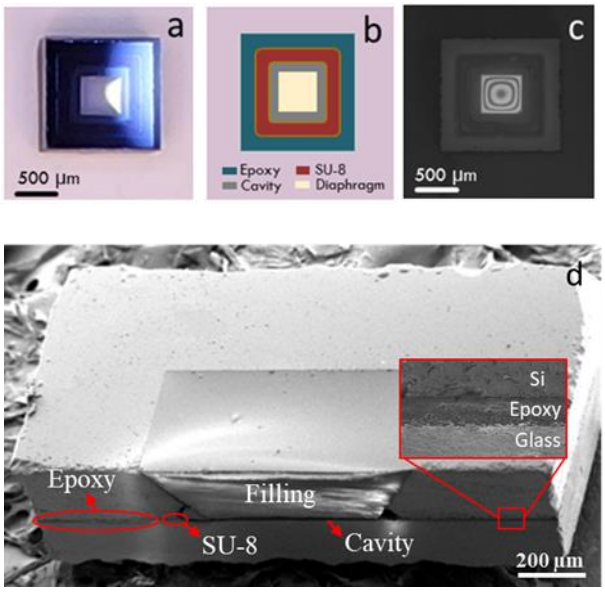

Figure 3.10: (a) Photograph of sensor (b) Schematic of sensor (c) Photograph of sensor under monochromatic light (d) SEM photograph of cross section of the sensor (epoxy filling was used to preserve the cavity of the sensor during cross section dicing).

3.2 Benchtop Testing of IOP Sensor

To evaluate the use of the sensor for the measurement of small changes in intraocular pressure, we first investigate the response of the sensor in an environment that represents the environment of the eye.

3.2.1 Experimental Setup

The bench top experimental set up for in vitro and ex vivo studies is shown in Figure 3.11. The set up consists of a microscope (Mitutoyo), a pressure regulator (MVP, Proportion Air), an artificial anterior chamber (Katena) and a 1.3MP CMOS camera (DCC3240M, Thorlabs). The bright field microscope with an internal beam splitter was used to direct monochromatic light (632.8 nm) at the sensor housing. Monochromatic light

was obtained by coupling a laser line filter (FL632.8-1, Thorlabs) with a white light source (Eiko EKE 150 W bulb). The temporal coherence length of the light was determined to be 330 µm which is sufficient to generate high quality interference patterns in our sensor. The intensity of the light delivered to the sensor was 2 µW (Newport). The camera was mounted to the microscope to capture the reflected light from the sensor as it travels through the beam splitter. The artificial anterior chamber was connected to a pressure regulated water column to adjust the fluid pressure inside the chamber. The sensor was secured inside the artificial chamber during testing to reduce motion-induced noise as the pressure is varied. As various pressure loads were applied, the interference patterns were captured and processed using MATLAB image analysis algorithms.

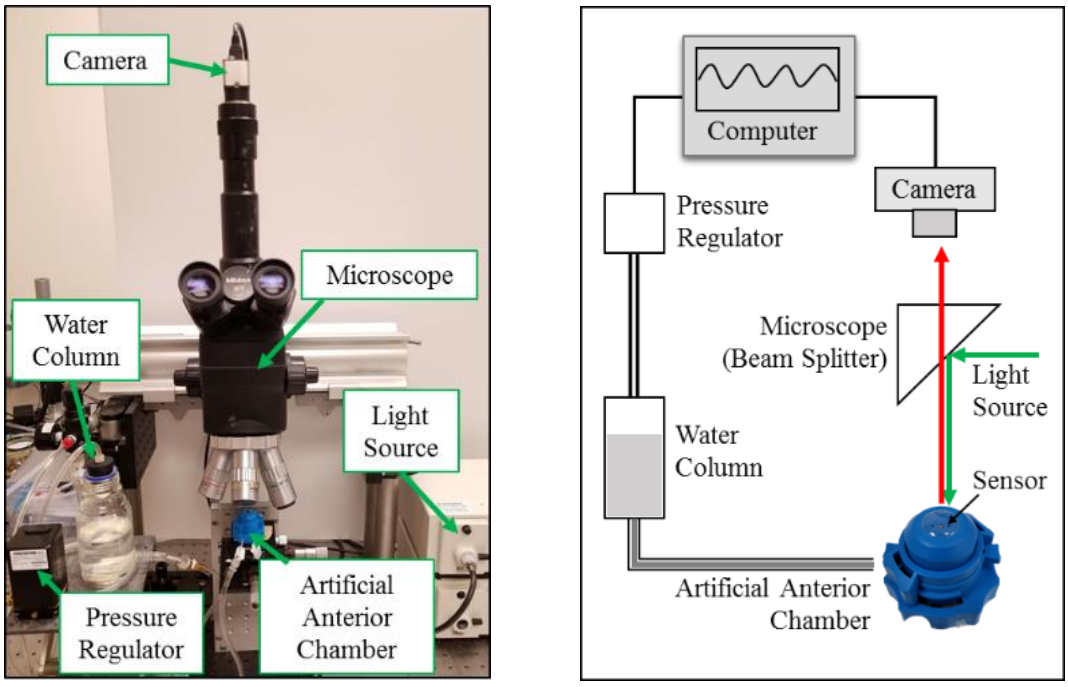

Figure 3.11: (a) Photograph of experimental setup (left) (b) Schematic of experimental setup (right).

3.2.2 In vitro Experiment Using Silicone Cornea

In the in-vitro experiments, silicone corneas (Figure 3.12a) were used. The silicone corneas were molded on a steel sphere with a radius of 8 mm to simulate the radius of curvature of a human eye. Silicone rubber (Dow Corning 734) was poured onto the steel sphere and allowed to coat the surface of the sphere under the effect of gravity [149]. After the silicone was fully cured (48 hr.), the top of the silicone mold was removed and mounted on the artificial anterior chamber for in-vitro testing.

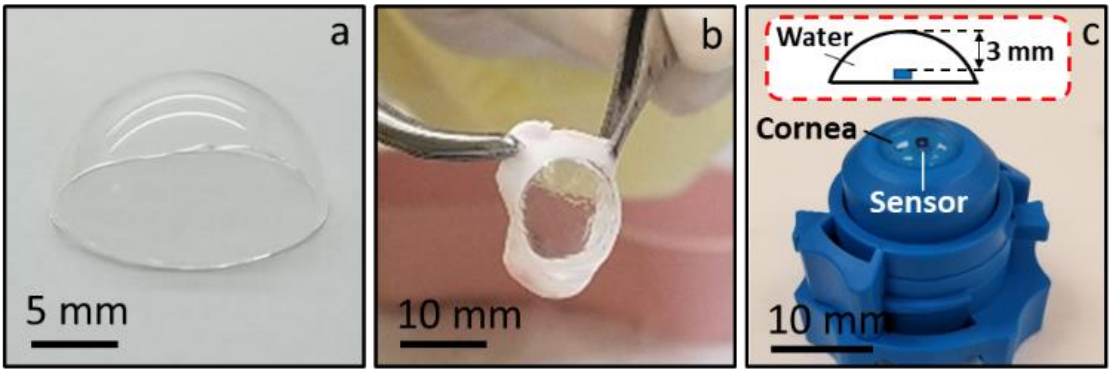

Figure 3.12: (a) Silicone cornea (b) rabbit cornea (c) sensor mounted in the artificial anterior chamber.

Hydrostatic pressure in the artificial anterior chamber was varied from 0 mmHg to 60 mmHg using a step size of 1 mmHg. In Figure 3.13, in-vitro results of the sensor response to various pressure loads inside the anterior chamber are shown. The appearance of a fringe pattern at 0 mmHg pressure load indicates that the pressure inside the cavity was different from atmospheric pressure. This pre-deflection of the diaphragm is caused by curing at high temperature during fabrication.

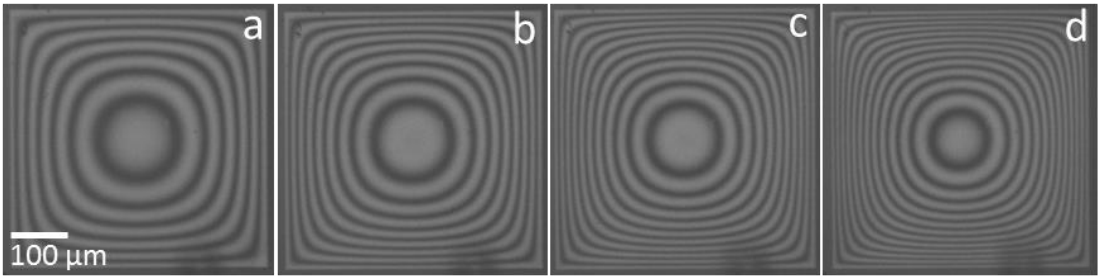

Figure 3.13: Images of interference patterns obtained from in-vitro experiment at pressure load of (a) 0 mmHg (b) 20 mmHg (c) 40 mmHg (d) 60 mmHg.

Using image processing algorithms (MATLAB and ImageJ), we analyzed the fringe patterns to determine the maximum deflection of the sensor diaphragm as a function of the applied pressure (Figure 3.14). A third order polynomial curve fit was performed on the experimental data to produce a calibration curve. The sensitivity of the sensor was determined to be 31 nm/mmHg. The resolution of the sensor, i.e., the minimum change of IOP that can be detected, depends on the minimum deflection of the diaphragm that can be captured. With the current image processing algorithm, a resolution of 0.2 mmHg was achieved.

Next, the sensor was subjected to three pressure load cycles from 0 mmHg to 60 mmHg with a step size of 5 mmHg. Using the calibration curve, we determined the measured pressure and compared it with the applied pressure. As shown in Figure 3.15, the measured pressure agrees well with the actual pressure with an average error of ±0.3 mmHg.

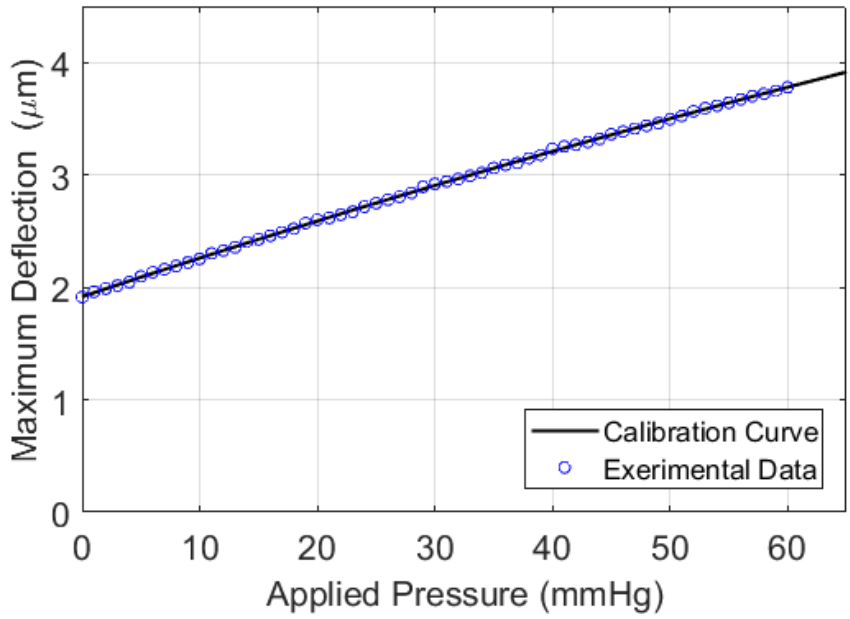

Figure 3.14: Maximum deflection of the sensor diaphragm as a function of applied pressure.

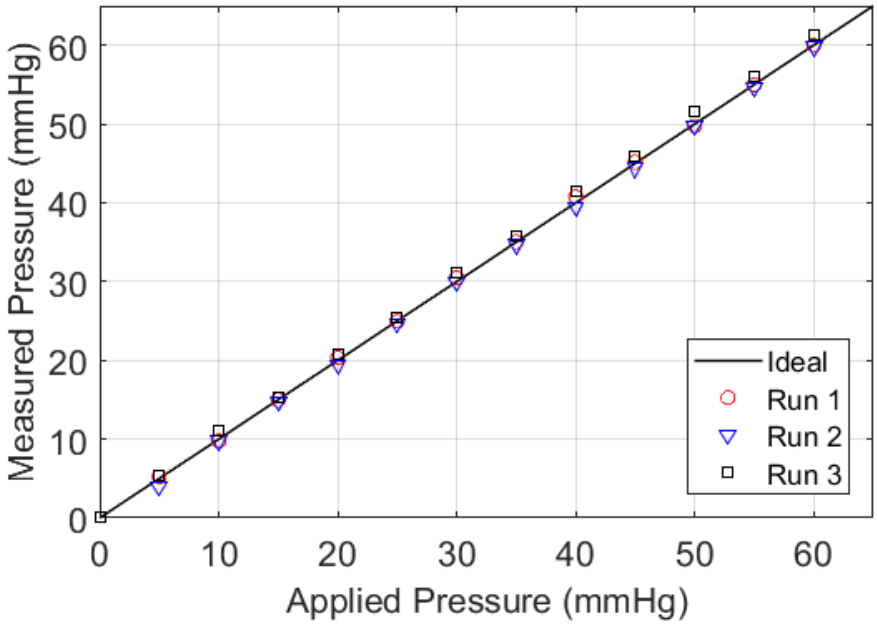

Figure 3.15: Measured pressure versus applied pressure for in-vitro (silicone cornea) pressure measurements using the optical pressure sensor.

3.2.3 Ex vivo Experiment using Rabbit Cornea

The mechanical properties of the silicone cornea and a real cornea are different. For this reason, we evaluated the response of the sensor using excised rabbit corneas to demonstrate the use of our sensor for measuring intraocular pressure. For ex-vivo testing, rabbit corneas with a 2 mm scleral rim were harvested from New Zealand white rabbits (Figure 3.12b). The corneas were immediately stored in phosphate buffer solution (PBS) at 4ºC to preserve the tissue. Similar to the procedure for the in-vitro investigation, the rabbit corneas were mounted on the artificial chamber for ex-vivo testing. The artificial anterior chamber was filled with water and pressurized, creating a 3-mm layer of fluid between the sensor and the cornea as shown in Figure 3.12c.

In this experiment, the chamber was first filled with phosphate buffer solution (PBS). Next, hydrostatic pressure was varied from 5 mmHg to 45 mmHg using a step size of 5 mmHg for three load cycles. A minimum pressure load of 5 mmHg was found to be necessary to keep the rabbit cornea inflated. Images of the interference pattern were captured at each pressure load and analyzed.

The calibration curve obtained from the in-vitro experiment with the silicone cornea was used to analyze the ex-vivo response of the sensor (Figure 3.16). We observed very good agreement between the actual pressure and the measured pressure with an average error of ± 0.6 mmHg.

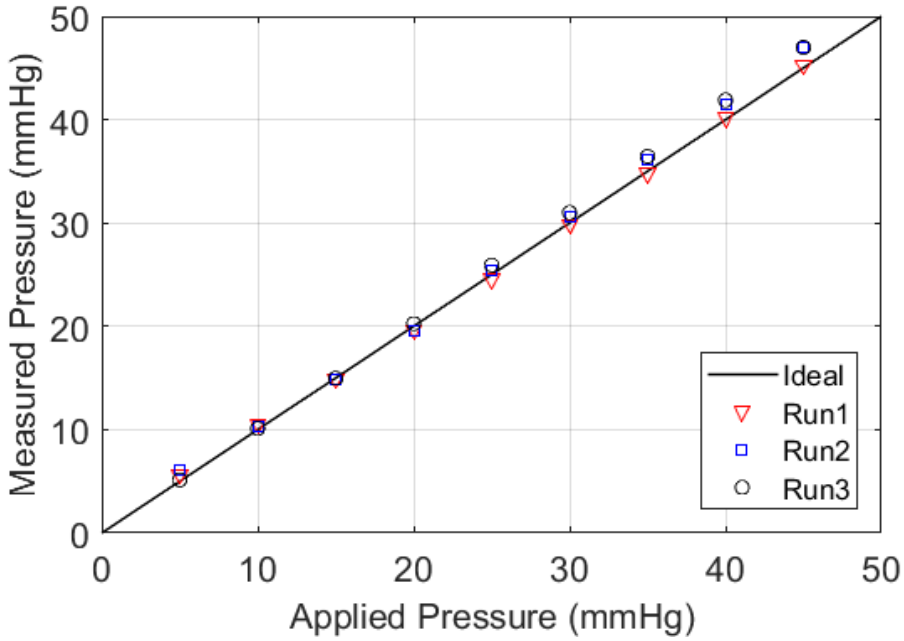

Figure 3.16: Measured pressure versus applied pressure for ex-vivo (rabbit cornea) pressure measurements using the optical pressure sensor.

3.2.4 Discussion

Our experimental pressure measurements for in-vitro and ex-vivo testing using our optical sensor have shown excellent results. The sensor measured intraocular pressure in the physiological range between 0 mmHg and 60 mmHg with an average error of ±0.3 mmHg for in-vitro experiments and ±0.6 mmHg for ex-vivo experiments. We believe that the difference in error between both tests can be attributed to damage of corneal endothelium cells during harvesting and storage. Over time, this may cause the cornea to become cloudy which reduces the visibility of the fringes and contributes to larger measurement errors, as observed in our ex-vivo experiments.

In real applications, preoperative calibration should be performed on each sensor prior to implantation to account for manufacturing tolerances. It is important to obtain a calibration curve associated with each sensor and to compensate fabrication variations such

as pre-deflection and residual stress of the diaphragm. Postoperative calibration can be tested by verifying the sensor readout with standard clinical IOP measurement techniques such as the Goldmann applanation technique.

We would like to point out that the square foot print of our sensor was chosen purely based on manufacturing cost considerations. A circular foot print would allow the reduction of the size of the sensor to about 1 mm or less in diameter without any additional changes in the manufacturing process. A circular footprint of 1 mm or less is well within the desired size of an implantable intraocular sensor.

Additional experiments performed will include in-vivo experiments with rabbit eye models to assess biocompatibility and bio-stability of our sensor. To conduct these studies, optimal sensor placement must be considered and integration of the sensor onto the intraocular lens must be performed. In addition, reducing the sensor footprint to sub-millimeter size using laser dicing without comprising sensor accuracy will be important for ease of implantation.

3.3 Summary

In this chapter, we discuss the fabrication process used to create the sensor. A novel two stage bonding method was proposed to optimize consistency and control equilibrium conditions during the sealing of substrate channels.

Once fabricated, the sensor was experimentally evaluated in vitro and ex vivo to assess its dynamic range, sensitivity, accuracy, and repeatability. The results demonstrated strong proof of concept results that are in line with the accuracy and characteristics required for an implantable intraocular pressure sensing device.

Chapter 3, in part is a reprint of the material as it appears in " Design of an Optical Pressure Measurement System for Intraocular Pressure Monitoring," Phan, Alex, Phuong Truong, Julian Trumpp, and Frank E. Talke, *IEEE Sensors Journal*, vol. 18, no. 1, 2018, pp. 61–68. The dissertation author was the primary investigator and author of this paper.

Chapter 4

Effects of Temperature, Incident Angle, and Substrate Coating

4.1 Introduction

In this chapter, we evaluate and isolate the effects of temperature, incident angle, and substrate coating thickness in order to determine the parameters that influence the optical readout of the sensor. Each external effect was isolated to find the range, calibration correction, or optimal parameter in which the sensor can provide a reliable reading. How these effects impact the efficacy of the sensor are also studied.

4.2 Effects of Temperature

As discussed in Chapter 3.6, the IOP sensor is fabricated and bonded at atmospheric pressure. During the sensor bonding process, the cavity of the sensor is sealed in the second stage of bonding, confining a certain amount of gas in the cavity. In an ideal bonding situation, where the epoxy seals the cavity very slowly, the pressure of the gas inside the cavity would be at atmospheric pressure. We can assume that the ideal gas law applies for this volume of gas:

$$PV = nRT \tag{4.1}$$

where P is the pressure of the gas, V is the volume of the cavity, n is the molar amount of the gas, R is the gas constant and T is the temperature of the sensor. Assuming the amount of gas inside the cavity is at equilibrium, the amount of gas, n, is a constant. The governing ideal gas law equation shows that if the temperature of the sensor increases, the pressure of the gas inside the cavity increases due to gas expansion.

If the reference pressure (P_{ref}) inside the cavity changes due to temperature, it can have a significant effect on the calibration curve if calibration is conducted at room temperature. Thus, it is necessary to quantify and isolate the effect of temperature on the response of the IOP sensor in order to obtain accurate readings once the sensor is implanted in a body with temperature above environmental temperature.

4.2.1 Experimental Design

To investigate the effects of temperature on the response of the sensor, an experimental set up consisting of a calibrated IOP sensor, Katena artificial anterior chamber and a water bath was used. The calibrated sensor was mounted in the Katena artificial anterior chamber and submerged into the water bath. A stir hot plate was used to heat up the water bath to a set temperature. A stirring rod was spun at low speed to ensure the water temperature in the bath was uniform. A schematic and photograph of the experimental setup are shown in Figure 4.1.

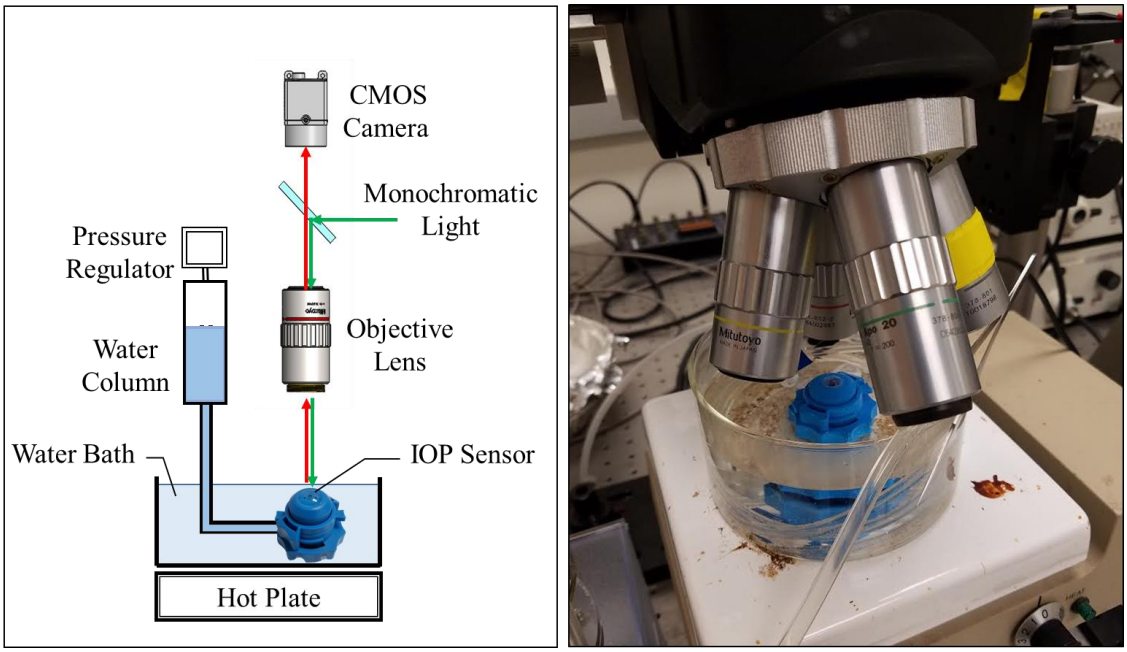

Figure 4.1: Schematic (left) and photograph of experimental setup (right).

In the first experiment, the temperature of the water bath was increased to 42°C and the hot plate was turned off allowing the system to cool down naturally. The hydrostatic pressure inside the anterior chamber was fixed at 20 mmHg using a pressure regulator. Fringe patterns of the sensor were captured at every 2°C drop as the temperature inside the water decreases to room temperature over the course of several hours.

In the second experiment, the temperature of the water bath was maintained at 37°C throughout the test. A hydrostatic pressure load of 0 – 40 mmHg with a step size of 5 mmHg was applied to the anterior chamber and the IOP sensor. Fringe patterns at each pressure load were captured for analysis.

4.2.2 Results

Results of the first experiment are shown in Figure 4.2. As the temperature of the sensor decreases, the pressure reading from the sensor increases for a fixed pressure load. The fitted curve shows a highly linear relationship between the two parameters. The effect of temperature on the response of the sensor can be characterized with the slope of this curve, m = 0.15µm/°C.

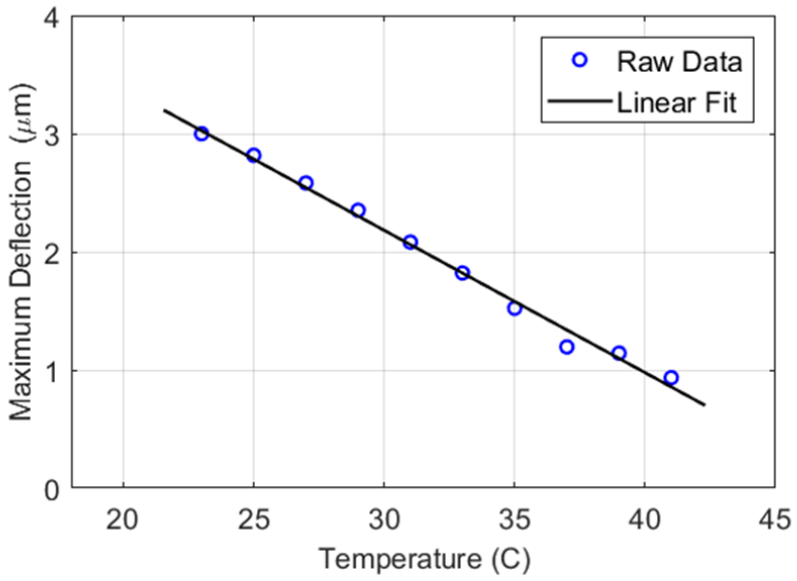

Figure 4.2: Effect of temperature on the maximum diaphragm deflection at a fixed pressure load.

For the second experiment, calibration curves from 0 – 40 mmHg of the same sensor at two different temperatures (24°C and 37 °C) were plotted for comparison. Similar to the sensor response from the previous experiment, the diaphragm of the sensor deflected into the cavity more at lower temperature for the same pressure load. It is important to note that the shapes of the two calibration curves are similar (Figure 4.3), indicating that the sensitivity of the sensor remains relatively constant in the temperature range of 24°C – 37°C.

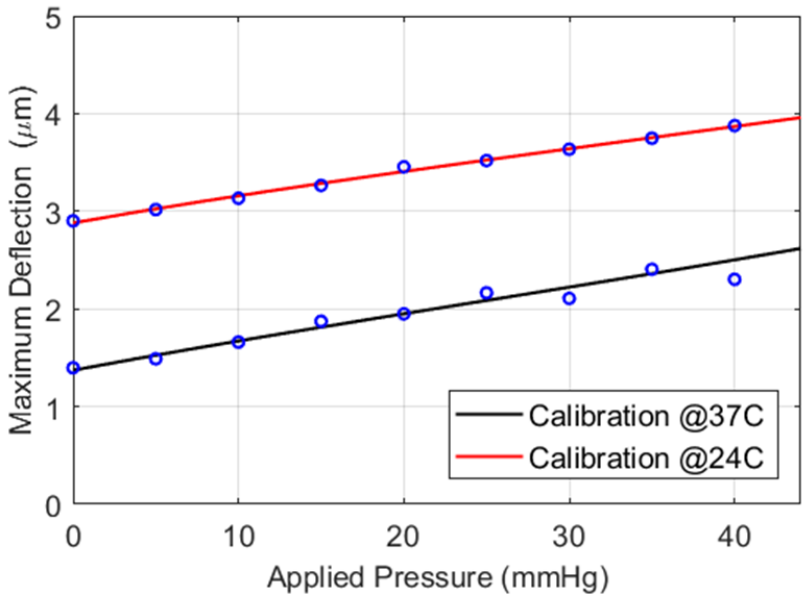

Figure 4.3: Calibration curves of the same sensor from 0 mmHg – 40mmHg at 24°C and 37°C.

4.2.3 Discussion

In this section, we investigated the effect of temperature on the response of the IOP sensor. The effect of temperature on the response of the sensor was determined to be about 0.15 µm/°C, or, equivalently, 5 mmHg/°C. The temperature in the human eye is assumed to remain relatively constant with minimal fluctuations due to homeostasis. However, in extreme conditions, the temperature of the eye may drop by 1°C – 2°C and would result in a higher IOP measurement than normal. One potential approach to eliminate the effect of temperature on the response of the IOP sensor is to utilize other bonding techniques that create a vacuum in the sensor cavity, e.g., anodic bonding. However, lower reference pressures inside the cavity of the sensor could lead to higher pre-deflection (more fringes) and make image processing more challenging.

4.3 Effects of Incident Angle

Normal incident angle is ideal for sensor readout and can easily be controlled during in-vitro testing. However, in real application, a variation in the incident angle may occur and could affect sensor readout. To determine the incident angle range in which a sensor readout can reliably be obtained, measurements were obtained at various incident angles.

4.3.1 Experimental Design

In this experiment, we varied the hydrostatic pressure from 0 mmHg to 60 mmHg using a step size of 5 mmHg, and changed the angle of incidence using a goniometer stage (Chuo Precision Industrial). A 200 nm SiN diaphragm was mounted in the pressure load cell, which was secured on top of the goniometer and an X-Y stage. Pictures of the experimental setup for various incident angles are shown in Figure 4.4.

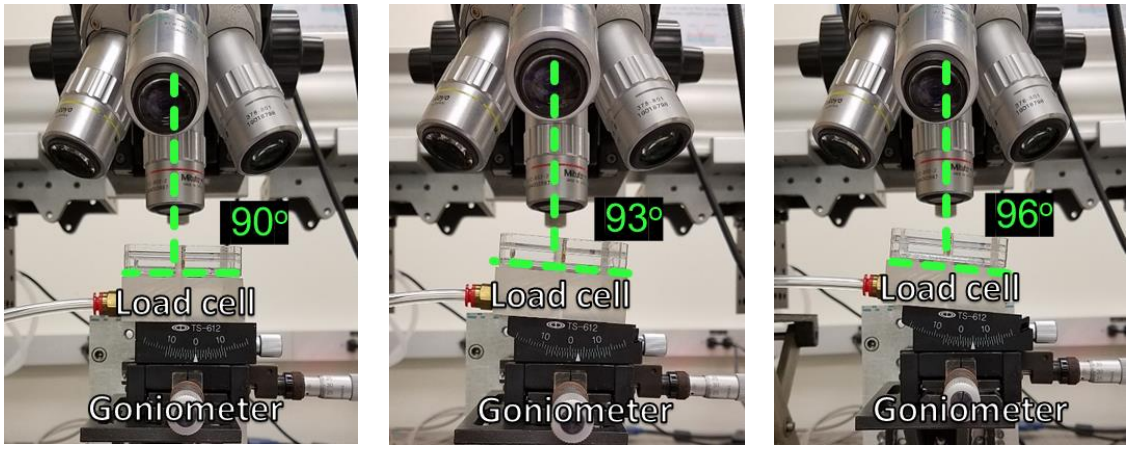

Figure 4.4: Experimental setup for the incident angel experiment using load cell and a goniometer. Incident angles (measure from the horizontal axis) of 90°, 93°, and 96° are shown here.

4.3.2 Results

Figure 4.5 shows the interference patterns for angles of incidence 0°, 3°, 6°, and 7°, respectively, at a constant pressure. Well-defined fringes can be seen for an angle of incidence up to 6°. It can be observed that the images obtained at increasingly larger angles of incidence appear darker due to the smaller amount of reflected light travelling back to the objective lens. However, we observed that the total number of fringes remains constant. The average errors of our pressure measurements for angles of incidence at 0°, 3° and 6° were calculated to be ±0.2, ±0.5 and ±1.4 mmHg, respectively. Images captured at incident angles larger than 6° were more difficult to analyze due to their low visibility (Figure 4.6). As shown in Figure 4.7, measurements taken at incident angles different from normal tend to underestimate the actual pressure slightly. These results indicate that while the incident angle may affect the quality of the optical read-out, the interference patterns are consistent up to ±6 degrees. Thus, it will be desirable to keep the variation of incident angles less than 6°.

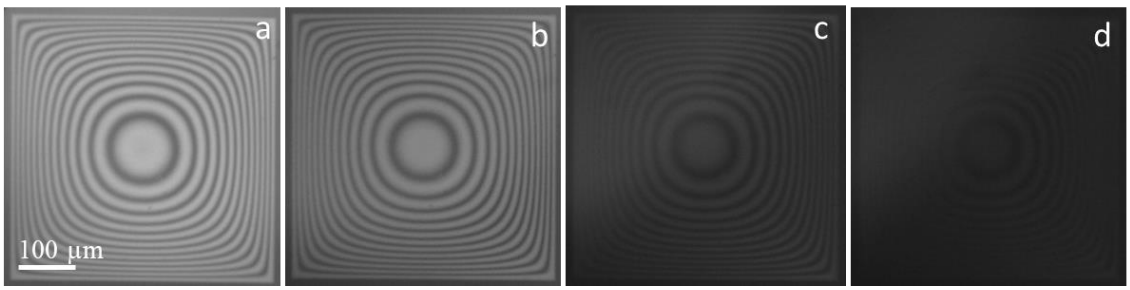

Figure 4.5: Sensor readout at various incident angles: (a) 0º incident angle (b) 3º incident angle (c) 6º incident angle (d) 7º incident angle.

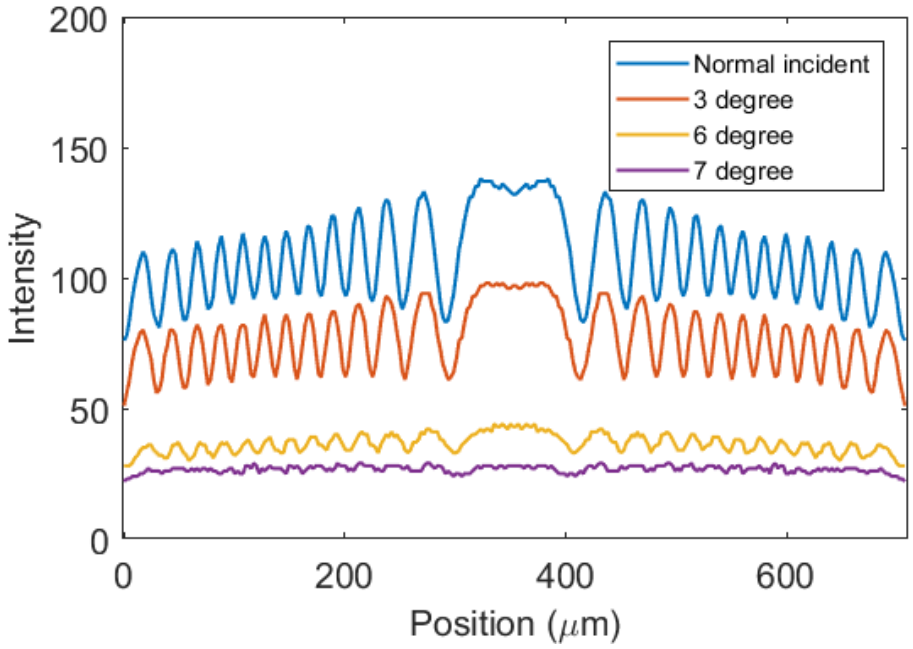

Figure 4.6: Intensities of fringe pattern along the diagonal line of the diaphragm at various incident angles: (a) 0º incident angle (b) 3º incident angle (c) 6º incident angle (d) 7º incident angle

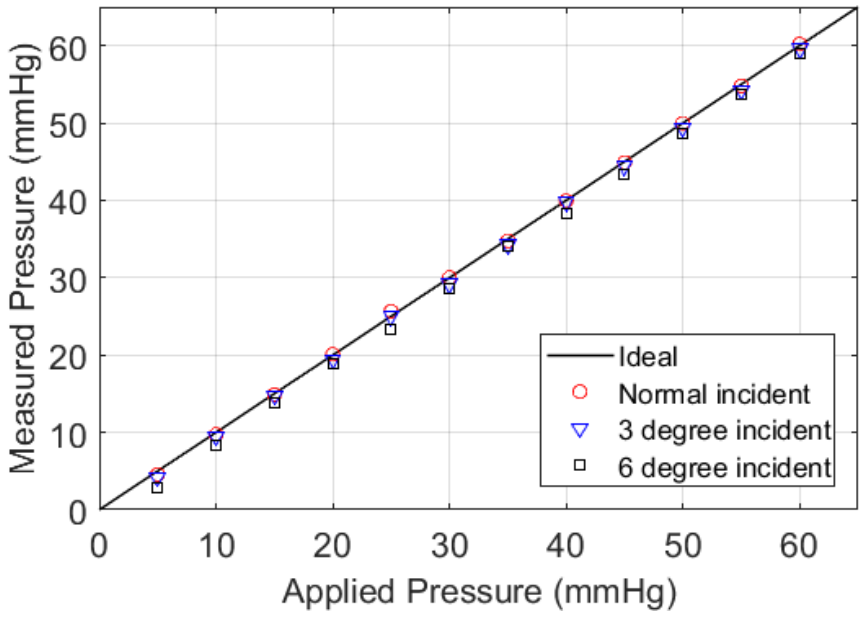

Figure 4.7: Effect of incident angle on pressure measurements.

4.3.3 Discussion

The incident angle used in the experiments was normal to the sensor surface as precise tooling and benchtop testing enabled ideal testing conditions. In actual application, the incident angle may vary and would have to be accounted for using a combination of a fixation point to limit eye movement, robust image processing algorithms to accurately distinguish interference fringes, and a slit lamp to position the optical unit. To test the limits of incident angle, a goniometer was utilized to test various angles. Based on experiments, it was found that reliable measurements can still be obtained within ±6 degrees in incident angle, while angles beyond this limit are too dark to analyze.

4.4 Effects of Substrate Coating Thickness

Optical visibility and contrast are important factors to consider for optimal achieving an optical readout signal. In this section, the effect of coating thicknesses is studied to optimize the optical sensitivity of the sensor.

4.4.1 Definition of Visibility

"Visibility" is a parameter that describes the quality of the interference fringes, i.e., the contrast between bright and dark fringes.

If I_1 and I_2 represent the intensities of the two reflected beams R_1 and R_2 (Figure 4.8), then the intensity of the resultant interference, I, can be expressed as:

$$I = I_1 + I_2 + 2\sqrt{I_1 I_2}\cos(\Delta\emptyset) \quad (4.2)$$

$$I_{max} = I_1 + I_2 + 2\sqrt{I_1 I_2} \quad (\text{when } \Delta\emptyset = 0) \quad (4.3)$$

$$I_{min} = I_1 + I_2 - 2\sqrt{I_1 I_2} \quad (\text{when } \Delta\emptyset = \pi) \quad (4.4)$$

Maximum constructive interference ($I = I_{max}$) occurs if $\Delta\phi = 2m\pi$ while maximum destructive interference occurs if $\Delta\phi = (2m-1)\pi$, where m is an integer. The visibility parameter of an interference pattern can be calculated from Equation 4.5 [122] as

$$Visibility = \frac{amplitude\ of\ the\ intensity}{average\ of\ intensity} = \frac{I_{max} - I_{min}}{I_{max} + I_{min}} \tag{4.5}$$

By substituting I_{max} and I_{min} from Equation (4.3) and (4.4) into (4.5) we obtain the following expression for visibility:

$$Visibility = \frac{2\sqrt{I_1 I_2}}{I_1 + I_2} \qquad (0 \le V \le 1) \tag{4.6}$$

4.4.2 Optimization of Visibility

To maximize the visibility of the interference fringes, the intensities I_1 and I_2 must be matched. This can be achieved by adding a thin silicon nitride coating on the surface of the glass substrate facing the sensor cavity as shown in Figure 4.8.

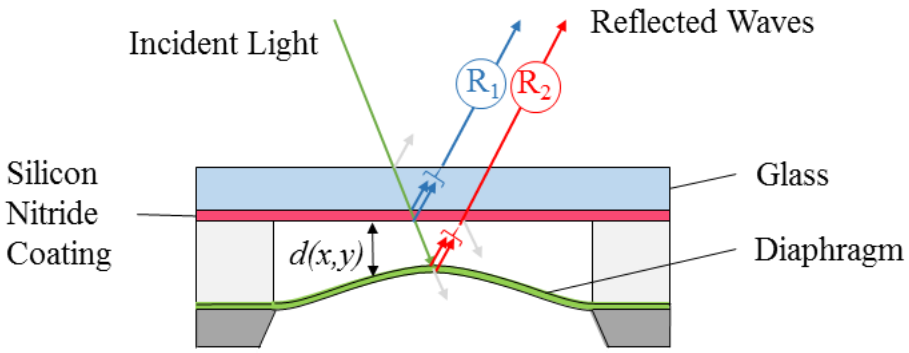

Figure 4.8: Schematic of interfering light with silicon nitride coating on the bottom surface of the glass substrate.

In Figure 4.9, the visibility of the interference pattern is plotted as a function of the thickness of the silicon nitride coating layer. We observe that the visibility varies between 62% and 100% as the coating thickness varies from 0 to 140 nm. For our experiment, the optimum coating thickness range which resulted in visibility of nearly 99% was determined to be within the range of 50 to 100 nm.

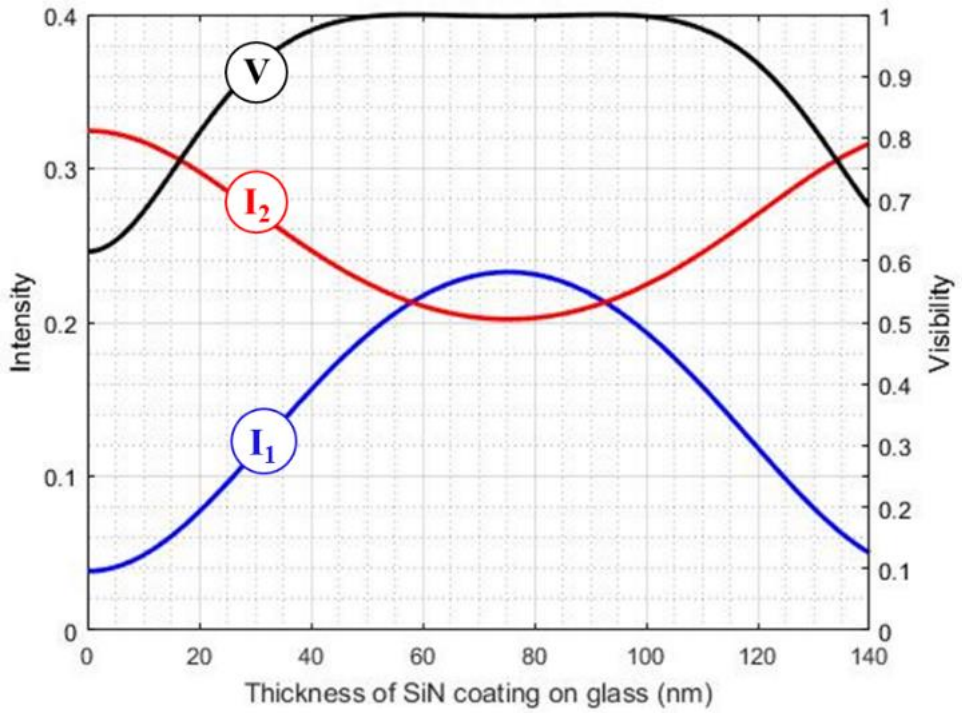

Figure 4.9: Visibility, V, and intensity of reflected light waves from the surface of the glass, I_1, and diaphragm, I_2, as a function of coating thickness. Highest visibility of the interference pattern was achieved for a silicon nitride coating thickness in the range from 50 to 100 nm.

4.4.3 Experimental Design and Results

Using the experimental setup described in reference [10], we investigated the effect of silicon nitride coating thickness on the visibility of the interference fringes. A 500µm borosilicate glass wafer (University Wafer) was diced into 0.5mm x 0.5mm square

substrates. A thin film of silicon nitride was deposited on the bottom surface of three glass substrates using PECVD (Oxford Plasma Lab 80). Deposition film thicknesses were measured to be 21 nm, 79 nm, and 139 nm with refractive indices of 2.1 (Filmetrics F20). One uncoated glass substrate was used as a control.

The four silicon nitride coated glass substrates were tested individually in a pressure chamber with a 10 um spacer and a 500 nm thick silicon nitride diaphragm (Norcada). A constant 20 mmHg pressure load was used for all conditions. Optimal thin film thickness was evaluated by comparing visibility of the various coating thicknesses of silicon nitride (Figure 4.10). The fringe pattern obtained from the 79 nm coating displayed highest visibility (highest contrast), followed by the 21 nm coating, the 139 nm coating and no coating. These qualitative results were in excellent agreement with the predicted numerical calculations presented in Figure 4.9.

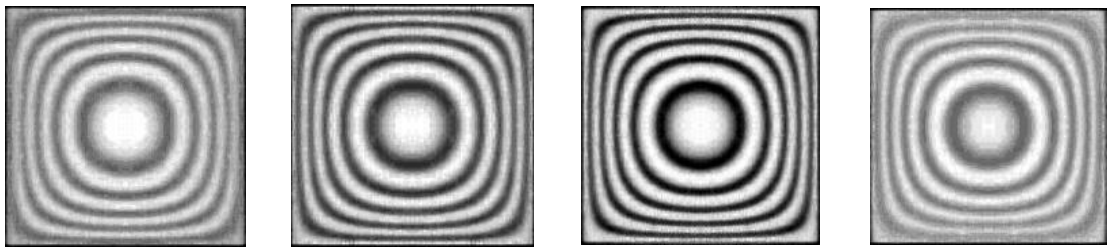

Figure 4.10: Images of interference pattern obtained from setup with glass substrate with varying silicon nitride coating thickness.

The intensity of the fringe pattern along the diagonal of each of the images is plotted in Figure 4.11. The corresponding visibilities were determined to be 0.37, 0.62, 0.92 and 0.38, respectively.

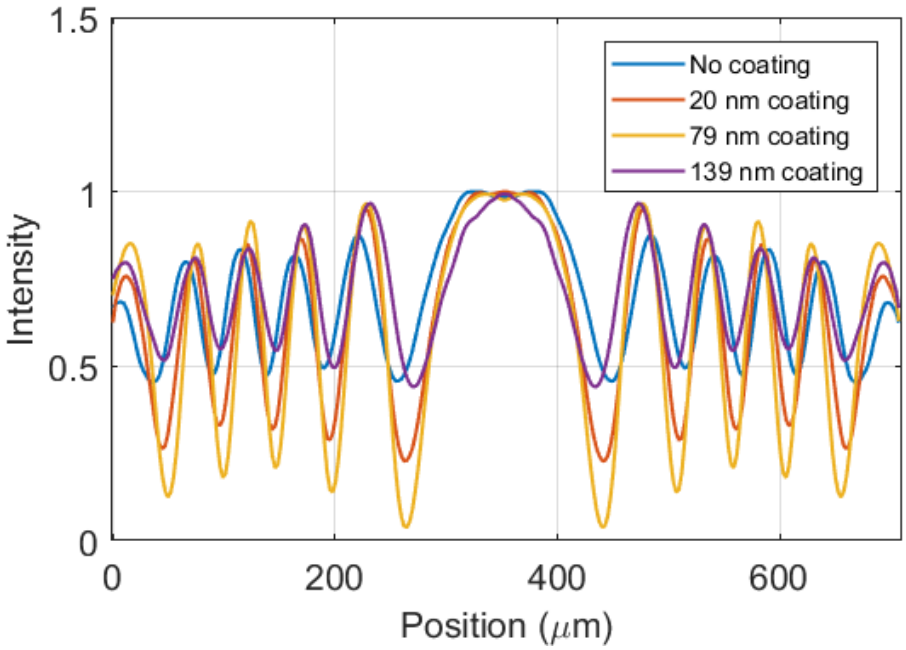

Figure 4.11: Intensities of the fringe patterns obtained from different coating thicknesses.

4.4.4 Discussion

In this section, we show that visibility of the interference patterns can be optimized by using a thin film coating on the surface of the glass substrate. By varying the coating thickness, we can control the transmission and reflection of the light traveling through the substrate. Visibility of the interference pattern can be further optimized during the image processing step. However, it is important to optimize the visibility optically to ensure that we can maximize the signal to noise ratio and obtain accurate pressure readings.

4.5 Summary

In this chapter, the effects of temperature, incident angle, and substrate coating were investigated.

First, temperature effects on the pressure inside the sensor cavity as a result of gas expansion were investigated. The offset from various temperatures was determined experimentally and accounted for in the final calculation of pressure. One method to reduce temperature effects is to create vacuum in the cavity. Fabrication techniques such as anodic bonding could generate a near vacuum cavity.

Second, the incident angle was investigated to determine the limiting range of the sensor for interference fringe measurements. The usable incident angle range was determined to be ±6 degrees. This finding is important in understanding the limitations of the optical approach. The incident angle limitation can be overcome in a real medical device by providing a fixation point on a screen to limit eye movement during measurements.

Finally, the visibility of an interferometric pressure sensor was optimized. A thin film coating of silicon nitride was used to match the intensities of the light reflected from the glass substrate and the diaphragm of the sensor. A coating thickness of 79 nm was shown to improve visibility by 150% in comparison to no coating.

Chapter 4, in part is a reprint of the material as it appears in "Optimization of an interferometric pressure sensor for intraocular pressure measurements," Phan, Alex, Phuong Truong, Julian Trumpp, and Frank E. Talke, *2018 ASME Information Storage and*

Processing Systems, Aug. 29 – 30, 2018, San Francisco, CA. The dissertation author was the primary investigator and author of this paper.

Chapter 5

Optical Handheld Reader

5.1 Introduction

In this chapter, we discuss the development of the optical read-out device of the intraocular measurement system. The IOP measurement system is intended to allow patients to measure their own eye pressure outside of the clinic setting. Therefore, the handheld reader should be portable and, more importantly, be able to obtain pressure measurements reliably at a reasonable readout distance. We have designed and built three different handheld readers of increasing complexity to demonstrate the feasibility of this concept.

5.2 Light Source

5.2.1 Safety Considerations

The IOP measurement system requires monochromatic light directed toward the eye of a patient. The power intensity of this light source must be lower than the safety level set by the American National Standards Institute (ANSI). Power of the light source and exposure time are the two most important parameters for safety reasons. According to ANSI, a laser with power under 4 μW is classified as class I and considered to be safe without any exposure time restrictions [151]. All light sources used in this research are kept within this safety limit.

5.2.2 Light Source Selection

The visibility of the interference fringes is essential to the accuracy of the IOP measurement system as discussed in the previous chapter. Therefore, it is important to select a light source that can produce high fringe visibility. Four approaches to generate monochromatic light were considered as shown in Table 5.1: Approaches to generate monochromatic light..

Table 5.1: Approaches to generate monochromatic light.

Light source	**Halogen with filter**	**Laser**	**LED**	**LED with filter**
				
Wavelength	632.8 nm	635 nm	635 nm	633 nm
FWHM	1 nm	< 1 nm	10 nm	5 nm
Power	150 W	1.2 mW	4 mW	4 mW

In the bench top set up, the monochromatic light source was generated using a combination of broadband white light and a laser line filter. The 150W halogen bulb is housed in a control unit with active cooling system to regulate the dissipated heat. When coupled with the laser line filter (Thorlabs FL628.1-1), this light source generates 2 µW at the target. While this configuration satisfies the safety requirement and works well for the bench top setup, it is not feasible for a portable handheld reader device due to its large form factor.

In the second approach, a laser source was used to generate the monochromatic light. A 1.2 mW red laser light source (Thorlabs CPS635R) was tested. A neutral density filter (Thorlabs NE20A) was used to reduce the power intensity of the laser to a safe level. This light source generated interference fringes with high visibility. However, because of the extremely high monochromaticity, the light source also generated many undesired diffraction patterns which interfere with the optical read out of the measurement system. An example of interference pattern generated by this light source is shown in Figure 5.1.

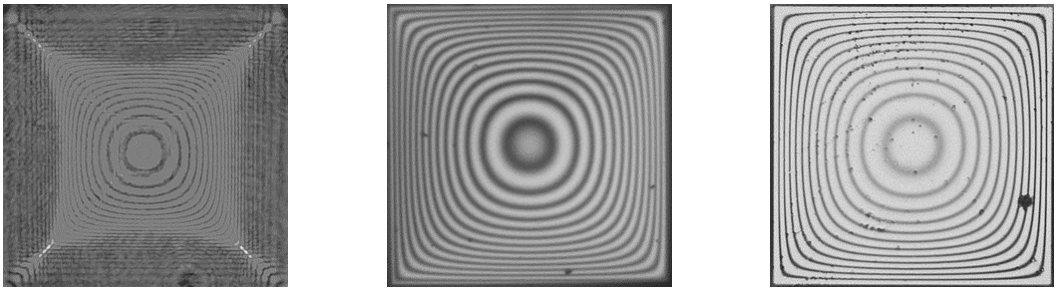

Figure 5.1: Interference patterns generated using different light sources: laser light source (left), halogen light with 1 nm laser line filter (middle), 635 nm LED with 5 nm laser line filter (right).

In the next approach, an LED with a narrow bandwidth was used as the monochromatic light source. LEDs generate high intensity light at very low power consumption which is a desirable feature for a portable device. A 4-mW red LED (Thorlabs LED631E) with a center wavelength of 635 nm and a full width at half maximum (FWHM) of 10 nm was tested. This light source was found to generate interference fringes. However, the visibility of the fringes was very low. As the bandwidth of the light source increases, the coherence of the light source decreases. This resulted in very low contrast between the bright and dark fringes.

Based on the testing results of the previous two approaches, it can be concluded that the bandwidth of the light source should be in the range of 1-10 nm. One potential

solution was to use the 635 nm LED together with the 632.8 nm laser line filter. However, due to the mismatch in the center wavelengths of these two items, the intensity of the output was too low for adequate measurement. To overcome this problem, a 5 nm bandpass filter (Thorlabs FLH633-5) with a center wavelength of 633 nm was used together with the 635 nm LED to generate the monochromatic light. This approach generates fringes with high visibility without any undesired diffraction patterns. Hence, this combination of a single-color LED and a bandpass filter was chosen for the development of the handheld readers.

5.3 First Generation Handheld Reader

The first generation of the handheld reader was designed and built to be a table top experimental setup. The main consideration for this reader was portability for in vivo IOP measurement on rabbits. The visibility of the fringes captured using this handheld reader should be comparable to the value obtained using the lab set up.

5.3.1 Configuration and Assembly

A schematic of the handheld reader is shown in Figure 5.2.

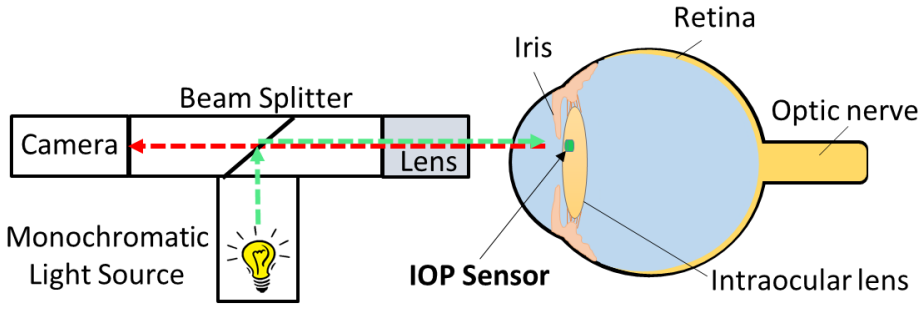

Figure 5.2: Portable handheld reader for optical pressure measurement system.

The optical path of the handheld reader follows the same configuration as that of the table top setup using a microscope. As monochromatic light travels through a beam splitter and an objective lens, it is directed to the implanted sensor in the anterior chamber of the eye (shown in green). Interference waves generated at the cavity of the sensor travel though the objective lens, the beam splitter and arrive at the camera (shown in red).

A portable handheld reader was built based on the schematic shown above. The unit consists of an objective lens (Mitutoyo Apo 5x), a beam splitter (Thorlabs CCM1-BS013), a 635 nm LED light source (Thorlabs LED631E), a 5 nm bandpass filter (Thorlabs FLH633-5) and a CMOS camera (Thorlabs DCC3240M). A photograph of the handheld reader is shown in Figure 5.3.



Figure 5.3: Portable handheld reader for optical pressure measurement system.

5.3.2 Experimental Testing

An XYZ stage was custom build to hold the handheld reader and position it above the artificial anterior chamber as shown in Figure 5.4. The stage can be translated in three directions. This allow accurate use and ease of alignment during testing of the handheld reader.



Figure 5.4: Experimental set up to evaluate the handheld reader.

Figure 5.5 shows a comparison of images from the same sensor taken using the bench top set up and the handheld reader. The fringe patterns observed were almost identical between the two methods, indicating that a handheld reader can be used to measure IOP in a clinical or patient point-of-care setting with accurate reading. However, while the initial handheld reader design can obtain comparable images to benchtop (when clamped in the apparatus in Figure 5.4), the device was difficult to use when imaging by hand. The preliminary tests using the reader as a handheld device resulted in blurry images, inconsistent focus, tracking as well as incident angle problems. This is due to the limited field of view and the lack of auto-stabilization and auto-focus features in the reader.

Measurements taken using this reader were obtained from video clips in which the region of interest in the video were isolated, cropped, rotated, and post processed.

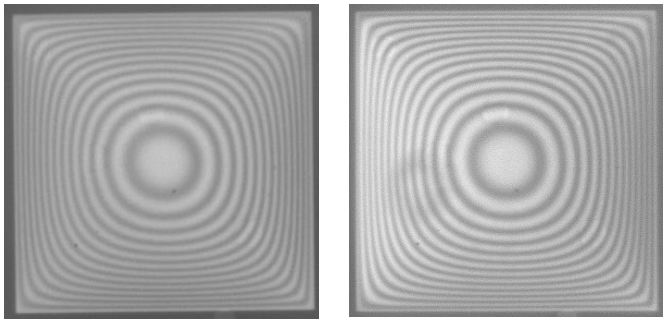

Figure 5.5: Fringe pattern of the same sensor at 20 mmHg pressure captured using the bench top lab setup (left) and the handheld reader (right).

In-vitro pressure measurements obtained using the handheld reader are shown in Figure 16. The results show very good agreement between measured pressure and actual pressure, with an average error of less than ±0.2 mmHg.

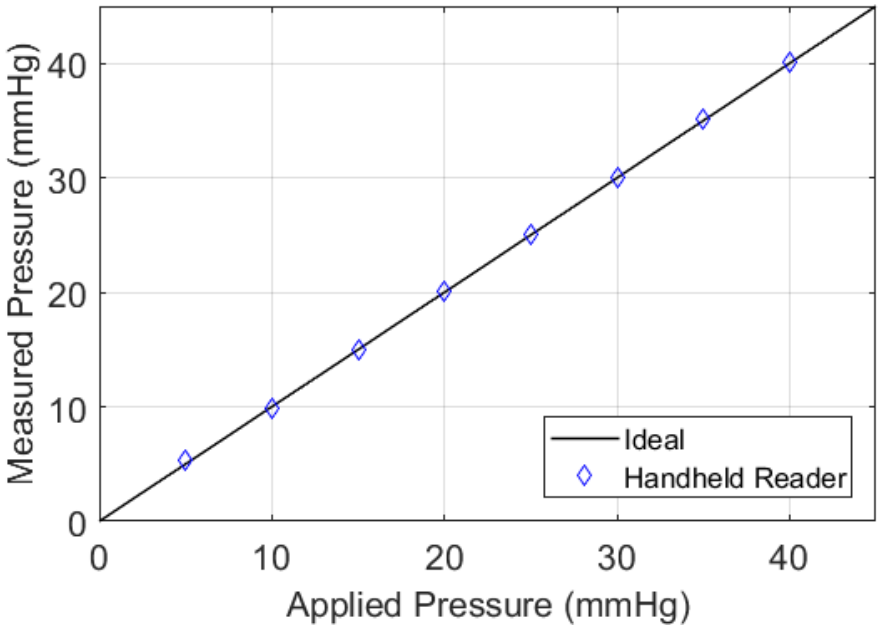

Figure 5.6: In-vitro pressure measurement using the handheld reader with a CMOS camera and a smartphone camera.

5.3.3 Discussion

The first-generation handheld reader is a portable device that could capture accurate IOP measurements. The images captured in a static setting using the reader were comparable to the bench top setup. However, the reader is susceptible to noise due to movement of the user and/or the subject during measurement. The problem can be overcome by taking a video of the fringe patterns as opposed to a picture. Frames from the video can be analyzed for measurement. This makes the reader difficult to use. A more practical reader is desired and will be presented in the next section.

5.4 DSLR Handheld Reader

The first-generation handheld reader was used to demonstrate proof of concept of a portable IOP measurement device. However, the lack of image stabilization and short depth of field (4um) presented challenges in taking pressure measurements in a practical setting. These shortcomings were addressed in the second iteration of the handheld reader using a digital single lens reflex (DSLR) camera.

5.4.1 Configuration and Construction

The DSLR handheld reader utilizes the same working principle as the previous reader. The schematic of the DSLR reader is shown in Figure 5.7. We replaced the CMOS camera with a DSLR camera with image stabilization (IS) technology. Canon macro lens (Canon EF 100mm f/2.8 IS) incorporates hybrid image stabilization technology that compensates for both translational and rotational motion during picture taking. This lens

stabilization technology reduces noise for a close-up shot during IOP measurement, allowing for a more accurate reading.

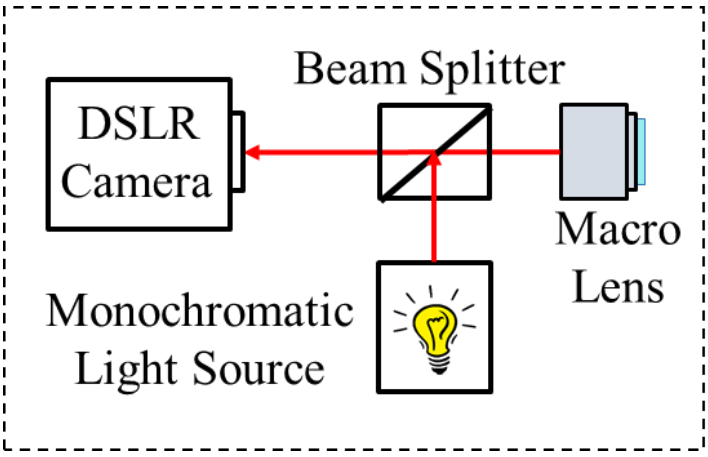

Figure 5.7: Schematic of the DSLR handheld reader.

The handheld reader consists of a DSLR camera (Canon 77D), a macro lens (Canon EF 100mm), a beam splitter (Thorlabs CCM1-BS013), a 635 nm LED light source (Thorlabs LED631E), a 5 nm bandpass filter (Thorlabs FLH633-5), an iris (Thorlabs SM1D12D), a condenser lens (Thorlabs ACL25416U), and a diffuser (Thorlabs DG10-1500-A). A custom adaptor was designed and machined to connect the beam splitter to the body of the camera and the camera lens (Figure 5.8). Electrical wires were used to connect the eight electrical connectors from the right side of the adaptor (to the camera) and the left side of the adaptor (to the lens). These electrical connectors are necessary to power the lens and control lens stabilization. A photograph of the complete DSLR reader is shown in Figure 5.9.



Figure 5.8: Adaptor for DSLR optical handheld reader



Figure 5.9: Photograph of the DSLR handheld reader.

5.4.2 Experimental Testing

An in vitro experiment was conducted to assess the quality of the fringe patterns captured using the DSLR handheld reader. A calibrated sensor was placed in the Katena artificial anterior chamber and subjected to a pressure load of 0 – 60 mmHg at a step size of 5 mm. Fringe patterns at each of the pressure steps were taken using the DSLR reader and analyzed. The results of the experiment (Figure 5.10) showed that the DSLR reader accurately captured the pressure profile with average error of less than 0.5 mmHg. Images of in vitro and ex vivo fringe patterns captured using the reader are shown in Figure 5.11.

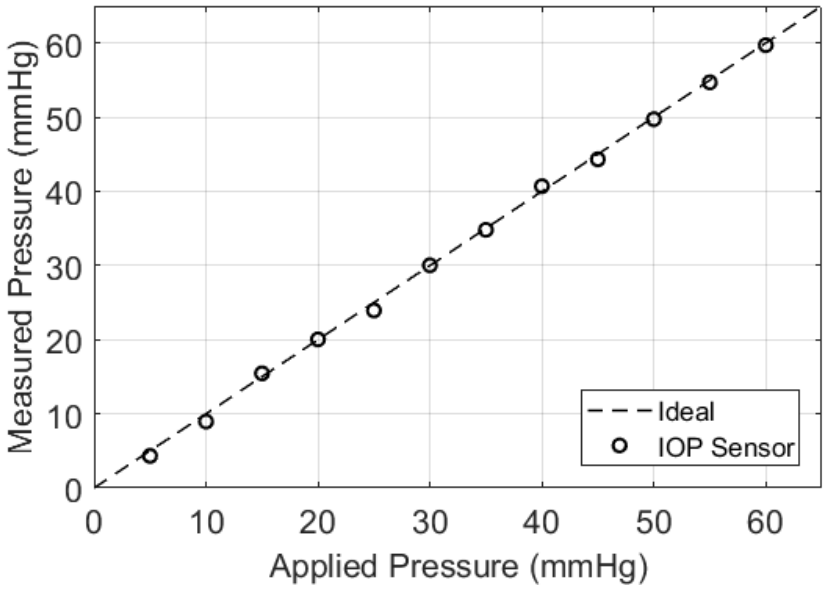

Figure 5.10: Measured pressure versus applied pressure for in vitro pressure measurements using the DSLR handheld reader.

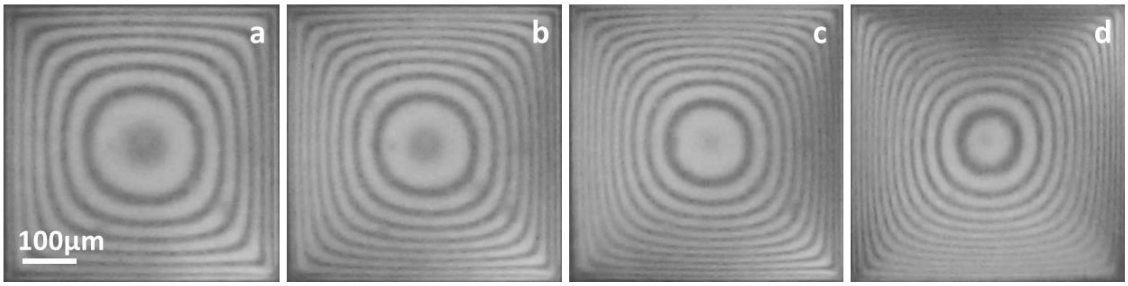

Figure 5.11: Images of interference patterns obtained from in-vitro experiment using the DSLR reader at pressure load of (a) 0 mmHg (b) 20 mmHg (c) 40 mmHg (d) 60 mmHg.

5.4.3 Discussion

With a large optical sensor, the Canon 77 DSLR camera allows IOP measurements with sharp images. Image stabilization technology of the macro lens helps reduce motion artifacts and noise in the measurement. Though the DSLR reader is large, it offers a reliable and portable option to obtain IOP measurements in a practical setting.

5.5 Mobile Device Attachment and Android App

To further demonstrate the feasibility of the IOP measurement system as a patient point-of-care technology, we incorporated the handheld reader into a smartphone device. As smartphone technology continues to advance with faster processors and more powerful camera systems with large sensors, autofocus features, and high resolution, the use of smartphone-based readers is now possible. There have been many applications of smartphones in the field of ophthalmology, e.g., fundus scope, slit lamp, etc, [152]. Our goal is to integrate the interferometry optics into a smartphone to create a compact handheld reader for the IOP measurement system.

5.5.1 Configuration and Construction

The design of the smartphone reader was divided into two components: the light source component and the lens system component.

The light source component is the same as the DSLR reader: a beam splitter (Thorlabs CCM1-BS013), a 635 nm LED light source (Thorlabs LED631E), a 5 nm bandpass filter (Thorlabs FLH633-5), an iris (Thorlabs SM1D12D), a condenser lens (Thorlabs ACL25416U), and a diffuser (Thorlabs DG10-1500-A).

The main challenge of building the smartphone reader is designing a lens system to integrate the interferometry optics with the phone camera. Since the optical sensor of the smartphone camera is significantly smaller than that of the DSLR camera, captured images of the sensor must be sufficiently large for post processing. Based on our previous experience with the first-generation reader, the field of view should be 0.25 – 1 cm^2. This would allow us to locate the sensor quickly as well as keeping it in the field of view during measurement (accounting for any movements by the user or the subject).

Although a microscope objective lens produces images with very little distortion, the main drawback of this approach is the long focal length. Our goal is to develop a compact handheld reader. Therefore, we decided to design a custom lens configuration that allows us to capture the sensor image at 0.5x – 1x magnification, with distortion of less than 5% and a total track length of less than 15 cm.

To achieve the optical design requirements, a 3-lens combination system consisting of an achromatic doublet lens (Thorlabs AC127-019-A), a bi-convex lens (Thorlabs LB 1901-A) and an achromatic triplet lens (Thorlabs TRH254-040-A) was used. A schematic

of the lens setup is shown in Figure 5.12. Reflected light from the sensor is directed through the optical system and collimated when it arrives at the phone camera.

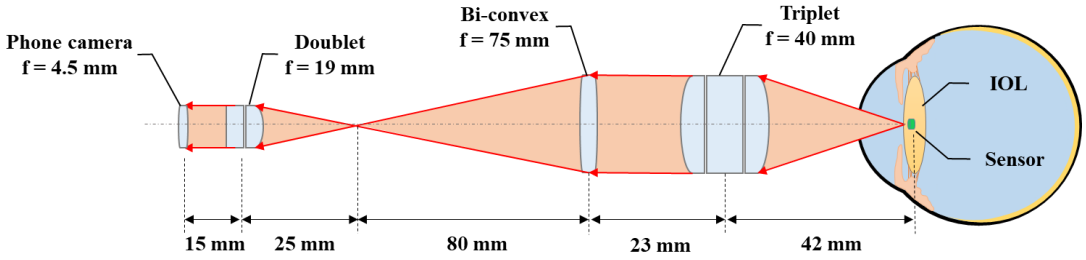

Figure 5.12: Schematic of custom lens system of the smartphone handheld reader. Interference fringes from the sensor (right) are directed to the phone camera (left) through the lens system.

Commercially available software "Zemax" was used to simulate the output of the lens system to evaluate the design of the setup. A ray diagram of the simulation is shown in Figure 5.13. Maximum distortion of a 1.4 x 1.4 mm field was simulated to be 2.43% (Figure 5.14) and maximum distortion of a 5 x 5 mm field was simulated to be less than 10%. This amount of distortion is acceptable given that the size of the interference pattern is 0.5 x 0.5 mm and the sensor is aligned to be in the center of the field of view.

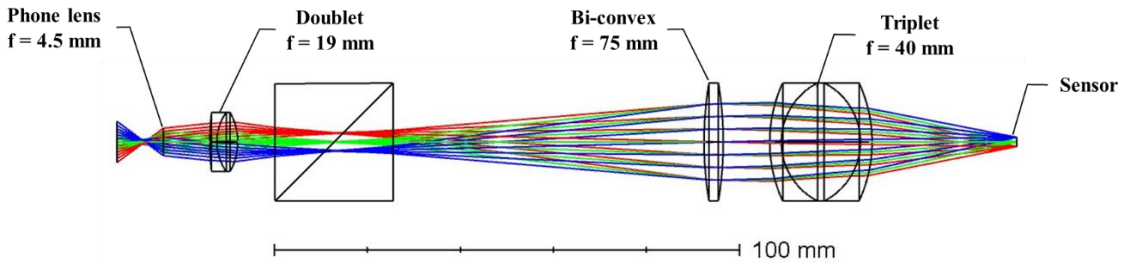

Figure 5.13: Ray trace diagram of the optical system simulated using Zemax. The sensor is placed on the right side of the diagram and the phone is placed on the left side of the diagram.

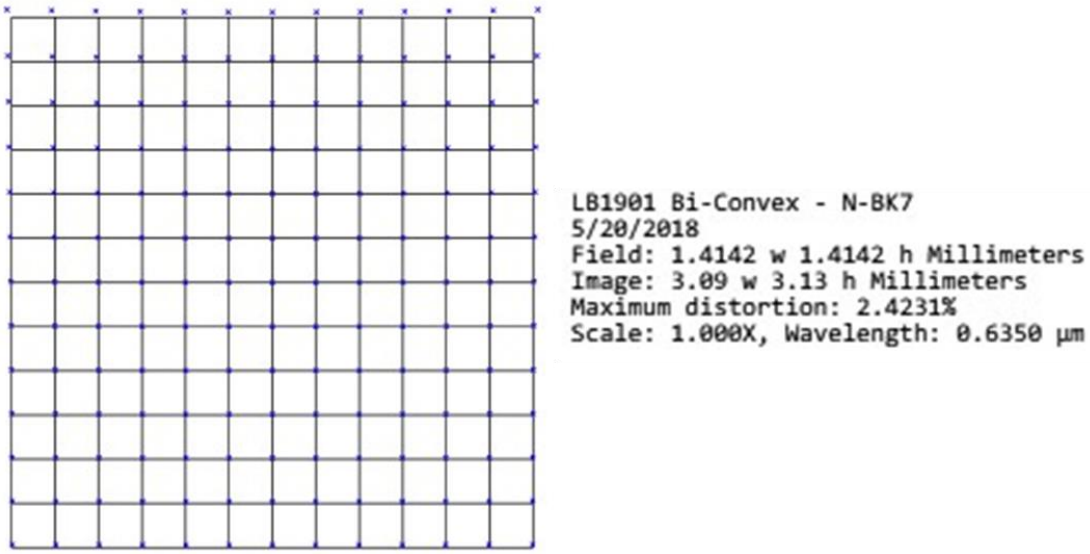

Figure 5.14: Distortion field plot of the optical system simulated using Zemax. The maximum distortion of 2.42% was simulated for a field of 1.4 x 1.4 mm.

After the lens system was built and tested based on the design above, it was integrated with the light source components to complete the smartphone handheld reader. A schematic and a photograph of the smartphone reader are shown in Figure 5.15. All optical components were connected together using standard optical tubes and cages from Thorlabs. A custom phone case and connector were designed, and 3D printed to connect the smartphone (Google Pixel 2) to the reader.

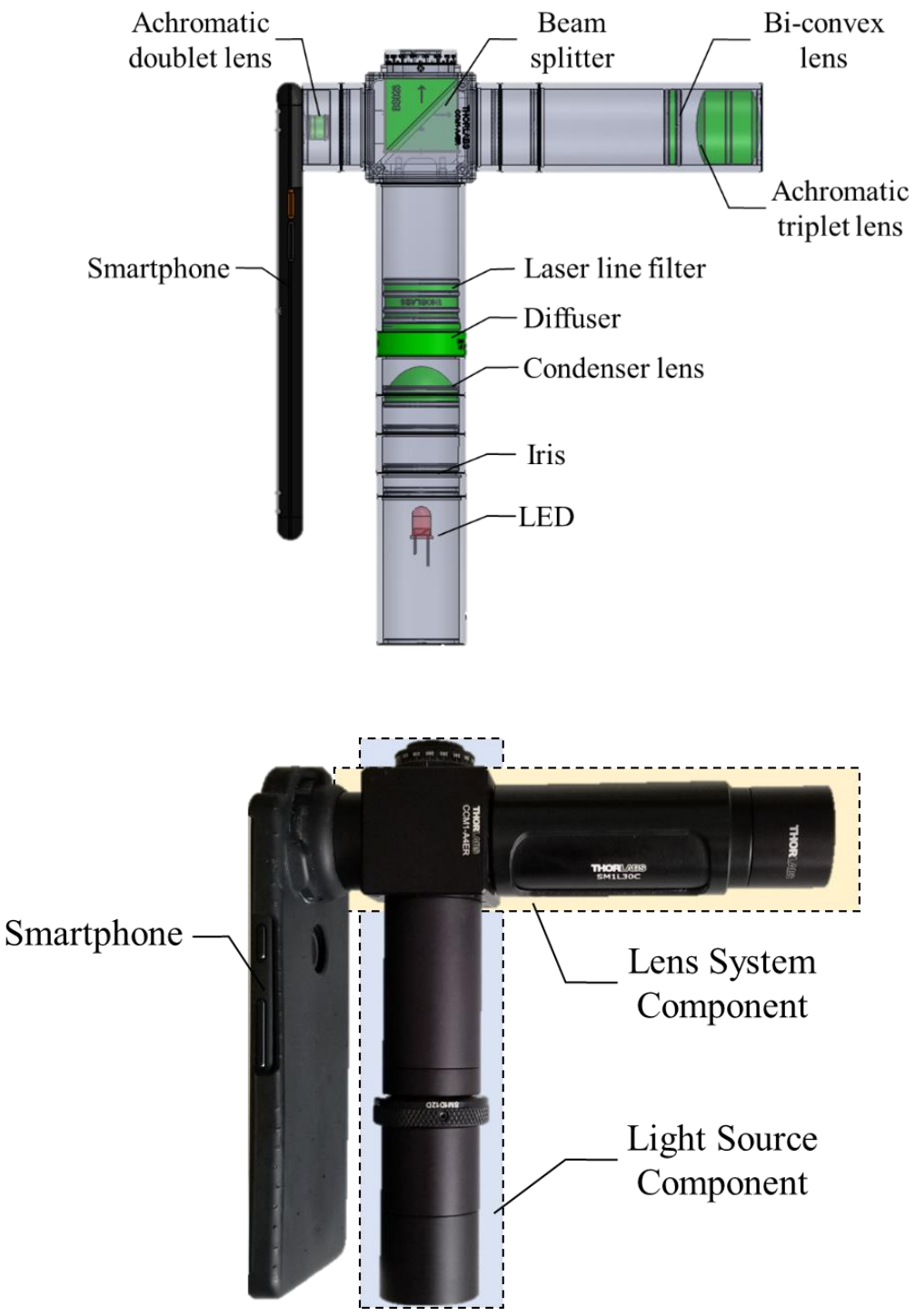

Figure 5.15: Schematic (top) and photograph (bottom) of the smartphone handheld reader

5.5.2 Smartphone Application on Android Platform

An Android application (app) was developed to allow the user to use the smartphone handheld reader to obtain IOP measurement. The main functions of the app include: utilizing the smartphone camera to capture an image of interference fringes from the sensor, performing image processing on the captured image to determine the pressure value, and saving the measured pressure value in a data log for report.

The process flow diagram of the IOP app is shown in Figure 5.16. Once the app is launched, the user has three options from the main user interface (UI) screen: (1) take new IOP measurement, (2) process previous data and (3) access the IOP history. Once an image of the interference pattern is captured using the camera or loaded from storage, the application performs image processing and analyzes the pattern to calculate the IOP pressure. The user will then have an option to save the measurement or return to the main UI screen. Screen shots of the main functions of the app are shown in Figure 5.17.

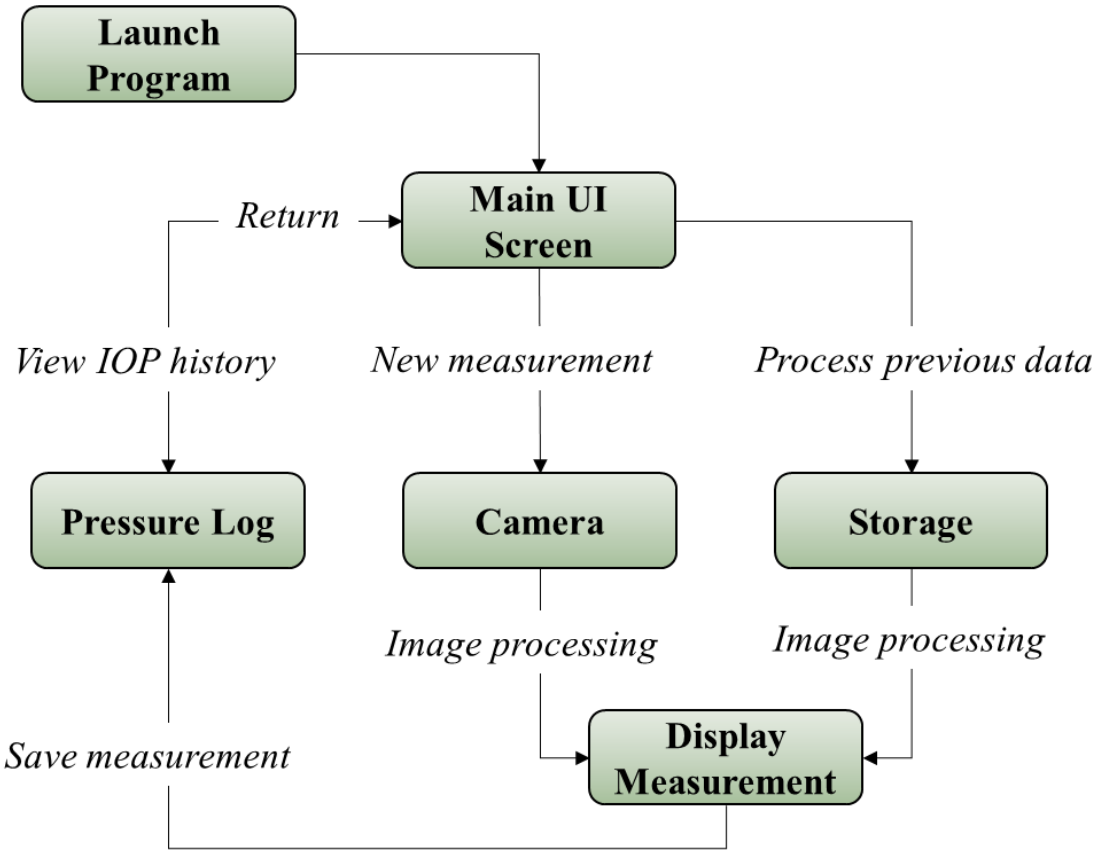

Figure 5.16: Process flow diagram of the IOP smartphone app

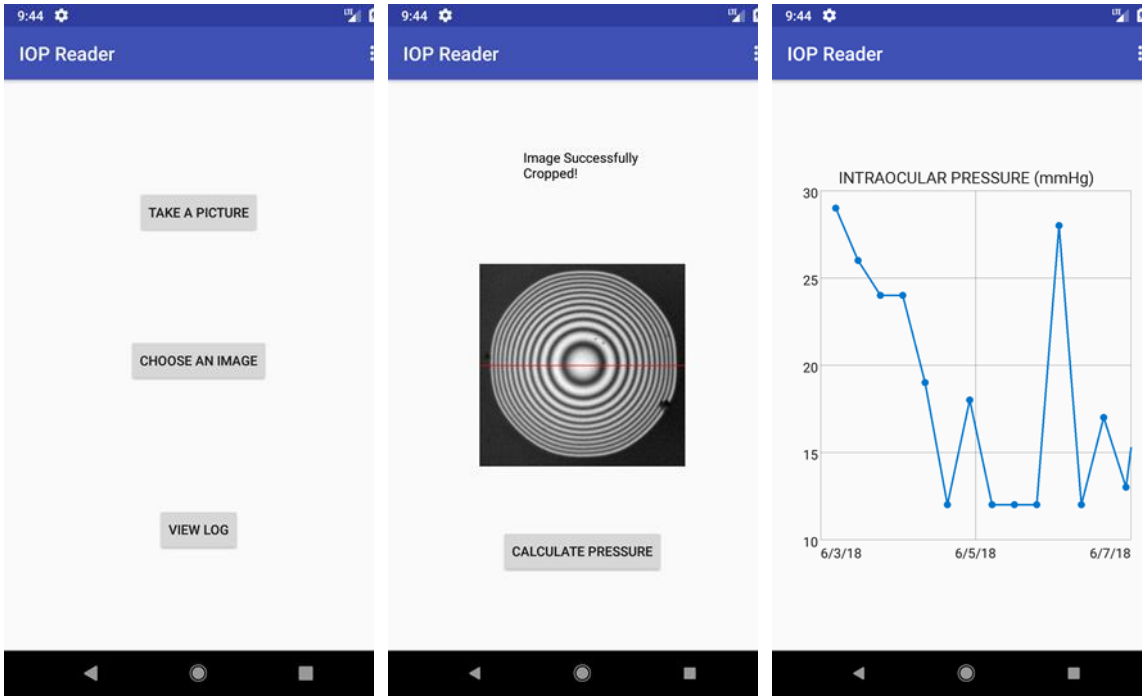

Figure 5.17: Screenshots of the main functions of the IOP app: (L) Home screen with options to take new measurement or load the measurement log, (C) Image processing to determine the pressure value, and (R) IOP measurement log.

5.5.3 Experimental Testing

The handheld reader was first used to a static in vitro experiment to evaluate the optical performance of the device. A calibrated sensor was mounted in a Katena artificial anterior chamber and subjected to a pressure load between 0-60 mmHg with a step size of 5 mmHg. The reader was mounted 4 cm directly above the chamber as shown in Figure 5.18.

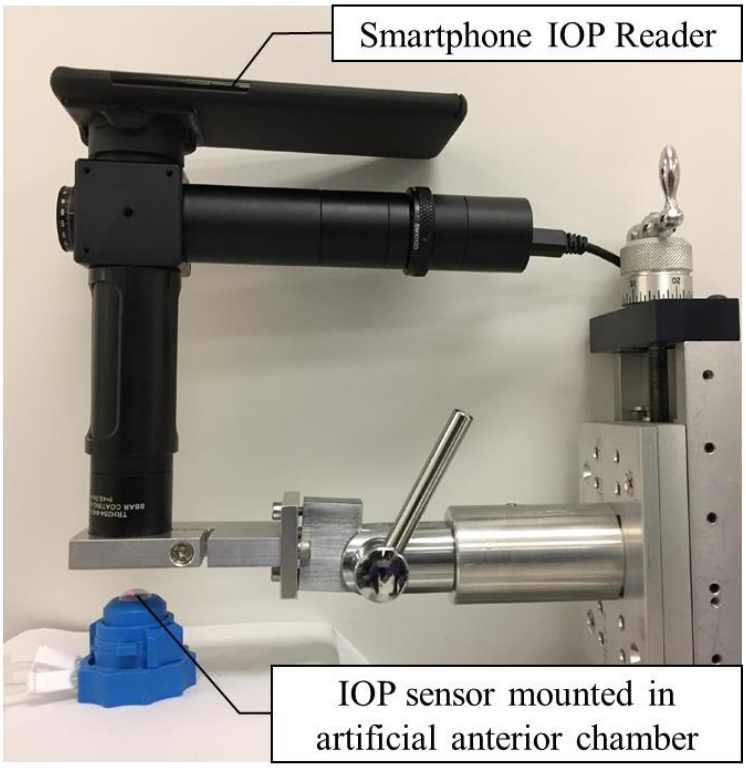

Figure 5.18: Experimental setup to evaluate the smartphone reader. The IOP sensor is mounted in a pressure control artificial anterior chamber. The smartphone reader is position directly above the chamber to capture the response of the sensor.

Pictures of the interference patterns were captured and analyzed. A typical image obtained with the reader is shown in Figure 5.19. The field of view was about 4 x 4 mm and images of the sensor were captured with good fringe visibility.

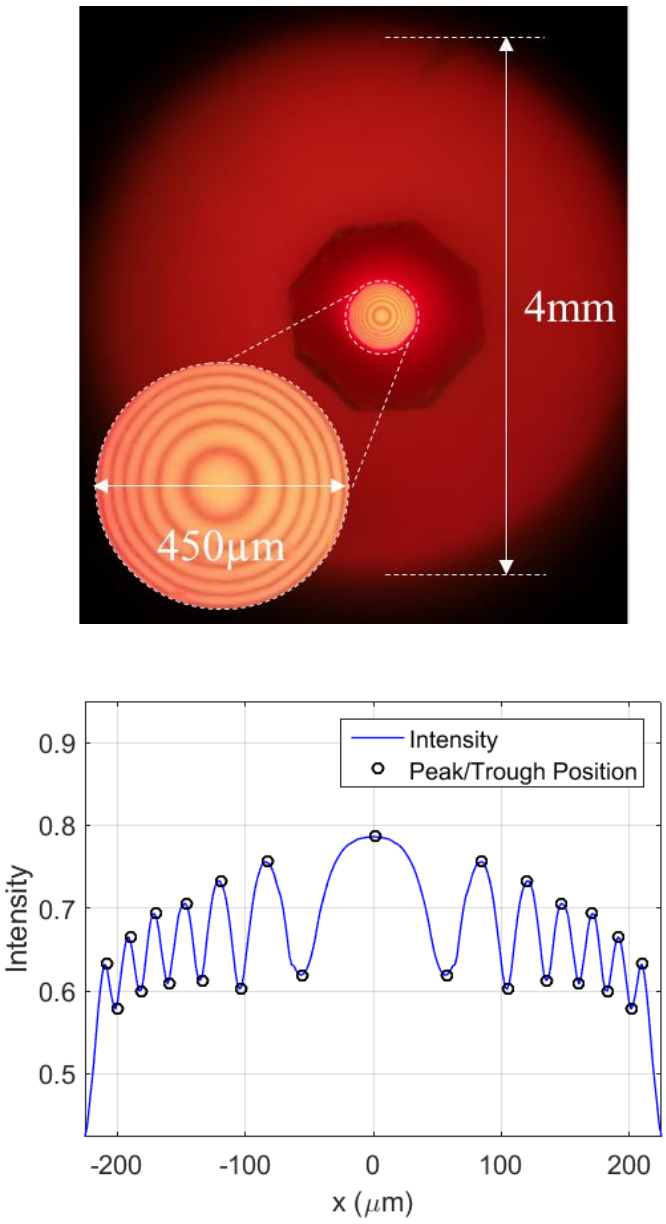

Figure 5.19: Typical image of the sensor captured using the smartphone reader in a static setup (top). Visibility plot of the corresponding interference pattern (bottom).

The measured pressure values were compared with the applied pressure as shown in Figure 5.20. The results indicated that the smartphone reader can be used to accurately measure IOP pressure in a static set up.

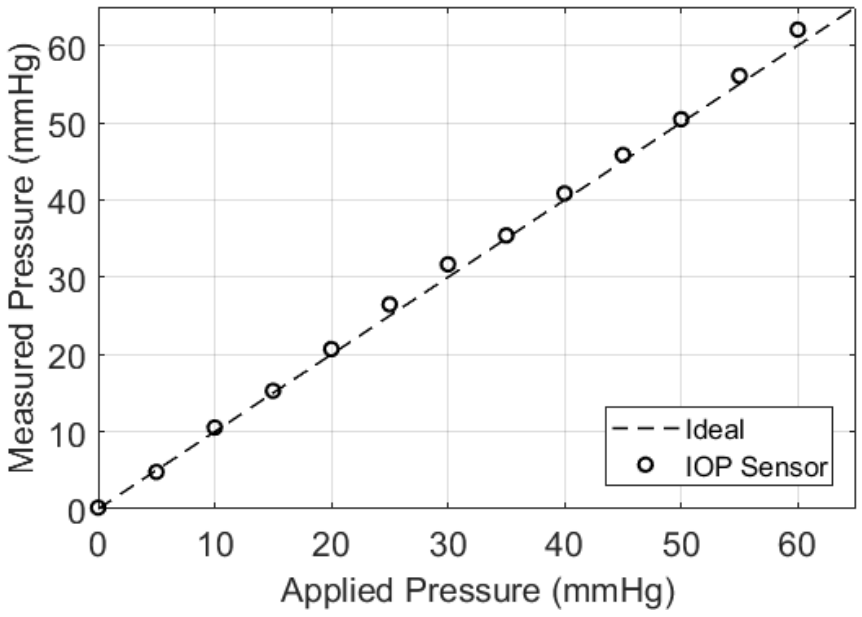

Figure 5.20: Measured pressure versus applied pressure for in vitro pressure measurements using the smartphone handheld reader.

5.5.4 Discussion

The smartphone handheld reader demonstrated the feasibility of a patient point-of-care IOP measurement system. The compact design and the use of a smartphone make the reader a practical solution to obtain optical readout of the interferometric pressure sensor.

The IOP app was developed on an Android platform to operate the reader. The system produced clear fringes with high visibility in a static setup. However, the image stabilization function of the phone was insufficient to allow for measurements in the handheld mode (freehand measurement).

The app was able to perform image processing algorithm to determine pressure values. However, this process is currently not yet optimized for the Android platform.

As smartphones become more advanced over time, with better cameras and faster processors, we expect that these shortcomings will be overcome.

5.6 Summary

In this chapter, we presented three different generations of a handheld reader used in the IOP measurement system. The first-generation reader was built to be a portable version of the lab setup with the use of the CMOS camera and the objective lens. While the reader allowed capturing of clear interference patterns in a static setup, the lack of image stabilization and short depth of field (3 μm) limited the use of the unit in a practical setting. For the second reader, we used a DSLR camera and a macro lens instead. With a larger field of view and depth of field, the DSLR unit was the most reliable reader for in vivo experimental measurement of rabbit's IOP. The third reader was built with the goal of making the reader more practical for patient care. A smartphone with a custom build app was integrated with a system of lenses to reduce the overall size of the reader and make the device more user friendly. It was found that the reader performed well in a static set up but failed to capture a clear fringe when used to measure IOP of rabbits in vivo. As camera technology of smartphone and personal devices continue to improve rapidly, we expect that the smartphone reader approach will provide reliable pressure reading as a patient point-of-care device.

Chapter 6

Ex vivo Investigation of an Optical Intraocular Pressure Sensor

6.1 Introduction

In this chapter, we explore different implantations and anchoring approaches to implant the IOP sensor. We also evaluate the response of the sensor ex vivo in the physiological pressure range using rabbit eyes to demonstrate the feasibility of using the IOP measurement system to track changes in eye pressure.

6.1.1 Implantation Sites

Since the IOP sensor requires direct optical access for fringe readout, an optimal region for implanting the sensor is in the anterior chamber of the eye. A cross sectional image of an anterior segment of a human eye is shown in Figure 6.1. Within this space, there are several viable approaches to position the sensor. First, the sensor can be incorporated in the intraocular lens and implanted during cataract surgery or refractive error correction surgery. Alternatively, the IOP sensor can be attached to a capsular tension ring and positioned in the sulcus space behind the iris. In this approach, an iridectomy procedure is required to provide optical access to the sensor. Lastly, the IOP can be anchored onto the surface of the iris using an iris fixation device, e.g., an iris claw.

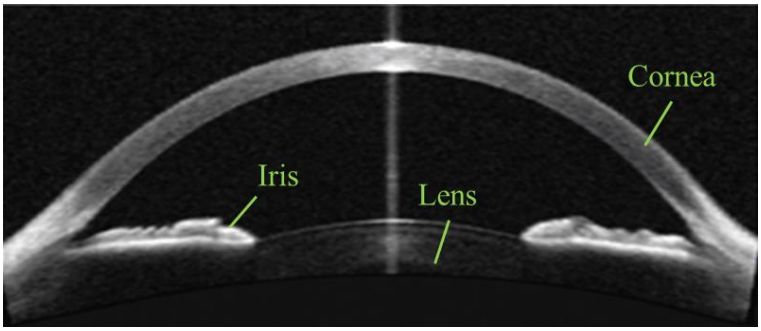

Figure 6.1: A cross sectional image of the anterior segment of a human eye captured using optical coherence tomography [153].

6.1.2 Cataract and Intraocular Lens

Cataract is an age-related medical condition where the native lens of the patient becomes cloudy and impairs vision. According to the National Eye Institute (NEI), cataract is one of the leading causes of blindness worldwide. There were 24 million of American who had cataracts in 2010 and this number is expected to raise to 50 million by 2050 [154]. Vision of cataract patients can be restored via cataract surgery, a lens replacement procedure. The procedure is being performed widely in the US and around the world with very high success rate (98% in the US [155]). It is one of the safest and most effective surgeries in the US.

Modern cataract surgery is done under local anesthesia and the procedure typically takes less than 15 minutes. The first step of the surgery is the phacoemulsification process of removing the native lens. The procedure utilizes ultrasound to break up the cloudy lens of the patient through a corneal incision and uses a suction probe to remove fragments of the lens preserving the capsular bag. Next, an artificial intraocular lens (IOL) is inserted into the eye through the same incision and positioned in place. An illustration of different stages of a cataract surgery is shown in Figure 6.2.

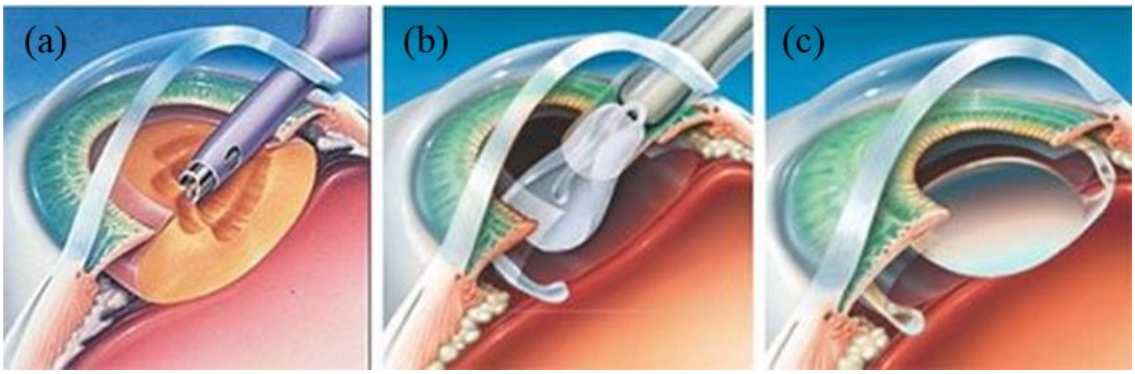

Figure 6.2: Illustration of a cataract surgery [156]: (a) phacoemulsification process of removing the native lens, (b) inserting the artificial lens using an IOL injector and (c) position the IOL in the capsular bag.

There are two main types of IOLs: pseudophakic IOLs which are used to replace the focusing function of the native lens in cataract surgery and phakic IOLs which are used to change the eye's optical power in treatment of refractive errors. Pseudophakic IOLs are implanted in the capsular bag and held in placed by haptics. Phakic IOLs are implanted in the anterior chamber of the eye and anchored by iris claws or supported by the irido-corneal angle. Traditionally, IOLs are made of rigid polymethyl methacrylate (PMMA) which require a large corneal incision (~6 mm) to insert the implant [157]. Recently, IOLs are made of flexible materials such as hydrophobic acrylic, hydrogel, or hydrophobic silicone [158]. These foldable and injectable IOLs are used in junction with phacoemulsification to reduce the corneal incision size to 3 mm or less and facilitate faster healing.

6.1.3 Capsular Tension Ring

Capsular tension ring (CTR) is a medical device that is implanted in the capsular bag to provide structure support during cataract surgery in which the zonules are weak or defective. The CTR has a circular contour that is designed to fit inside the capsular bag once the native lens is remove. This concept was first introduced by Hara et al in 1991

[159]. The Morcher CTR was the first CTR approved by the FDA in 2003. Since then, many companies have introduced their own designs and sold them worldwide. Applications of CTR have also expanded over the years, ranging from centering the placement of the IOLs, preventing capsular bag shrinkage post cataract surgery and simplifying the implantation procedure of foldable IOLs [160].

The CTR works by distributing the centrifugal force radially around the entire zonule structure. This reinforces the weaker zonule region and prevents the capsular bag from collapsing [161]. Figure 6.3 shows a schematic of how a CTR supports a capsular bag that has an area of zonular loss.

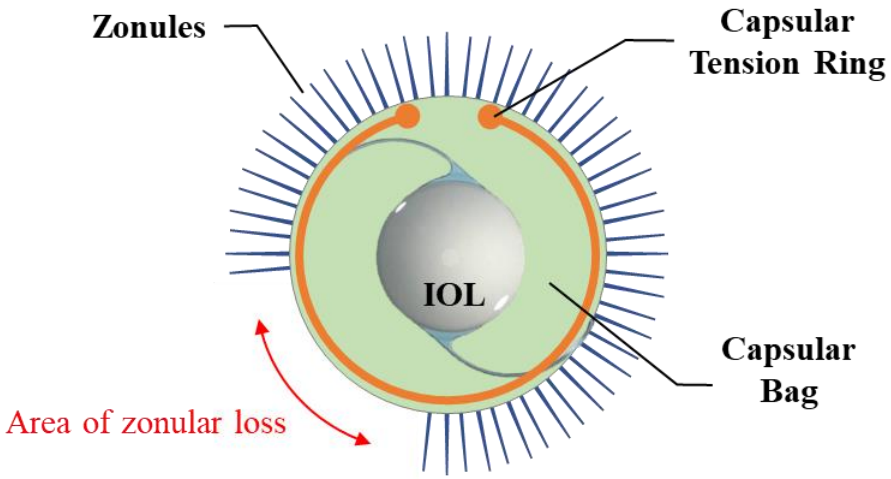

Figure 6.3: Schematic of how a CTR provides structure support to a capsular bag that has weak or defective region of zonules.

6.2 Intraocular Lens

In our research, we first explored the option of using a commercially available intraocular lens as a carrying substrate for the IOP sensor. We used one representative of each of the two different types of IOL for this study: Acrysof Multipiece IOL

(pseudophakic lens) and Artisan IOL (phakic lens). Once the calibrated IOP sensors were incorporated in the IOLs, the units were then implanted in rabbit eyes for ex vivo study.

6.2.1 Sensor Fabrication and Integration

Two IOP sensors were prepared for this study using the fabrication process outlined in detail in chapter 2. Figure 6.4 illustrates the assembly and components of the sensor. A 10 µm layer of SU-8 was patterned on 200 µm SiN-coated glass substrate using standard photolithography. A 200-nm silicon nitride diaphragm mounted on 200 µm silicon substrate was aligned and bonded to the glass substrate. The unit was then sealed with medical grade epoxy and diced to the final size of 1.5 x 1.5 x 0.4 mm.

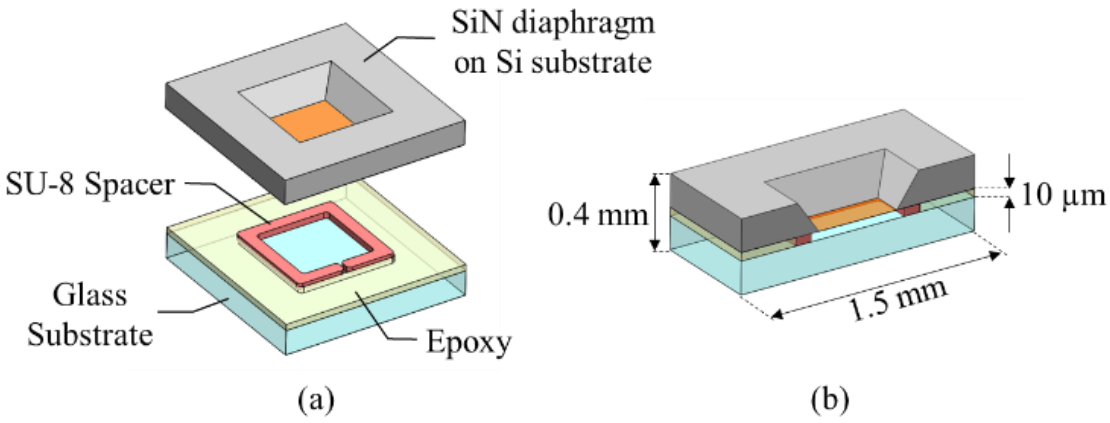

Figure 6.4: (a) Schematic of optical IOP sensor and (b) cross sectional view and dimensions of the sensor.

Next, we positioned the IOP sensors on the intraocular lenses and bonded them together using UV epoxy (Loctite 3936) for the implantation. The epoxy was cured using a 6W 365nm UV curing lamp for 15 minutes to ensure a strong bond between the sensor and the IOL. Figure 6.5 shows a picture of the fabricated IOP sensor and pictures the IOP sensor integrated to the pseudophakic lens (Sensor 1) and the phakic lens (Sensor 2).

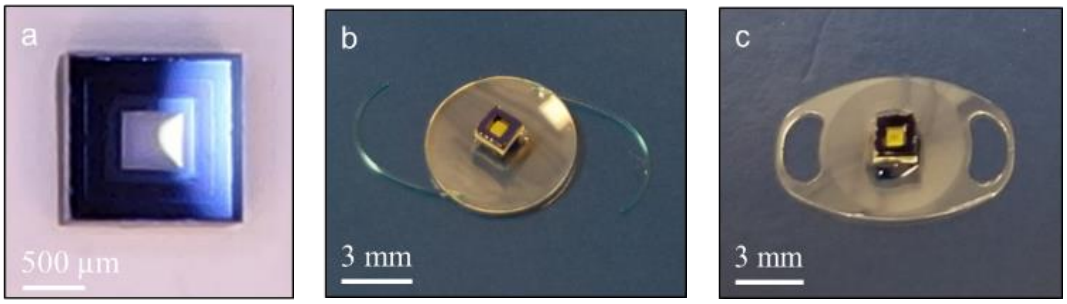

Figure 6.5: Photographs of (a) fabricated IOP sensor, (b) sensor integrated to Acrysof Multipiece IOL and (c) sensor integrated to Artisan Phakic IOL.

6.2.2 In vitro calibration

Before implantation, the response of each of the two sensors was characterized using an artificial anterior chamber (Katena) to simulate the pressure condition in the eye (

Figure 6.6). A balance salt solution (BSS) column was connected to a pressure regulator (Proportion Air) and used to precisely control the hydrostatic pressure (±0.1 mmHg) inside the artificial anterior chamber. Interference fringe patterns were obtained as a function of the applied pressure and captured by the CMOS camera for analysis.

The maximum deflection of the sensor diaphragm was determined from the fringe patterns and plotted as a function of the applied pressure (

Figure 6.7). The results were used to obtain the calibration curve for each sensor. The sensitivities of Sensor 1 and Sensor 2 were determined to be approximately 23 nm/mmHg and 22 nm/mmHg, respectively.

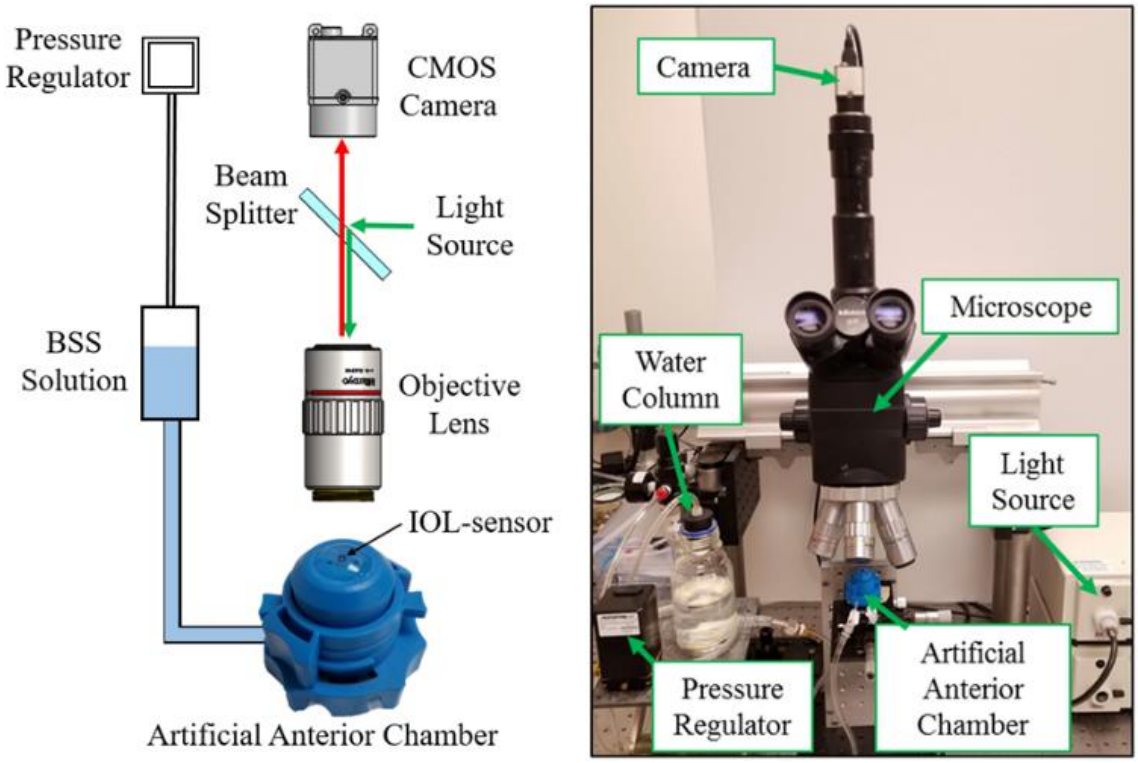

Figure 6.6: Schematic and photograph of experimental setup using artificial anterior chamber.

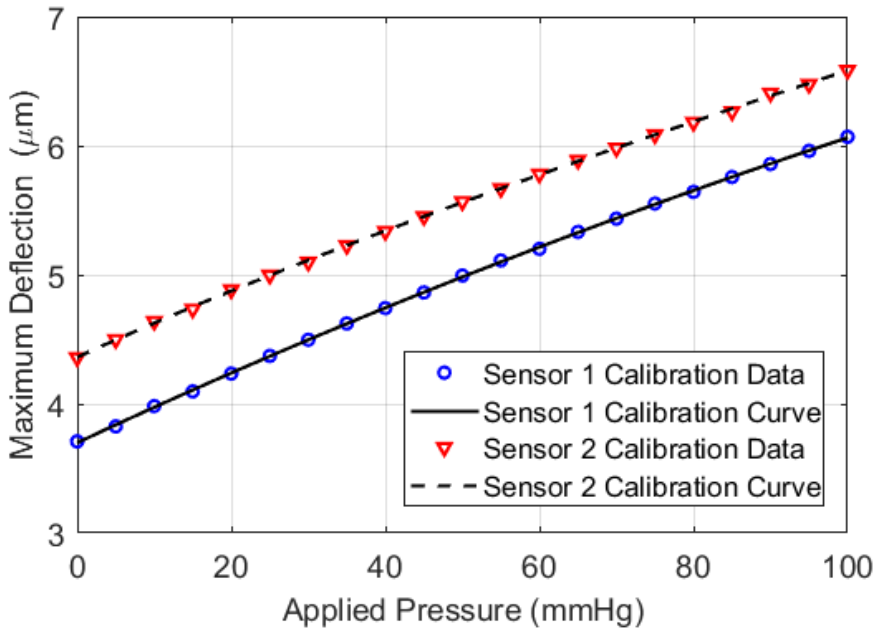

Figure 6.7: Sensor diaphragm deflection as a function of pressure.

6.2.3 Implantation

The two IOL units were implanted in euthanized New Zealand white rabbits to investigate the ex vivo response of the sensor. The Acrysof Multipiece IOL was implanted into the capsular bag using standard cataract surgery procedure, while the Artisan Phakic IOL was implanted in the anterior chamber and anchored on top of the iris using iris-claws via standard refractive error correction procedure. Photographs of the implanted units are shown in Figure 6.8.

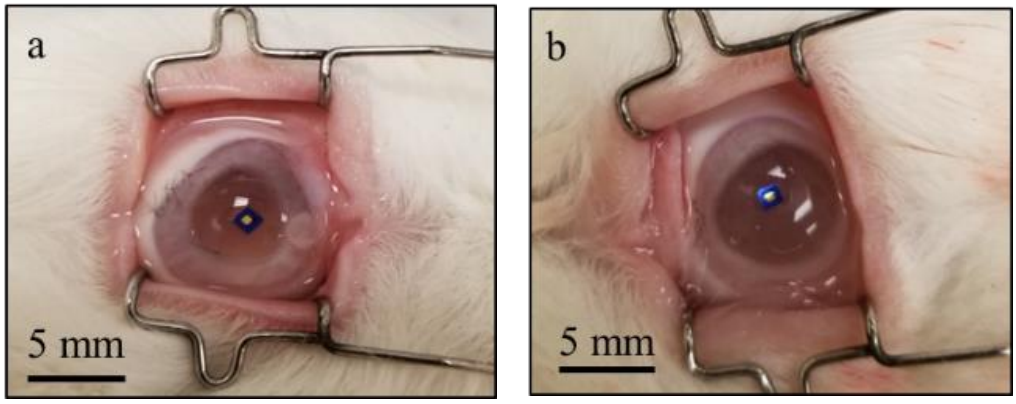

Figure 6.8: Photographs of IOP sensors integrated to (a) Acrysof Multipiece IOL and (b) Artisan Phakic IOL post implantation.

6.2.4 Ex vivo Experiment

Once the sensor units were implanted, a hydrostatic pressure regulator was connected to the posterior chamber using a 20-gauge needle to control pressure inside the rabbit eyes (Figure 6.9). As pressure was varied, interference fringe patterns were captured and analyzed to determine the pressure.

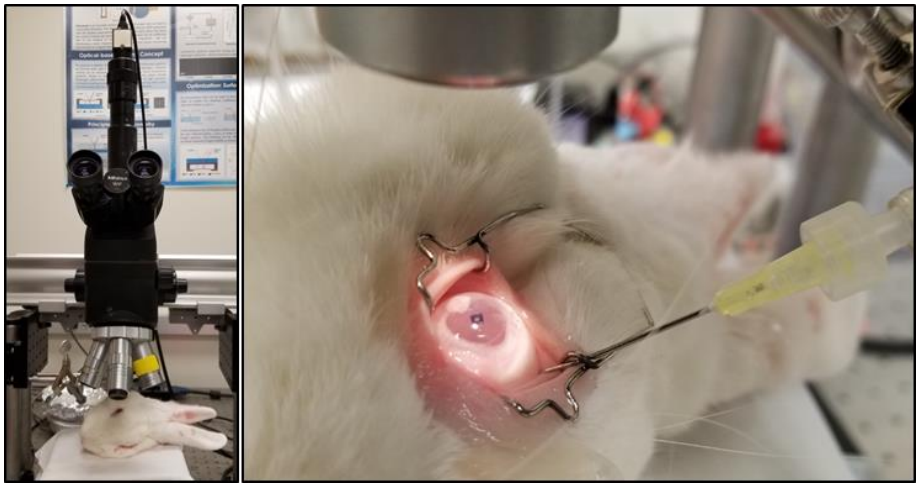

Figure 6.9: Ex-vivo experimental setup. 20-gauge needle was used to connect the pressure regulator to the posterior chamber of the rabbit eye.

Figure 6.10 shows ex-vivo IOP measurements of Sensor 1 for three load cycles, from 12 – 60 mmHg, with a step size of 2 mmHg. Pressure measurements obtained from the sensor showed good agreement with applied pressure with an average error of ±1 mmHg.

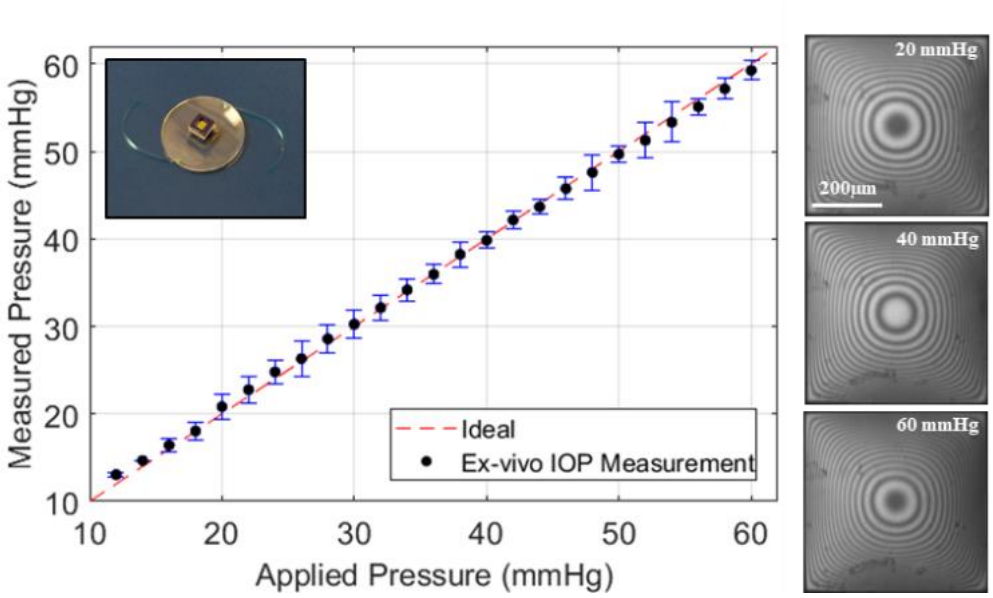

Figure 6.10: Measured versus applied pressure for ex-vivo measurements. Measurement taken using sensor integrated to an Acrysof Multipiece IOL.

Figure 6.11 shows results of Sensor 2 for three load cycles from 30-60 mmHg with a step size of 2 mmHg. The average error was determined to be ±0.5 mmHg.

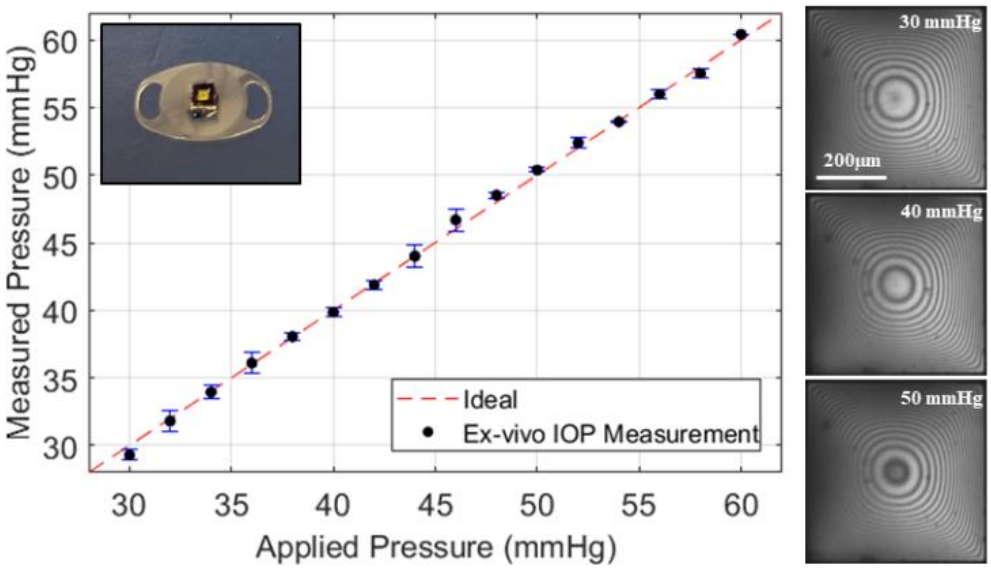

Figure 6.11: Measured versus applied pressure for ex-vivo measurements. Measurement taken using sensor integrated to an Artisan Phakic IOL.

6.2.5 Discussion

In this study, we have successfully performed ex vivo IOP measurements from our optical intraocular pressure measurement system. The sensor was integrated onto two types of intraocular lenses and surgically implanted into a rabbit eye using standard cataract surgery and refractive error correction procedures.

There was a slight difference in sensitivity and initial deflection of the two sensors. These differences were due to variations in fabrication. In clinical application, each sensor can be calibrated before implantation to account for variations in fabrication. The sensor can also be calibrated post implantation using standard IOP measurement techniques to account for any drifting over time.

Once implanted, intraocular pressure was measured using a benchtop microscope and a portable hand-held reader. The results show that the system has a sensitivity of 22 nm/mmHg and an accuracy as high as ±0.5 mmHg post implantation.

The accuracy of the same IOP sensor obtained in vitro testing using the Katena artificial anterior, ±0.2 mmHg, was better than ex vivo testing in rabbits, ±0.5 mmHg. This was largely due the difficulty of creating a tight seal of the anterior chamber of the rabbit eye after implantation. The 6 mm corneal incision was sealed using sutures. However, since there was no active wound healing ex vivo, fluid slowly leaked out of the incision as pressure in the eye increased making it difficult to maintain a stable pressure inside the rabbit eye.

The average error from the IOP sensor integrated to the pseudophakic IOL was slightly larger than that of the IOP sensor integrated to the phakic IOP. This is most likely because the pseudophakic IOL was positioned further away from the cornea (~4 mm as opposed to ~2 mm in the case of the phakic IOL), which affected the optical readout quality of the sensor.

6.3 Capsular Tension Ring

Another promising implantation approach is to integrate the sensor to a capsular tension ring. Though capsular tension rings are typically place inside the capsular bag during cataract surgery, it can also be placed in the sulcus, the space between the iris and the capsular bag. The sensor can be attached to one of the ends of the CTR and implanted in the sulcus. Since we need direct optical access to the sensor for IOP measurement, we

would need to remove part of the iris to expose the sensor underneath via an iridectomy procedure. A schematic of this implantation approach is shown in Figure 6.12.

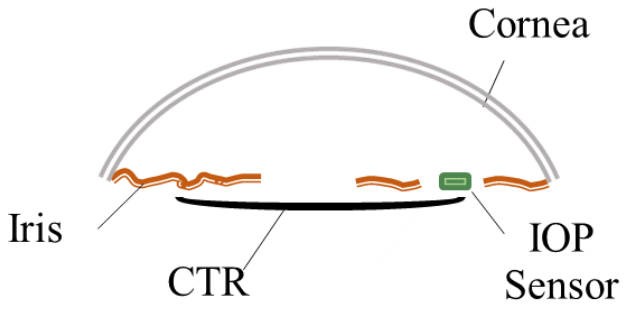

Figure 6.12: Schematic of the capsular tension ring implantation approach. The sensor is integrated to an CTR and placed in the sulcus space. Iridectomy procedure provides an opening for direct optical access to the sensor.

6.3.1 Sensor Integration and Implantation – Flat Position

The calibrated IOP sensor was positioned onto one of the ends of the CTR and secured in place using UV epoxy (Locttite 3325). The epoxy was cured using a 6W 365nm UV curing lamp for 1 hour to ensure strong bonding between the sensor and the CTR. A photograph of the integrated unit is shown in Figure 6.13.

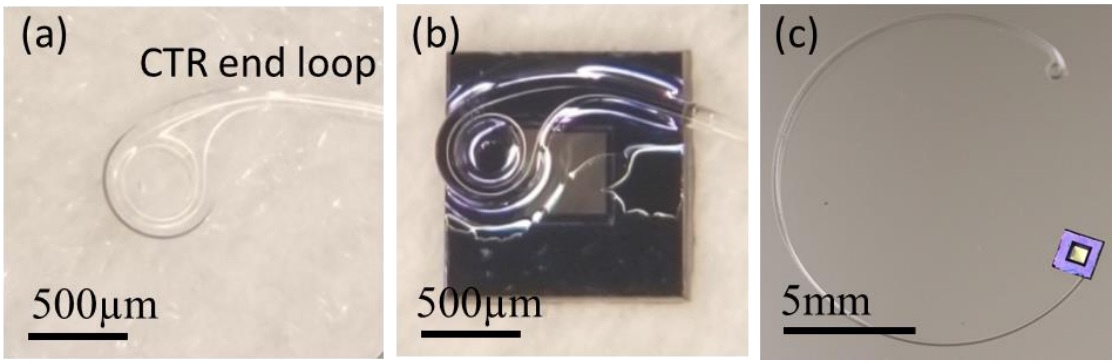

Figure 6.13: Photograph of (a) capsular tension ring end loop, (b) CTR end loop bonded to the back side of the IOP sensor, (c) IOP sensor integrated to a capsular tension ring.

The unit was then implanted in a rabbit eye ex vivo. First, an iridectomy procedure was performed to remove part of the iris through a 2-mm incision at the base of the cornea. The sensor-CTR unit was then inserted into the eye through the same incision. The unit was rotated and positioned so that the CTR was underneath the iris (in the sulcus space) and the sensor was visible through the iris opening. A photograph of the unit after the implantation procedure is shown in Figure 6.14. The sensor was clearly visible through the iridectomy site and the CTR was secured in place behind the iris.

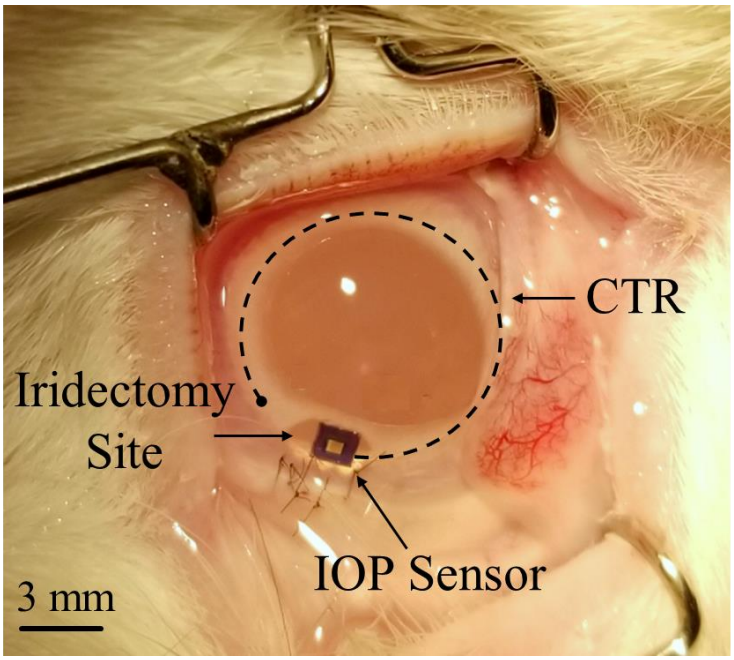

Figure 6.14: Photograph of the sensor-CTR unit post implantation. Outline of the CTR is shown in green.

6.3.2 Ex vivo Experiment - Flat Position

The DSLR handheld reader was used to conduct the ex vivo experiment with the sensor-CTR unit. We were not able to obtain interference fringes from the sensor. This can be caused by several reasons: local damage to the cornea due to suturing caused aberration.

The curvature of the cornea distorted the light as it is directed toward the sensor. As mentioned in chapter 3, the incident angle of the monochromatic light should be in the range of ±6° for optimal readout. This hypothesis was confirmed in the next test: taking measurement as the region of cornea directly above the sensor was flattened. A schematic of this test is shown in Figure 6.15. Fringe patterns was clearly captured in this test suggesting that the surface of the sensor should be position parallel to the cornea for optical readout.

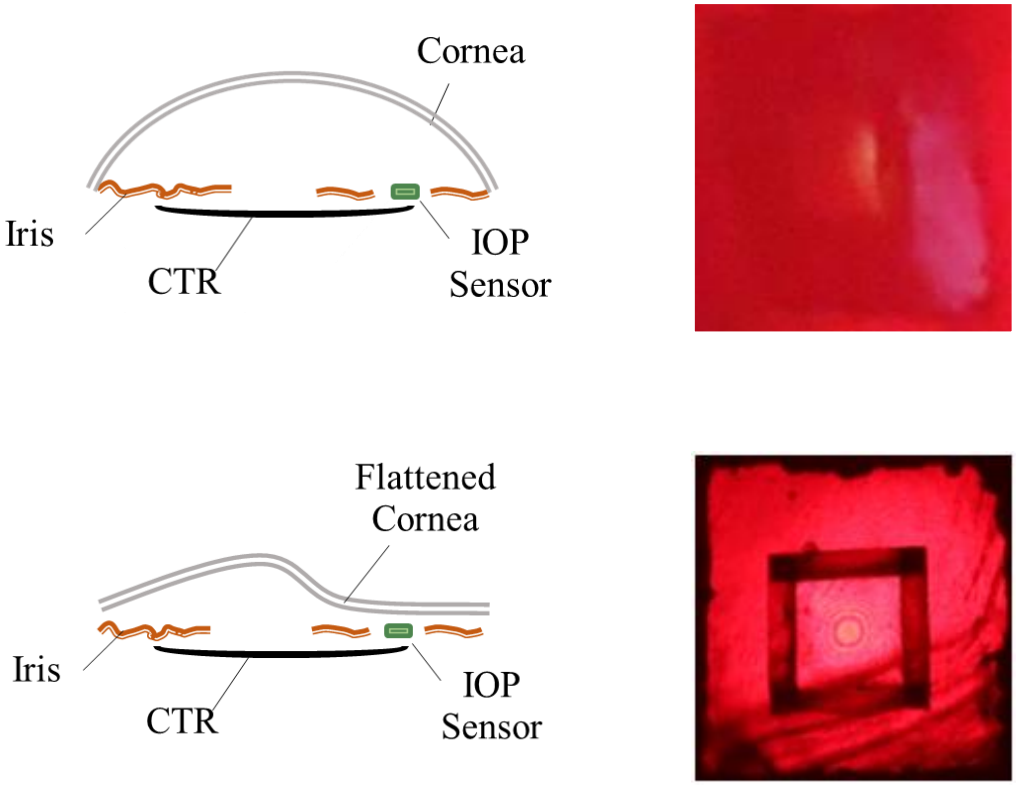

Figure 6.15: Differences in sensor orientation on the capsular tension ring (CTR).

6.3.3 Sensor Integration and Implantation - Angled Position

Based on the ex vivo results from the flat configuration, we modified the bonding angle between the IOP sensor and the CTR to 45° so that the surface of the sensor is parallel to the cornea.

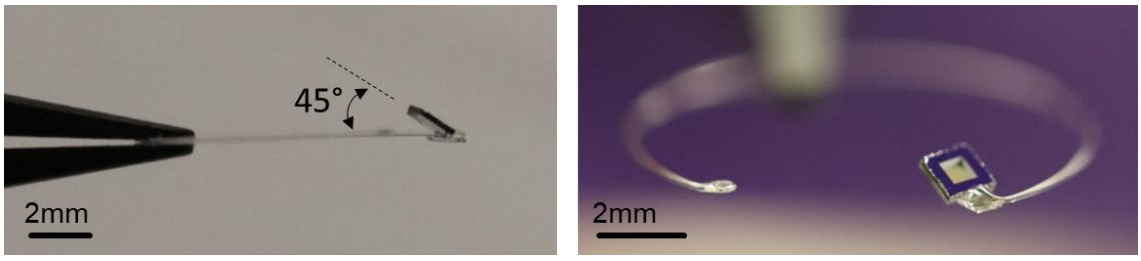

Figure 6.16: Photograph of the IOP sensor bonded to the capsular tension ring at a 45° angle. Side view of the unit (left) and isometric view of the unit (right).

The sensor unit was inserted into the anterior chamber and placed on top of the iris in this experiment. The IOP sensor was positioned away from the incision site to avoid any aberrations due to the suturing. A photograph of the of the sensor in the anterior chamber is shown in Figure 6.17.

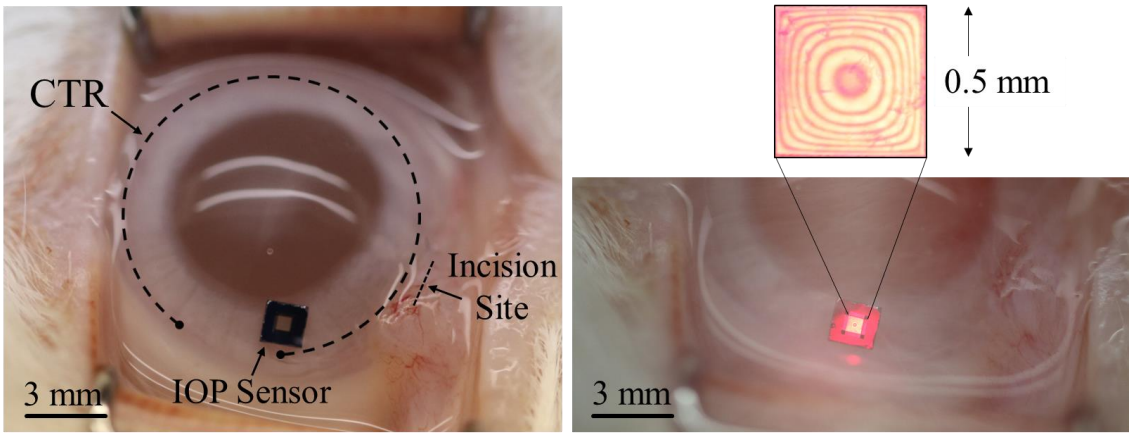

Figure 6.17: Photograph of sensor after implantation (left) and appearance of interference fringes when monochromatic light was directed to the sensor (right).

6.3.4 Ex vivo Experiment - Angled Position

As shown in Figure 6.17, interference fringes were clearly visible when monochromatic light was directed toward the implanted sensor. The DLSR reader was used to capture the response of the sensor as the eye pressure was varied from 18-42 mmHg via a 20-gauge needle. Fringe patterns were analyzed, and the ex vivo experiment results are plotted in Figure 6.18.

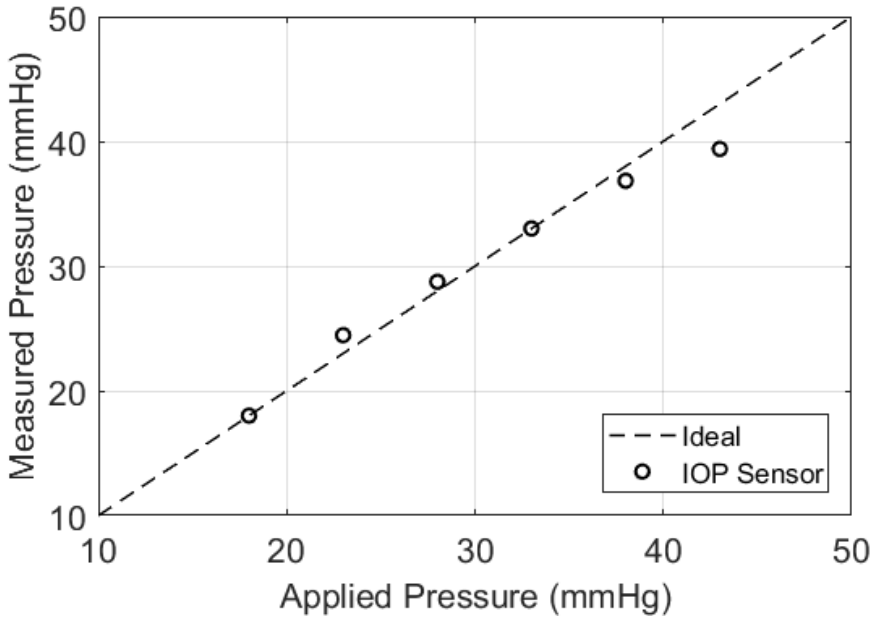

Figure 6.18: Ex vivo IOP measurements using an IOP sensor mounted on a capsular tension ring at a 45° angle.

6.3.5 Discussion

The capsular tension ring implantation approach was performed to address the following two goals: (1) to evaluate the feasibility of using the CTR as a carrier for the IOP sensor and (2) to evaluate the optical readout quality of the sensor placed off the visual axis.

The CTR implantation approach provided some advantages over the IOP implantation approach. First, the smaller corneal incision size (~2mm) allows for faster healing of the cornea. Second, cataract surgery is not required in this case and the native lens remains intact. This will open the applications for a wider patient population. However, this approach requires an iridectomy procedure to remove part of the iris and provide optical access to the IOP sensor. Though this is a relatively simple procedure, it presents increased surgical risk and produced an undesired permanent hole in the iris. Overall, the CTR implantation approach still provides a viable option to secure the IOP in the anterior chamber.

As shown in the results above, we were not able to capture interference fringes in the flat sensor-CTR configuration. However, once we changed the bonding configuration to a 45° angle, we were able to capture interference fringes in the ex vivo experiment. This can be seen through the ray trace diagram shown in Figure 6.19.

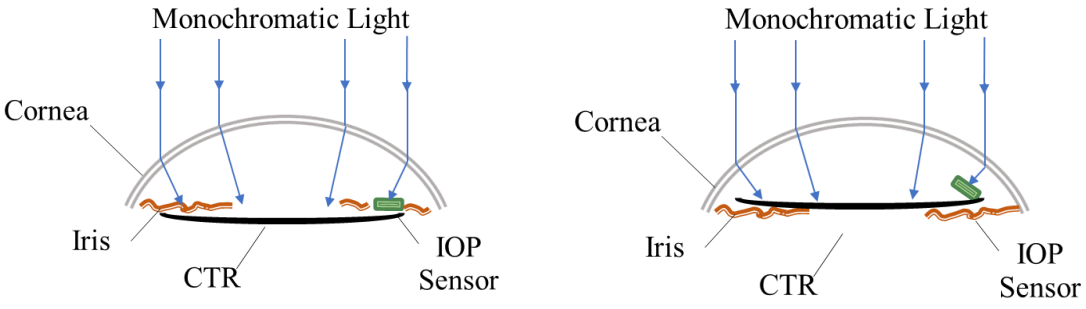

Figure 6.19: Light ray trace diagram as light travels through the cornea and arrives at the IOP sensor. The sensor is placed at a horizontal position (left). The sensor is placed at a 45° angle (right).

Since the cornea acts as a lens, light is focused toward the middle of eye as it travels through the cornea. Hence, the monochromatic light was directed straight at the eye, the

incident angle toward the sensor was much larger than 6° and no interference fringes were observed. As we tilted the sensor to account for the focusing effect of the cornea, the incident angle toward the sensor was within ±6° and we were able to obtain IOP measurement.

6.4 Iris Claw

Another implantation approach that we have considered is to anchor the sensor on top of the iris using iris claws via a stand-alone surgical procedure.

6.4.1 Sensor Integration and Implantation

The iris claw was prepared by modifying the Artisan phakic IOL (Ophtec) as shown in Figure 6.20 (a). The lens portion of the IOL was removed and the claw portion was retained as the anchoring substrate for the IOP sensor. Next, UV cured epoxy (Loctite 3936) was used to bond the glass side of the IOP sensor to the claw. Once inserted into the anterior chamber of the eye through a 3 mm corneal incision, the implant was positioned on top of the iris such that the IOP sensor was pointing toward the center of the eye. The iris tissue was then gently lifted through the haptic slot of the claw to anchor the implant. Figure 6.20b and Figure 6.20c. shows photographs of the IOP sensor and the iris claw before and after implantation.

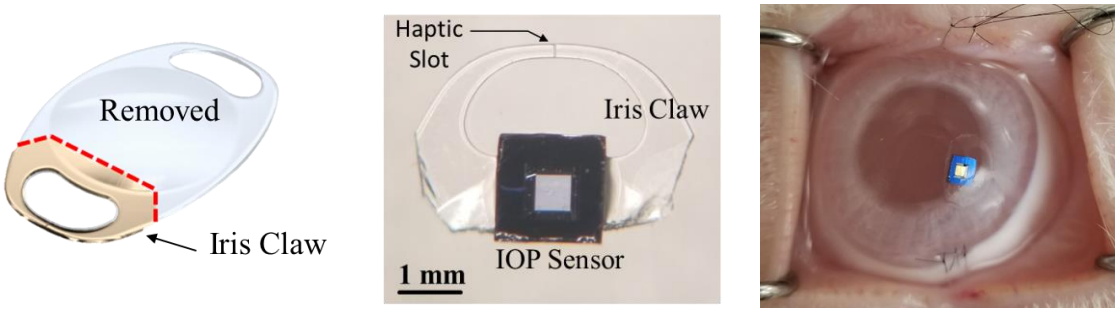

Figure 6.20: (a) Iris claw cut out from Ophtec Artisan lens, (b) IOP sensor integrated to the iris claw and (c) IOP sensor implanted on the surface of the iris.

6.4.2 Ex vivo Experiment

We conducted an ex vivo experiment after the IOP sensor was implanted in the eye of the rabbit. A 20-gaugle needle was inserted into the anterior chamber through the surgical incision to control the pressure inside the eye. We applied a pressure load of 18 – 53 mmHg with a step size of 5 mmHg to the eye and used the DSLR reader to capture the response of the sensor. The results of the experiment are shown in Figure 6.21.

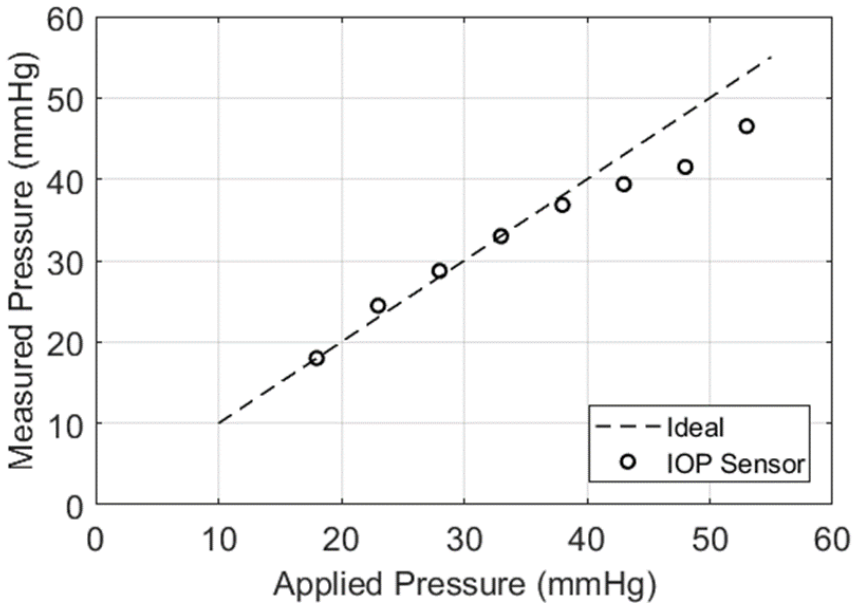

Figure 6.21: Ex vivo experiment using the iris claw.

6.4.3 Discussion

The results from the iris claw experiments demonstrate the feasibility of implanting the IOP sensor on the iris. The current prototype leveraged the claw portion of the Artisan lens as the anchoring device. While using this pinching method to anchor the sensor, it is important to pull adequate amount of iris tissue through the haptic slot to make sure that the implant is stable and secure in place.

The ex vivo results show that the measurements from the optical readout of the sensor produced very good accuracy. This demonstrated potential to implant the sensor on the iris using a claw or clip for anchoring. The measured pressure agreed well with the applied pressure in the range of 18 mmHg to 40 mmHg. The measurements for pressure load >40 mmHg showed an underestimation of pressure due to leakage at the suture site.

To reduce the size of the anchoring component, we have designed a vertical iris claw as shown in Figure 6.22. The pinching mechanism is very similar to that of the Ophtec lens. This iris claw design will be implemented using a micro-CNC machine.

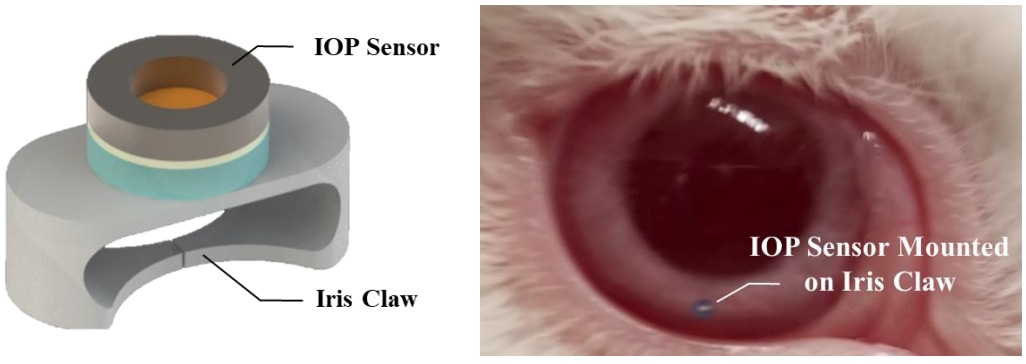

Figure 6.22: Render image of the IOP sensor and the vertical iris claw (left) and proposed implant location of the IOP sensor and iris claw in the eye (right).

6.5 Summary

In this chapter, we presented three different approaches to investigate the response of the IOP sensor ex vivo. First, the sensors were incorporated into two different types of intraocular lenses and implanted via cataract surgery. Placement along the visual axis allows the sensors to have excellent fringe visibility. Ex vivo measurements of the intraocular pressure were obtained using the bench top setup with high accuracy (<0.5 mmHg).

The second implantation approach utilized capsular tension rings as the delivering substrates for the sensors. We found that the sensor mounted at a 45° angle with respect the horizontal plane of the capsular tension ring could generate high quality interference fringes. Ex vivo IOP measurements were obtained using the DSLR reader. The results were in good agreement with the applied pressure.

Lastly, the IOP sensor was successfully implanted in the anterior chamber and anchored on top of the iris using an iris claw made from the Artisan phakic lens. This approach allowed the sensor to position away from the visual axis and still have good optical response in a stand-alone surgical procedure, i.e., without the need for cataract surgery. We also proposed a design for a vertical iris claw that minimizes the corneal incision size and allows for easy of implementation.

Chapter 6, in part is a reprint of the material as it appears in "Optical intraocular pressure measurement system for glaucoma management," Phan, Alex, Phuong Truong, Alexander Kief, Milien Dhorne, Andrew Camp, Robert N. Weinreb, and Frank E. Talke, *2017 IEEE Healthcare Innovations and Point of Care Technologies (HI-POCT)*, Bethesda,

MD, 2017, pp. 188-191. The dissertation author was the primary investigator and author of this paper.

Chapter 7

Implantation of an Optical Pressure Sensor in Live Rabbits

7.1 Introduction

In Chapter 6, we demonstrated a proof of concept of the IOP measurement system. Ex vivo studies showed that accurate IOP measurements could be obtained in the physiological range of 0 – 60 mmHg using an optical readout system. Next, we want to demonstrate the feasibility of using the IOP measurement system to measure IOP frequently on a living subject. In vitro and ex vivo studies are usually conducted in a highly controlled environment, e.g., static setup, optimal lighting, no space and time constraints. However, real live testing environments are much different from a controlled setting. In this chapter, we evaluate the response of the sensor in vivo by comparing the pressure measurements with a tonometer. We also conduct a histology study to investigate how the body responds to the implant. Finally, we will assess the biostability of the implant to determine the effect of the biological environment on the characteristic of the implanted sensor.

7.1.1 iCare tonometer

The iCare tonometer is a medical device used to measure intraocular pressure based on the principle of rebound tonometry [162]. During IOP measurement, the tonometer

ejects a probe toward the eye and characterizes the motion of the probe as it makes contact with the cornea. The probe is made from a magnetized steel wire and a round plastic end cap. When the probe hits the cornea, it decelerates and bounces back to the device. Since the probe is magnetized, it's motion during contact with the cornea can be measured using an induction coil system built in the tonometer. The software algorithm in the device determines the deceleration and the contact time. When the eye pressure is low, the probe decelerates slowly, and the contact time is relatively long. When the eye pressure is high, the probe decelerates fast and the contact time is shorter. Therefore, by analyzing the motion of the probe, the tonometer can determine the eye pressure. During one measurement, the probe is ejected six times and the tonometer acquires six readings. The highest and lowest values are discarded and the average of the other four is recorded as the measured IOP value.

7.1.2 Rabbits

We used New Zealand White (NZW) rabbits in our in vivo study. Rabbits (5.6-6.6 lbs) were obtained from Western Oregon Rabbit Company and housed inside the UC San Diego animal facility during the study. All procedures and experiments conducted on the rabbits adhere to the protocol approved by the Institutional Animal Care and Use Committee (IACUC) of UC San Diego.

7.2 First Round of Implantation

The goals of this first round of in vivo study were to (1) demonstrate the ability to measure eye pressure in a live rabbit using the IOP measurement system, (2) compare the pressure measurement results of the implantable sensor with a tonometer, and (3) evaluate

the biocompatibility of the sensor during the 10-week study. In this investigation, we used an anterior intraocular lens as the carrier for the IOP sensor. The sensors were implanted during cataract surgery. Handheld IOP readers and a rebound tonometer were used to obtain IOP measurements. The rabbits were euthanized at the end of the study and the sensors were removed for post implantation analysis.

7.2.1 Sensor Preparation

Two IOP sensors were first fabricated using the 2-stage bonding technique described in Chapter 2. The sensors were then coated with a 1 μm thick layer of parylene-C (PDS 2010 Parylene Coater). An Acrysof IOL (Alcon) and a 3-piece IOL (Alcon) were used as the carry substrate for the IOP sensors in this study. The two sides of the IOLs were removed using a surgical blade to reduce the width of the lenses to 3.5mm and, hence, minimize the size of the corneal incision. The IOP sensors were mounted on the IOL (diaphragm facing outward) with a small amount of UV medical grade epoxy (Loctite 3936). The epoxy was fully cured for 15 min using a 6W 365nm UV curing lamp (Edmund Optics). The units were individually bagged in a pouch and sterilized using ethylene oxide for the implantation. Photographs of the two integrated IOP sensor and IOL units are shown in Figure 7.1.

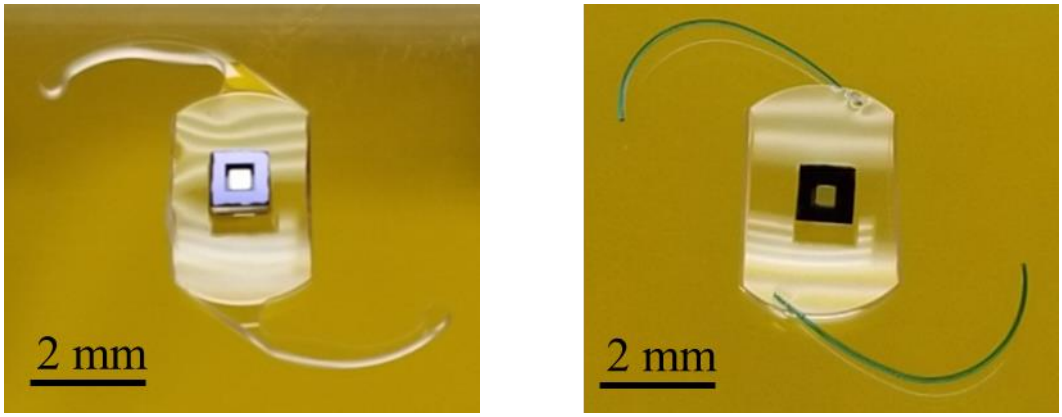

Figure 7.1: Photographs of the IOP sensors integrated to modified intraocular lenses.

7.2.2 Sensor Implantation

Two NZW rabbits were prepared for IOP sensor implantation via cataract surgery. After anesthesia was induced by ACP veterinary services, topical ophthalmic proparacaine was applied to the right eye of the rabbit to provide local anesthesia during sterile preparation. The eye and adnexa of the operative eye were sterilized using 5% betadine ophthalmic solution. The rabbit was draped with standard sterile ophthalmic drapes with only the operative eye exposed. A 2.4 mm tri-planar corneal incision was made using a keratome blade. Ophthalmic viscoelastic was injected into the anterior chamber to keep the chamber inflated during the procedure. The native lens was then removed by phacoemulsification. After the lens was completely removed, the corneal incision size was increased to approximately 5 mm to accommodate the artificial lens without folding. The IOL-sensor unit was inserted into the eye and positioned inside the capsular bag using forceps. Next, the corneal incision was closed using 10-0 nylon sutures. After sealing, the incision was examined to ensure it was watertight to minimize the risk of infection. Lastly,

since the eye of the rabbits showed significant amount of inflammatory responses, e.g. presence of fibrin, a 10 mg of triamcinolone was injected in the inferior fornix of the eye and in the anterior chamber to provide continuous anti-inflammatory medication exposure. Photographs of the implantation procedure are shown in Figure 7.2.

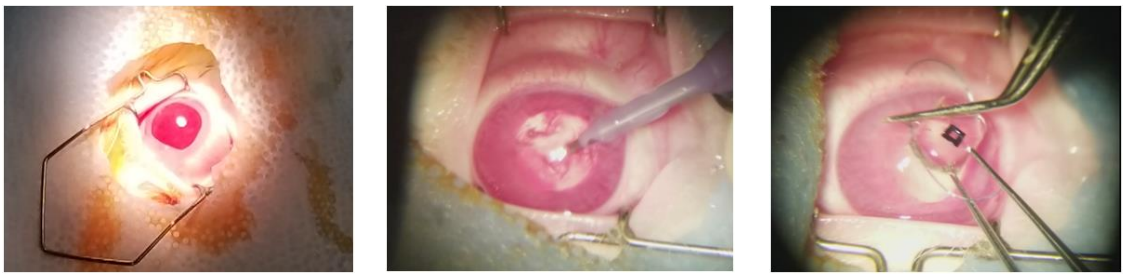

Figure 7.2: Photographs of (a) the rabbit eye before implantation (b) the phacoemulsification process of removing the native lens, (c) the IOP-sensor unit being inserted into the capsular bag.

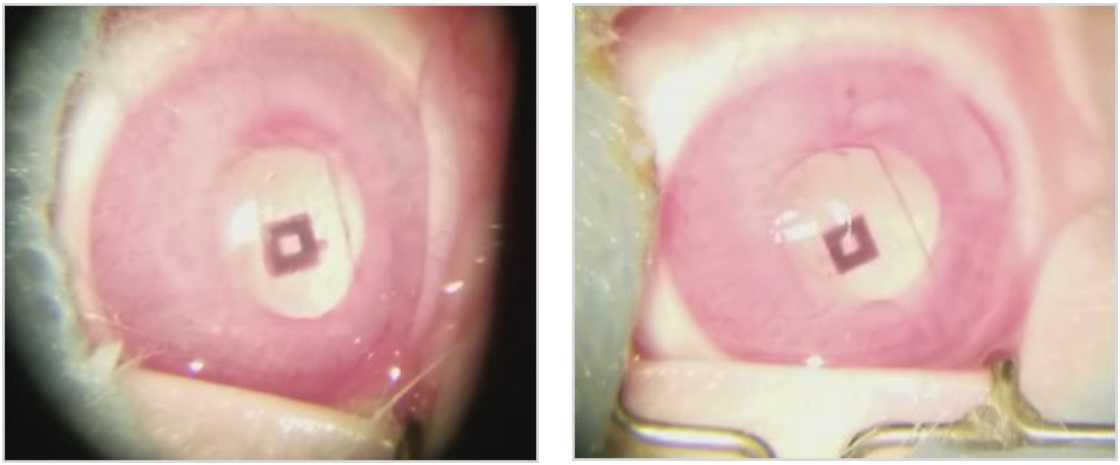

Figure 7.3: Photographs of the implanted sensor in rabbit #1 (left) and rabbit #2 (right).

7.2.3 Sensor Calibration

Before implantation, calibration tests on each of the two IOP sensor were performed *in vitro* using the Katena artificial anterior chamber setup to characterize the response of

the sensors. At the end of the in vivo study, we removed the sensors from the rabbit eyes and conducted post-implantation calibration tests. The calibration results from pre-implantation and post-implantation tests were plotted together in Figure 7.4 for comparison. We can observe that there was a baseline drift in the response of the sensor. At zero pressure load the maximum membrane deflection changed from 2.1µm before the in vivo study to 2.9µm after the study (70 days). Hence, the baseline drift of the sensor is determined to be approximately 0.01 µm/day.

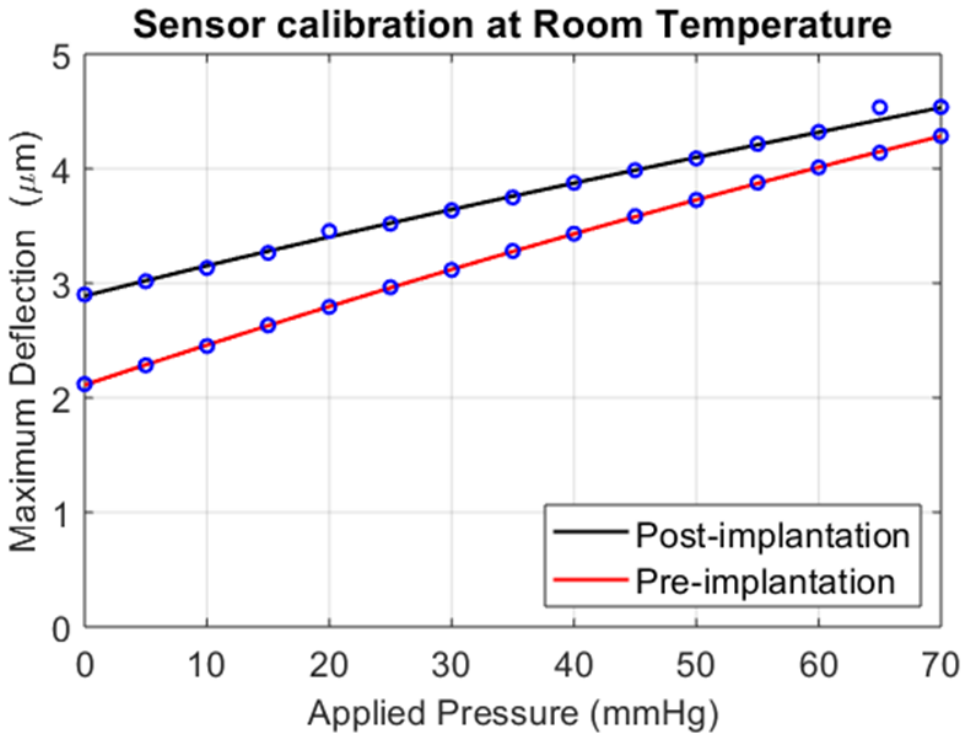

Figure 7.4: Comparison of sensor calibration before and after implantation.

7.2.4 IOP Measurements

Three different approaches were used to obtain IOP measurement on the rabbits in this study: the first generation handheld reader, the DSLR reader and the iCare tonometer.

The steroid, triamcinolone, injected into the rabbit eye at the end of the surgery is an off-white suspension and therefore made the anterior chamber cloudy, blocking the optical access to the IOP sensor. Once the triamcinolone fully dissolved (after 2 weeks), the anterior chambers of the rabbits were clear and the implanted IOP sensors were fully visible as shown in Figure 7.5.

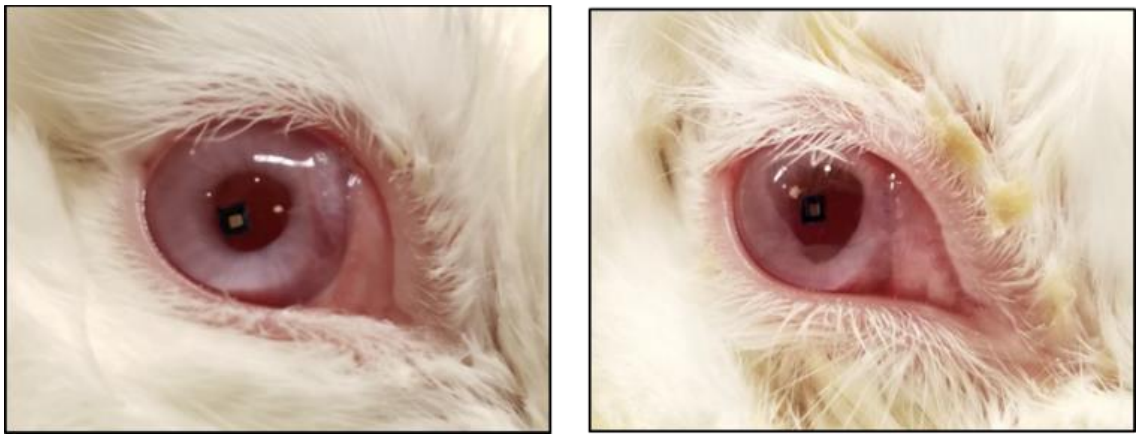

Figure 7.5: Photographs of the IOP sensors in rabbit eyes 3-week post implantation.

First, we attempted to take an IOP measurement using the first handheld reader. The rabbits were removed from the cage, gently wrapped in a small blanket to restrain their motion. The reader was positioned at 50 mm away from the rabbit eye. Although the rabbits remained calm throughout the measurement process, the movement caused by breathing and slight shaking of the hands made it difficult to locate the sensor and keep it in the focal plane. Instead of taking a picture of the fringe pattern, we decided to capture a 30 second video of the sensor while directing monochromatic light to the rabbit eye. We then looked at individual frames of the video and performed image processing on those frames that had the fringe pattern in focus to determine the IOP pressure. Figure 7.6. shows an image of the interference pattern captured using the handheld reader.

After obtaining an image of the fringe pattern, we compared it with the calibration curve obtained prior to implantation to determine the pressure. An example of how to determine a single IOP measurement point is shown Figure 7.6.

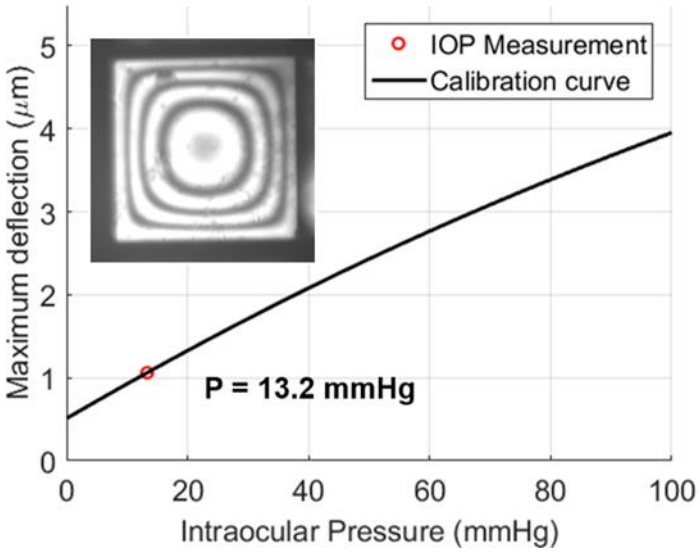

Figure 7.6: Image of fringe pattern was captured, analyzed and compared with the calibration curve to determine IOP.

Next, IOP measurement were taken using the DSLR reader. We were able to obtain eye pressure measurement with the rabbit unrestrained or gently restrained on a table top (Figure 7.7). The reader was positioned about 100 mm away from the rabbit cornea. Since the field of view of the reader is large (8 mm x 12 mm), it was relatively easy to locate the sensor. Once the sensor is in view, we adjusted the camera so that the incident angle of the monochromatic light was within the $\pm 6^{o}$ to generate a clear fringe pattern. We then captured the interference pattern as they came in focus for pressure measurement. As previously described in Chapter 4, we were able to use the auto focus and image stabilization function of the DSLR and the lens to obtain multiple IOP measurements within a much shorter time (<10 seconds).

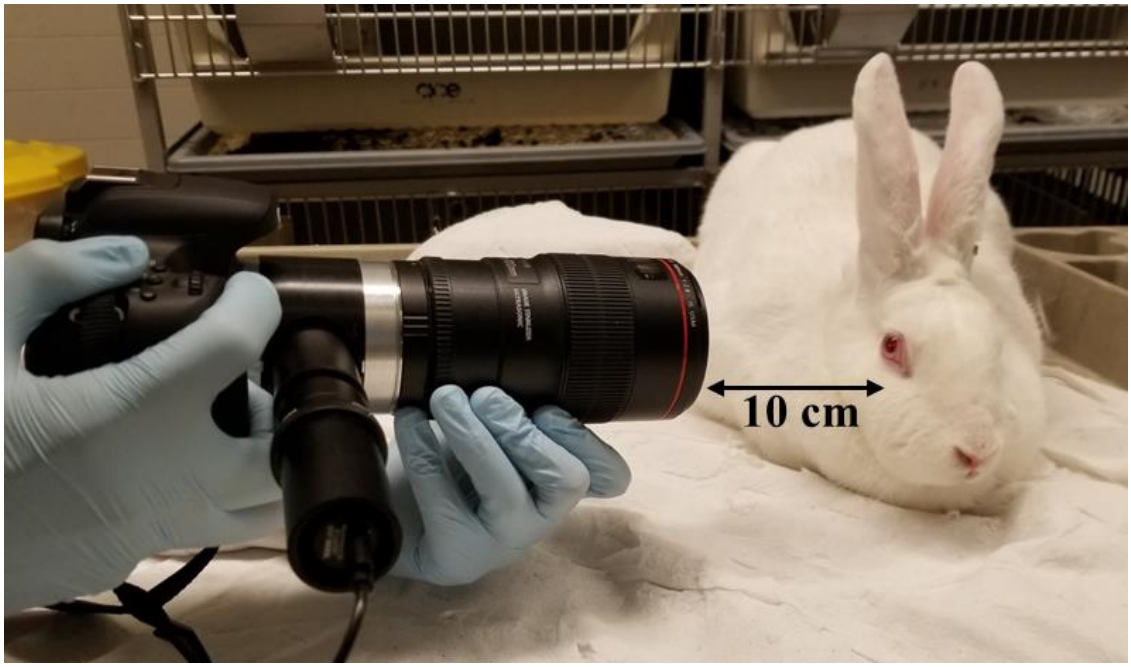

Figure 7.7: Photograph of DSLR optical reader.

Figure 7.8 shows appearance of interference fringes captured using the DSLR handheld reader. Images obtained from the measurement were processed and analyzed for IOP values the same way as before.

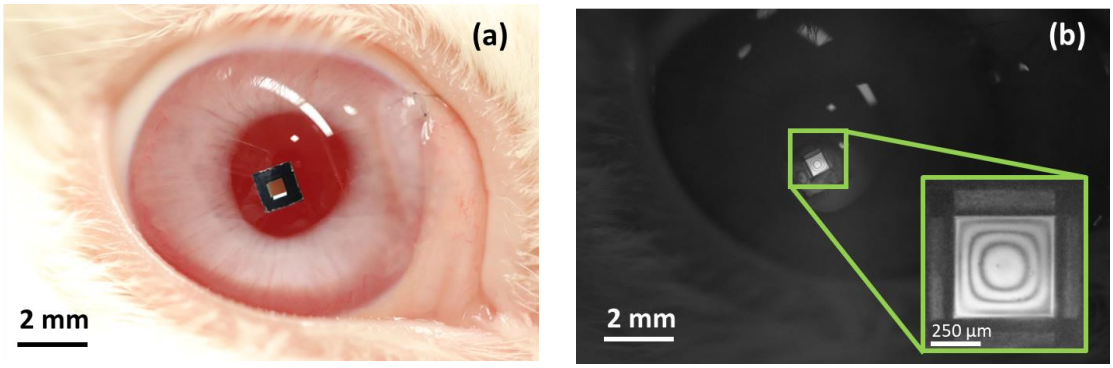

Figure 7.8: Photograph of implanted IOP sensor: (a) ambient light, (b) monochromatic light.

IOP measurement was also obtained using a rebound tonometer (iCare) for comparison. The tonometer was position upright, 10 mm away from the rabbit cornea. The rabbits were lightly restrained to minimize reading error due to movement. A photograph of the measurement procedure using the iCare tonometer is shown in Figure 7.9.

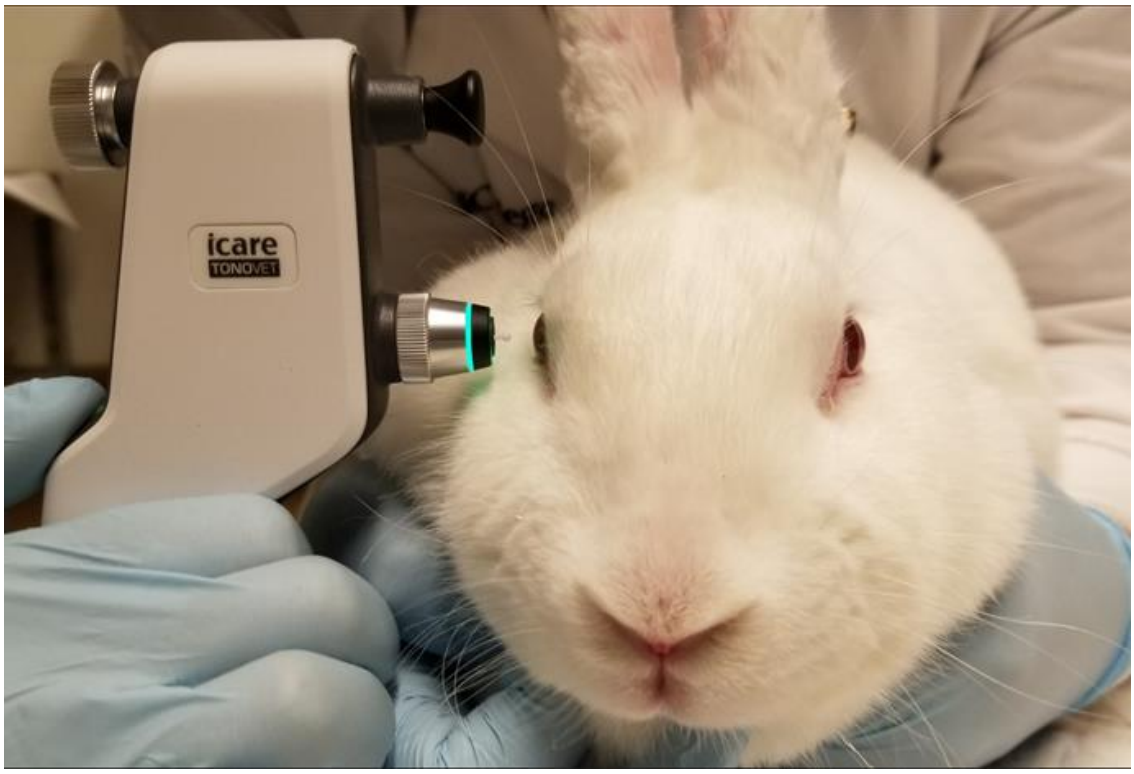

Figure 7.9: IOP measurement using iCare rebound tonometer.

7.2.5 Twelve Hour Study

We conducted a 12-hour experiment to compare the IOP measurements using the IOP implantable sensor and the rebound tonometer. In this experiment, IOP of the rabbit was measured every 1.5-hour using the DSLR reader and the iCare tonometer in random order. As shown in Figure 7.10, the measurements obtained from both devices were very consistent and could pick up the same spike in pressure. The pressure values from the iCare measurement were generally lower than the values from the implanted sensor. This is

expected as the rabbit cornea is thinner than that of a human and the tonometer did not account for this variation in corneal thickness.

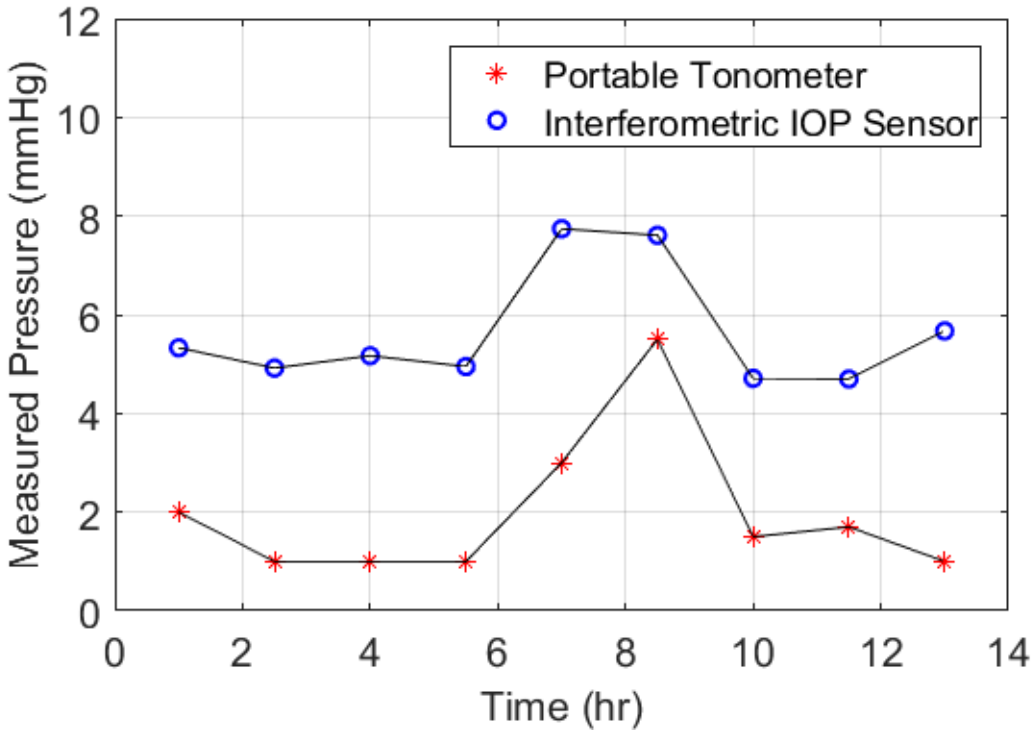

Figure 7.10: 12-hour in-vivo IOP measurements using interferometric IOP sensor and iCare tonometer.

7.2.6 10-day Study

Another experiment conducted in this first round of in vivo studies was to track the intraocular pressure profile over an extended period using the implanted IOP sensor. We used the DSLR reader to obtain one pressure measurement every day for ten days. The study was carried out at the end of the 10-week period. Therefore, we used the post-implantation calibration curve to calculate the pressure measurements. Figure 7.11. shows the IOP profile of the rabbit over ten days.

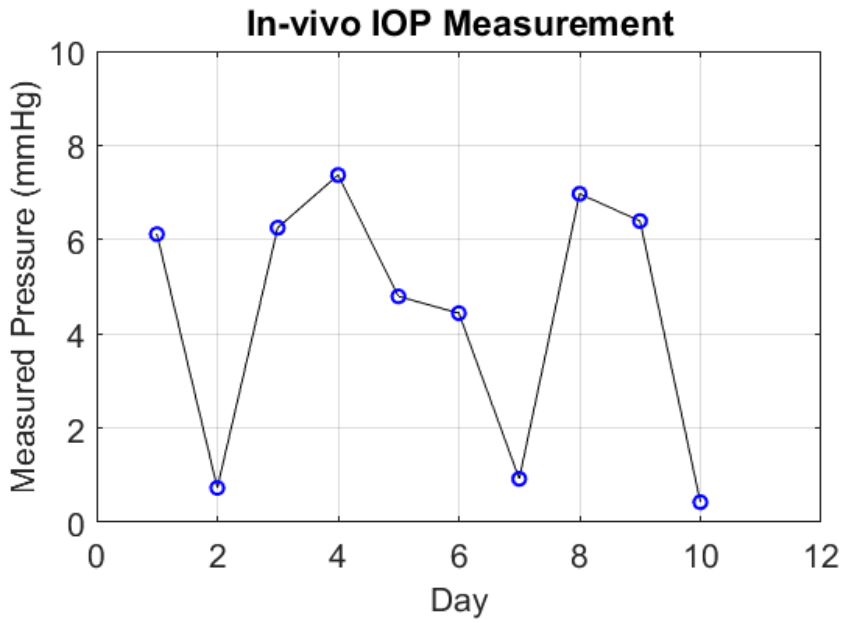

Figure 7.11: Intraocular pressure profile of the rabbit over a 10-day period obtained using the implanted IOP sensor.

7.2.7 Discussion

We have successfully implanted the IOP sensor unit into two rabbits via cataract surgery. The sensors were demonstrated to be biocompatible during the length of the study (10 weeks). IOP measurements obtained using two different optical readers were consistent with values obtained from the iCare tonometer.

The results indicate that measurements from the iCare tonometer underestimated the IOP in comparison to our implanted IOP sensor. Several research groups have also reported that the iCare tonometer and rebound tonometry in general tend to underestimate the true pressure value [163-164]. One possible cause for this difference is that the iCare tonometer was designed to be used in humans, whose corneal thickness and biomechanics are different than those of New Zealand white rabbits. Also, movement of the rabbits and

variations in angle of the probe relative to the corneal surface, distance between the tonometer and the cornea, or contact location on the cornea can all cause errors and variations in the pressure readings. Moreover, even though the iCare probe has a round plastic end cap to minimize the risk of injury to the cornea, repeated measurements may still cause irritation and damage to the cornea. For these reasons, the iCare tonometer is not ideal for frequent measurements of IOP.

Lobler, et al. [165] have conducted a thorough study on IOP measurement on New Zealand white rabbits using the iCare tonometer and proposed a correction factor for the underestimated measurements. The adjusted IOP values can be obtained by using the following linear equation:

$$IOP_{iCare} = 0.6972\, IOP_{actual} - 2.8222 \tag{7.1}$$

where IOP_{iCare} is the measurement from the tonometer and IOP_{actual} is the adjusted value. When we applied this correction for the results of the 12-hour study, the IOP measurements from the iCare tonometer and our IOP sensor agreed with each other very well as shown in Figure 7.12. The average difference of the twelve measurements was 1.2 mmHg. This demonstrates that our IOP sensor provides an alternative method to accurately measure eye pressure.

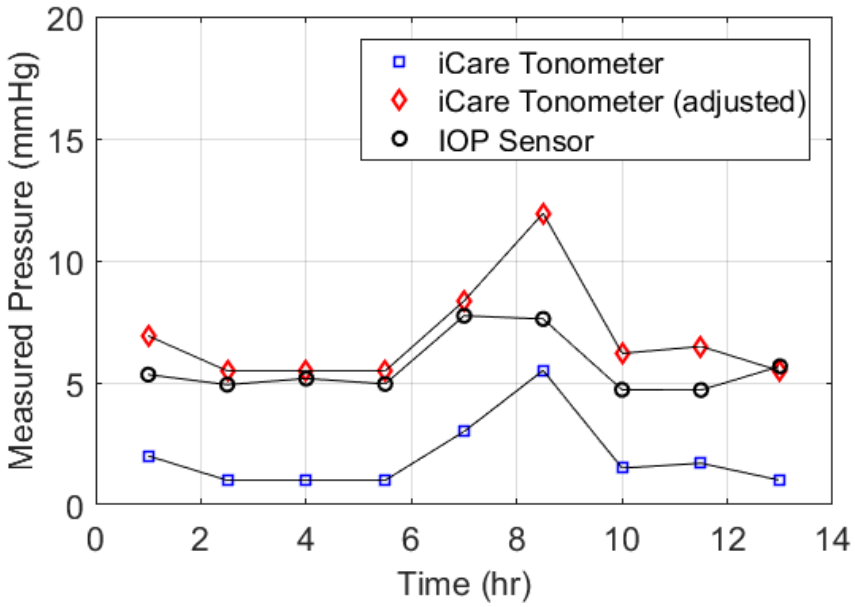

Figure 7.12: Comparison of pressure readings from IOP sensor and iCare tonometer after correction for iCare readings.

Our IOP sensor offers several advantages over tonometry, especially rebound tonometry. Since the sensor is implanted in the anterior chamber of the eye, we can obtain direct pressure measurement. The optical technique is independent of the corneal thickness and relatively insensitive to orientation of the reader. It also provides a long working distance (~10 cm), which reduces the risk of injuring the eye during measurement.

The pre-implantation and post-implantation calibration curves of the sensor indicate that the sensor exhibits a base line drift over time. Since the 12-hour experiment and the 10-day experiment were conducted toward the end of the 10-week study period, we used the post-calibration curve to calculate the IOP measurements in those experiments. In order to account for potential drifting during the life time of the sensor, we can obtain IOP measurements using one of the standard techniques periodically to recalibrate the IOP sensor.

In this round of our in vivo study, we compared the IOP measurements of the IOP sensor and the iCare tonometer in a 12-hour experiment and obtained an IOP profile for a 10-day period using the implantable sensor. It is important to have a long-term comparison study where IOP measurements are taken daily for an extended period using both methods to evaluate the performance of the IOP sensor. We have evaluated the biocompatibility of the implanted sensor through gross examination of the eye. A histology study is necessary to confirm that the implant does not cause any significant inflammation response from the eye.

7.3 Second Round of Implantation

The goals of the second round of in vivo study were to further evaluate the response of the IOP sensors and biocompatibility of the implant units. In this study, we used the circular sensor as opposed to the square ones in the last study. The footprint of the circular sensor was reduced to 0.8 mm^2, a 70% reduction in size comparing to the square sensor. This allowed us to integrate the IOP sensor into a foldable IOL and implanted the unit through a smaller corneal incision.

7.3.1 Intraocular Lens with Circular Sensor

In this round of in vivo study, we prepared two calibrated circular sensors and integrated each of them into soft foldable IOL (Alcon Toric). Figure 7.13 shows the steps of integrating the IOP sensor into the lens. First, we cut out a circular hole in the IOL using a puncher (Miltex Biopsy). The IOP sensors were then press fitted into the lens and fixed in place by friction between the two components.

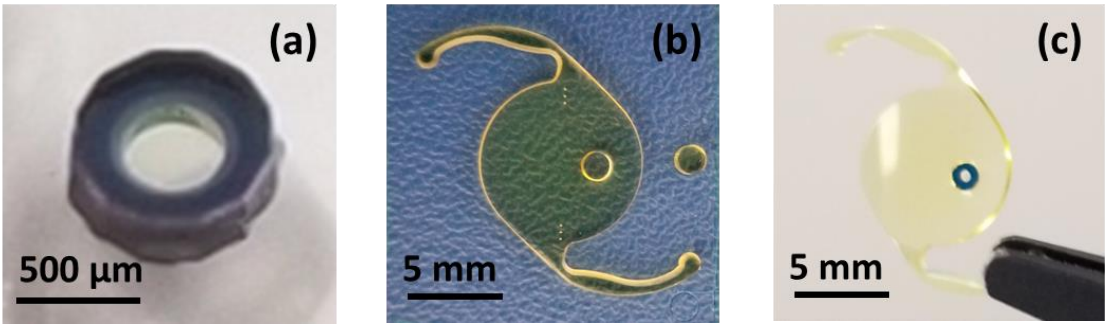

Figure 7.13: (a) Circular IOP sensor, (b) soft IOL with a circular cutout and (c) IOP sensor integrated to IOL.

One of the major advantages of using soft IOLs is that they can be rolled up, inserted in an injector and injected into the anterior chamber of the eye through a 3 mm corneal incision. It is important to verify that the IOL can still fit in the injector and be injected out after the IOP sensor is integrated. It is also crucial to test the response of the sensor to verify that there was no structure damage caused by the integration and implanting processes. We used the Monarch Delivery System (Alcon) to test out the injection process of the implant (Figure 7.14).

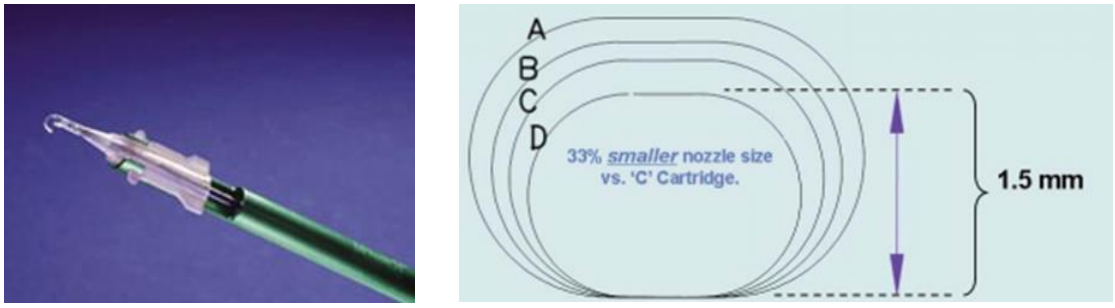

Figure 7.14: (a) Alcon Monarch II delivery system and (b) size comparison of Monarch cartridges: A – 3.2 mm, B – 3.0 mm, C – 2.8 mm and D – 2.2 mm [166].

The implant unit was successfully inserted and injected using a Monarch Cartridge C (2.8 mm). Once released into an aqueous solution, the lens unfolded back to the original configuration after a few minutes as shown in Figure 7.15. The sensor stayed in place

during the injection process and the pressure response was confirmed to be the same before and after the testing.



Figure 7.15: (a) IOL during injection, (b) IOL immediately after injection and (c) IOL 5 minutes after injection.

7.3.2 Long term study

In this long-term study, we compared daily pressure measurements obtained from the IOP sensor and the TonoVet rebound tonometer for a duration of 3 weeks. The rabbit was gently restrained during the measurement. It is important to make sure that the rabbit was calm while taking a pressure reading. Excessive movements from the rabbit can affect the quality of the rebound tonometer measurement as well as make the image of the fringe patterns blurry when using the DSLR reader.

The results of the long-term pressure measurement study indicated that the eye pressure of the rabbit remained stable during the study as shown in Figure 7.16.

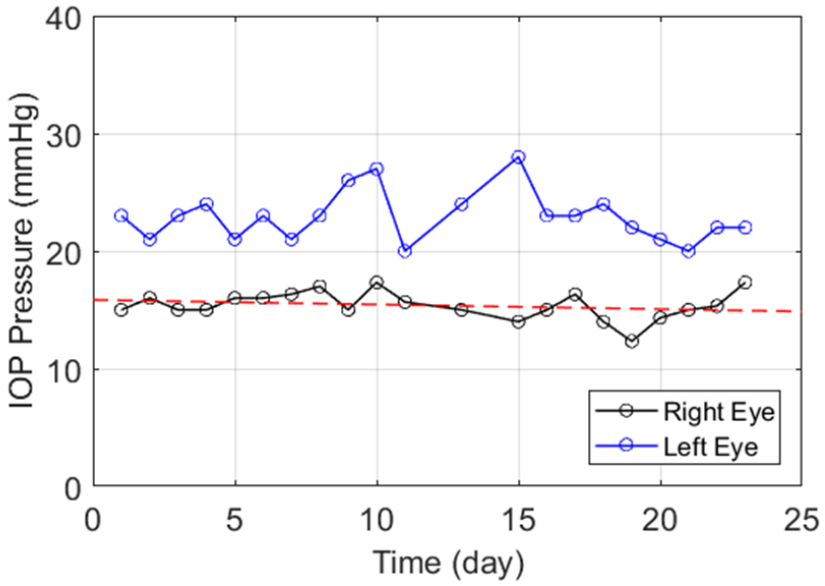

Figure 7.16: IOP of the left eye and right eye (implanted sensor) were monitor daily using the TonoVet for a duration of 23 days.

A linear fit through all pressure readings from the TonoVet indicates that the pressure of the right eye was stable around 15 mmHg. On the other hand, we observed that pressure readings from the IOP sensor indicated that the average deflection of the diaphragm increased linearly over time (Figure 7.17). This was most likely due to a baseline drift of the IOP sensor over the period of the study. In Figure 7.18, the drift corrected pressure readings from the IOP sensor were plotted in comparison with the TonoVet reading.

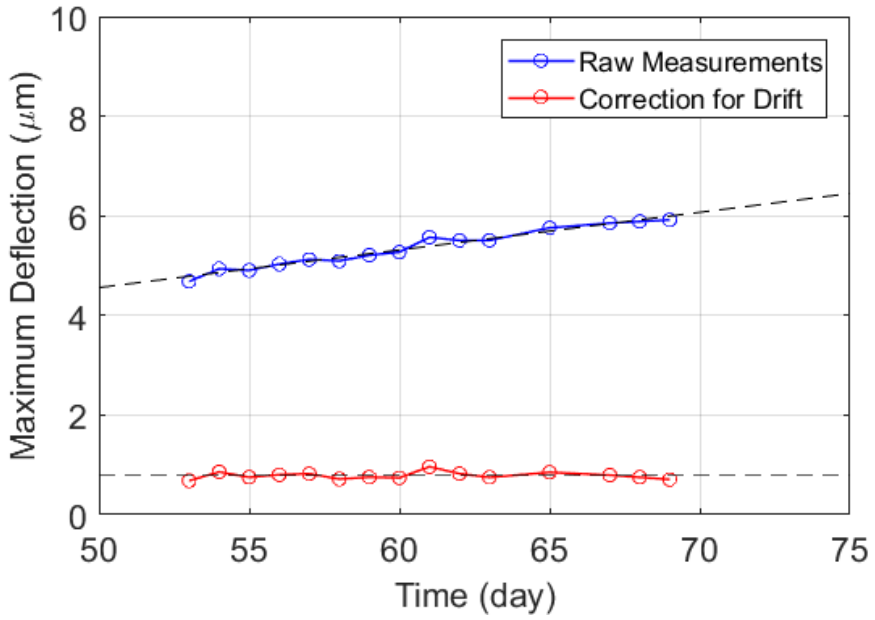

Figure 7.17: Average maximum deflection of the sensor increased linearly over time due to drift.

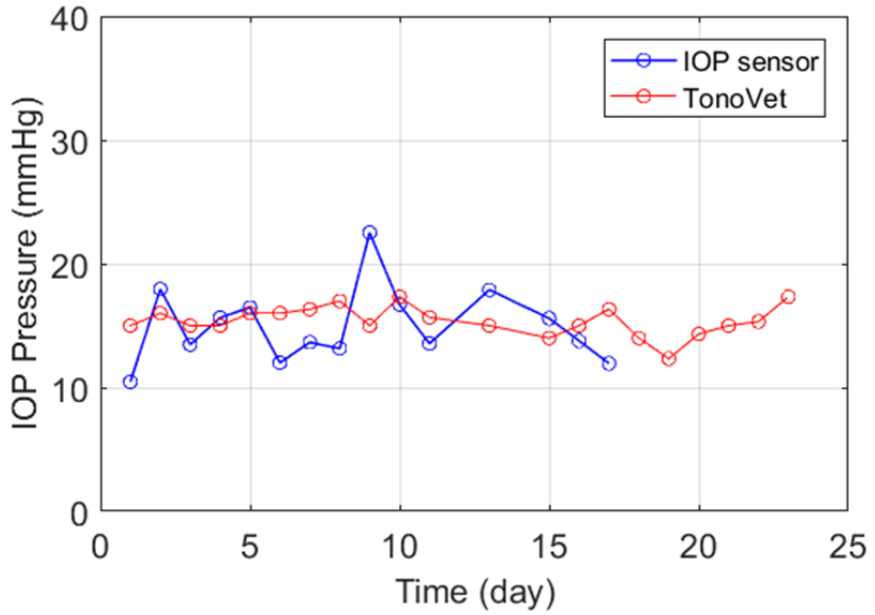

Figure 7.18: Comparison of the long-term pressure measurements using the IOP sensor and the TonoVet.

7.3.3 Transient study

Next, we conducted a transient study to demonstrate the ability of the IOP measurement system to measure eye pressure frequently in vivo and also the ability to measure large fluctuations in eye pressure, especially high eye pressure. High eye pressure was induced by injecting saline solution intravitreally into the eye of an anesthetized rabbit. There were two rounds of saline injections: 40 µL of saline solution at time t = 0 and 60 µL at time t = 45 minutes. The eye pressure of the rabbit was monitored using the DSLR handheld reader and the TonoVet rebound tonometer for a duration of one hour.

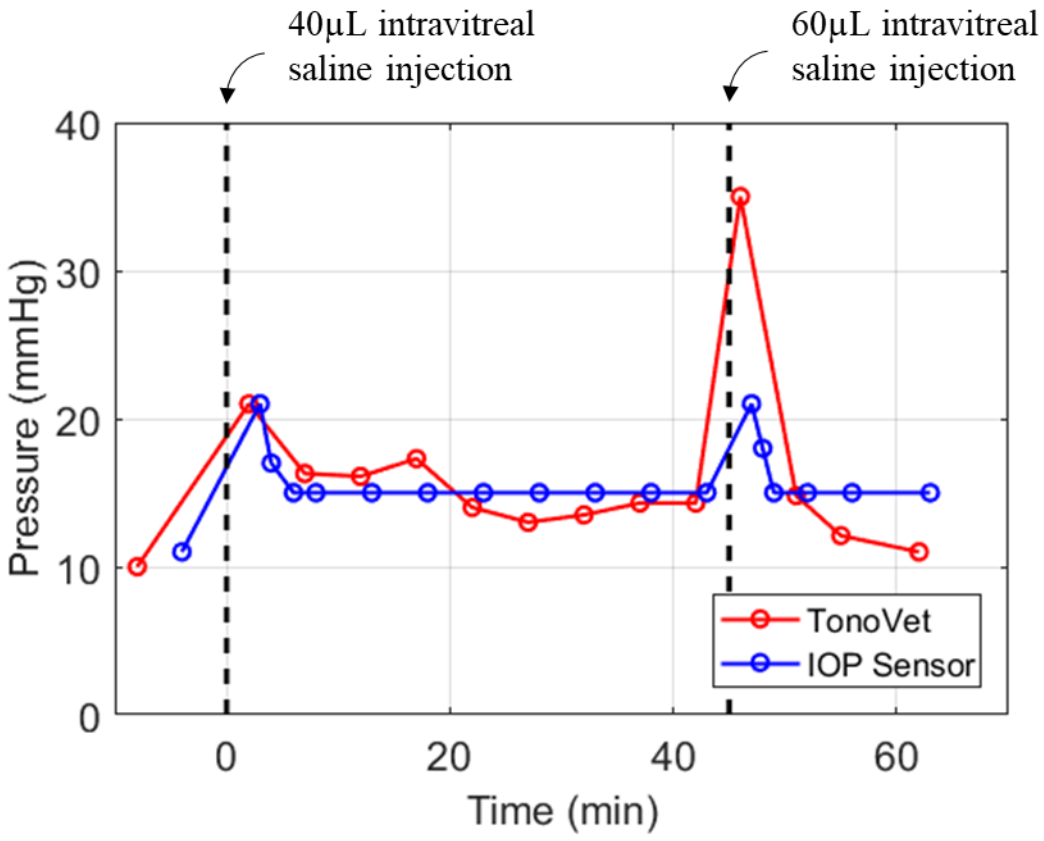

Figure 7.19: Induced artificial high pressure using intravitreal saline injection. Eye pressure monitored using the IOP measurement system and the TonoVet tonometer for a one-hour period.

Results for the transient study are shown in Figure 7.19. Immediately after the saline injection, the eye pressure increased to >20 mmHg. As the saline solution was being filtered out from the anterior chamber of the eye via the trabecular mesh, the eye pressure quickly dropped back down to the baseline pressure. The eye pressure increased sharply to >30 mmHg immediately after the second injection and dropped back down to baseline pressure within a few minutes. The trend obtained from both measurement devices agreed well with each other indicating that the IOP sensor can accurately capture transient changes of pressure in vivo.

7.3.4 Histology Study

To further demonstrate the biocompatibility of the IOP sensor, we performed a histology assessment at the end of the in vivo study. First, the implanted unit (IOP sensor and IOL) was carefully removed from the eye of the rabbit for post-implantation analysis. The whole eye ball was then excised and immediately submerged in 1% formaldehyde and 1.5% glutaraldehyde solution for fixing after euthanasia. After a 2-day fixing period, the eye ball was rinsed with 70% isopropanol and stained for imaging purposes. We performed a standard H&E staining procedure and sectioned the sample for imaging analysis.

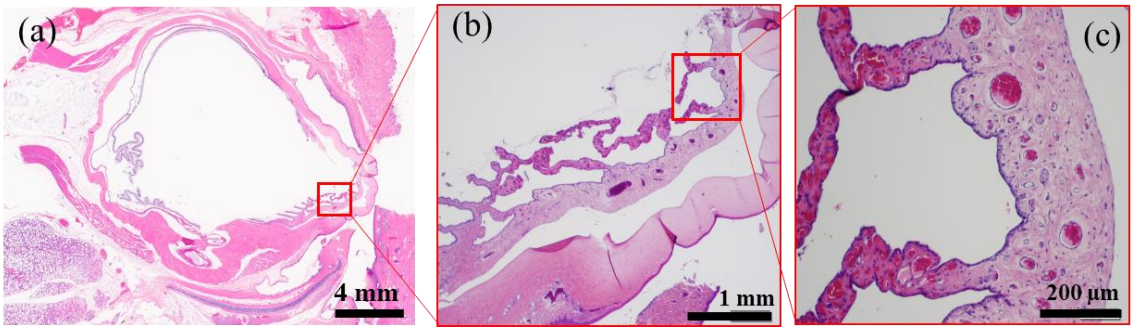

Figure 7.20: Images of the H&E staining of the rabbit eye post-implantation: (a) whole globe and (b-c) ciliary apparatus including the ciliary processes and the iris.

The results from the histology (Figure 7.20) showed normal ciliary apparatus (ciliary processes and iris), with no signs of inflammation. The H&E slides of the eye ball indicated that the ocular tissue of the rabbit eye was microscopically normal, with no evidence for reaction to the lens or the IOP sensors.

7.3.5 Discussion

Most of the current IOLs used in cataract surgeries are foldable lenses. The smaller form factor of the implant allows smaller incision size. This allows the cornea tissue to heal faster and reduces the risk of inflammation and infection. Therefore, integrating the IOP sensor into foldable IOLs makes the implantation procedure easier in practice.

The long-term study indicated that there was a base line drift. All pressure sensors are susceptible to some degree to baseline drift over the life of the sensor. Two of the common sources of drifting are that the sensors undergo expansion and contraction during pressure and temperature cycling, and that materials change their dimensions due to environmental changes. Magnitude of the baseline drift depends heavily on the environment of the sensor. The baseline drift and long-term stability for a pressure sensor

can be predicted through pre-implantation testings and calibrations. However, these tests are often conducted in a well-controlled environment which can lead to inaccurate predictions of the actual in vivo drift response. In the application of an implantable IOP sensor, the baseline drift can be corrected through calibration using a standard tonometry device, e.g., a Goldman tonometer. Depend on the magnitude of drift, we can adjust the interval of re-calibration. We envision the IOP sensor to be re-calibrated once or twice a year during annual office visits.

One of the potential reasons for the rapid baseline drift that was observed in the long-term in vivo study was that the SiN diaphragm erodes and becomes thinner over time. In that situation, the SiN diaphragm would deflect more for the same pressure at the end of the study compared to at the beginning of the study. Maloney, et al. [167] concluded that the in vivo diaphragm removal rate can be as much as 0.33 nm/day for LPCVD silicon nitride and 2.0 nm/day for PECVD silicon nitride. Using the analytical model for the deflection of a diaphragm together with our long-term study results, we can estimate that the SiN diaphragm would have been getting thinner at a rate of 1 nm/day.

In the transient study, intravitreal injection of saline solution into the posterior chamber of the eye was selected as a method to induce elevated eye pressure. In a healthy eye, IOP is well regulated by balancing the production of aqueous fluid from the ciliary body and the drainage of fluid through the trabecular mesh. After the saline injection, the pressure gradient across the trabecular mesh regulates the outflow process which reduces the pressure in the eye. This process occurs quickly, and the baseline pressure is re-established within seconds to minutes. A truly continuous IOP measurement system is necessary to capture the full profile of this type of transient changes in pressure.

Currently, commercially available techniques for measuring IOP are not suitable for frequent measurements. A Goldman tonometer is only available for clinical use. Portable rebound tonometers, e.g., iCare tonometers, are not suitable for frequent measurement because of risks of corneal damage from repeated contacts with the probe. The results from the transient study demonstrated that the IOP sensor performed very well over a large physiological pressure range, and that our IOP measurement system is capable of obtaining frequent IOP measurements without the risk of corneal damage.

7.4 Summary

In this chapter, we introduced and discussed two rounds of in vivo studies of the IOP sensor using rabbits. Eye pressure measurements were obtained using the DSLR reader and a rebound tonometer (iCare and TonoVet). The studies demonstrated the feasibility of implanting the IOP sensor through convention cataract surgery and the capability of the IOP measurement system to accurately capture changes in eye pressure over an extended period. The IOP sensor can be calibrated periodically based on pressure values obtained using traditional method to correct for baseline drifting in long term use. Histology study indicated that the IOP sensor did not have any significant immune response in the eye. This result shows that the implant was well tolerated by the eye and that the sensor was biocompatible in the eye environment for the duration of the study (12 weeks).

Chapter 7, in part is a reprint of the material as it appears in "A Wireless Handheld Pressure Measurement System for in vivo Monitoring of Intraocular Pressure in Rabbits," Phan, Alex, Phuong Truong, Andrew Camp, Kerrianne Stewart, Benjamin Suen, Robert

N. Weinreb, and Frank E. Talke, *In Preparation for Publication*. The dissertation author was the primary investigator and author of this paper.

Chapter 8

Image Processing

In this chapter, we discuss about different image processing algorithms that were developed throughout the project to analyze the fringe patterns and determine the intraocular pressure. This is a critical component to evaluate the accuracy and reliability of the measurement system.

8.1 Image Correlation

To calculate the pressure from a captured image, we first created a database of interference images corresponding to known pressure loads from 0 to 60 mmHg at 0.2 mmHg interval. Thereafter, images of interference patterns from unknown pressures were compared with the database images. By determining where the highest correlation occurred, we were able to find the applied pressure at which the image was taken.

Correlation coefficient r between captured images and the database images were calculated using:

$$r = \frac{\sum_i (A_i - \overline{A})(B_i - \overline{B})}{\sqrt{\sum_i (A_i - \overline{A})^2}\sqrt{\sum_i (B_i - \overline{B})^2}} \tag{8.1}$$

In Equation **(**8.1**)**, A_i and B_i are the intensities of the ith pixel whereas $\bar{A}$ and $\bar{B}$ are the mean pixel intensity of images A and B, respectively.

Figure 8.1 shows typical correlation results of test images with the reference database taken at five different pressures. Pressure values of the database images are

represented on the x-axis and correlation coefficients are plotted on the y-axis. From Figure 5, it is clear that the test images taken at 10, 20, 30, 40 and 50 mmHg have the strongest correlation (r~1) with the reference images corresponding to 10, 20, 30, 40 and 50 mmHg pressure loads, respectively. When compared with the rest of the database, the test images have low correlation ($r < 0.4$). In a control testing environment, this method can reliably provide a pressure measurement with an accuracy of approximately $\pm$ 0.5 mmHg.

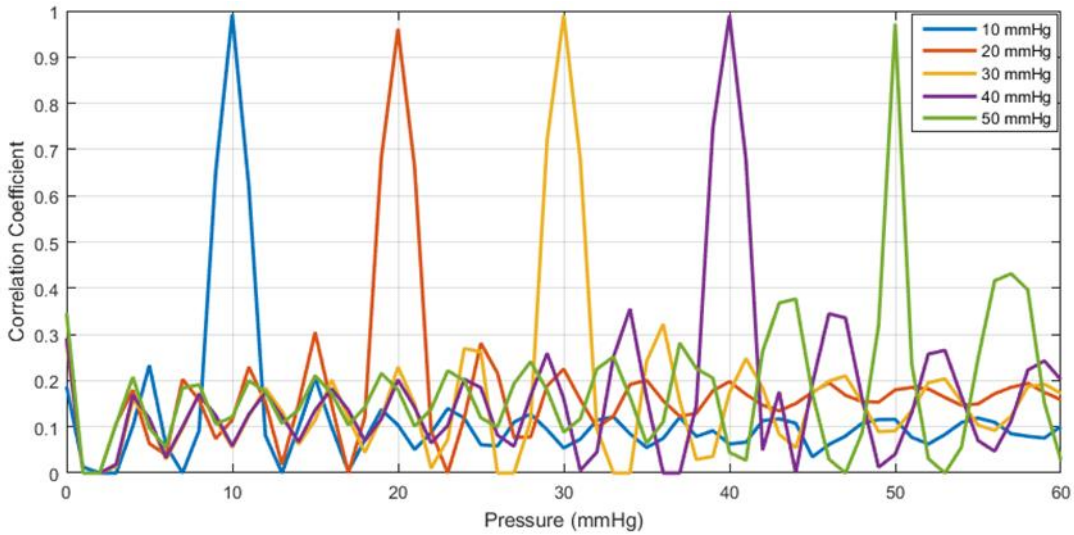

Figure 8.1: Correlation of interference patterns with the database for five different pressure loads from 10 to 50 mmHg.

Performing image processing using the correlation approach as shown here provides a quick way to analyze the fringe patterns. However, this method requires the image to be in the exact orientation of the calibration images. Any misalignment would lead to inaccurate calculation, especially when there are many fringes and they appear close to one another.

8.2 Power Spectrum Analysis

Another approach used to analyze the captured image to determine the IOP pressure was the power spectrum method. In this approach a combination of ImageJ and MATLAB were used for the analysis of the fringe patterns. The procedure begins with cropping the region of interest (the membrane region of the sensor) in ImageJ. Next, the cropped images were converted into binary images and imported into MATLAB for analysis. By converting the fringe pattern into a binary image, we minimized the effect of ambient light due to different testing conditions. Finally, a two-dimensional discrete Fourier transform, and calculation of mean pixel intensity of the corresponding power spectrum was performed on each image.

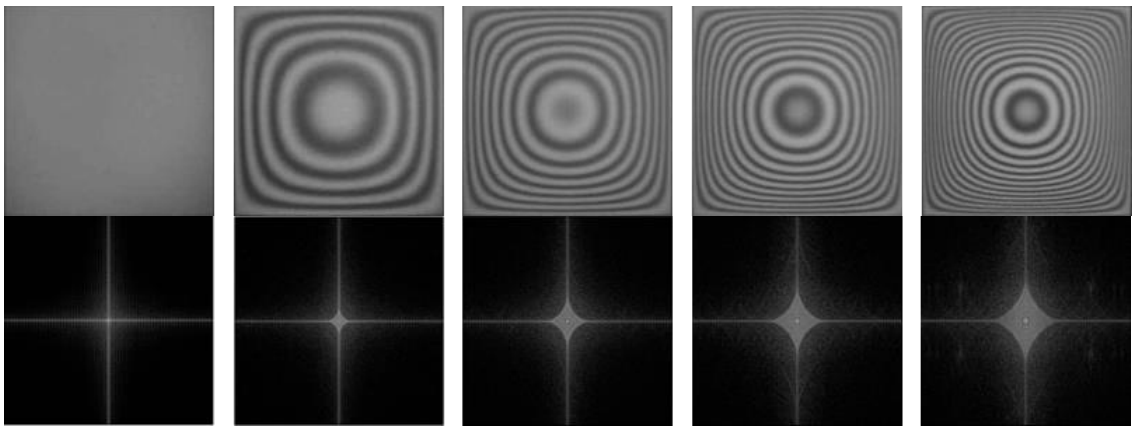

Figure 8.2: Interference patterns at different pressure loads and their corresponding power spectrum plots.

Figure 8.2 shows an example of an average pixel intensity as a function of pressure. As the pressure increases, the number of fringes increases. This translates to the presence higher frequency components and leads to higher average pixel intensity of the power spectrum plot.

We were able to improve the image processing algorithm by transforming the fringe patterns into the frequency domain and analyze their corresponding power spectrums. This method relaxes the constraint on the orientation of the images. Though this image processing approach would work well in many situations, the average pixel intensity of the power spectrum is not unique to a fringe pattern, which is unique to a given pressure load. In other words, prone to error.

Also, it can be noted from Figure 8.3 that there are two regions where the analysis is prone to error: patterns that have less than 2 fringes (lower pressure) and patterns that have more than 10 fringes (higher pressure). This can potentially become worse if the images of the fringe patterns are not taken in idea conditions, e.g., blurry image, uneven lighting, presence of particles or cells on the surface of the diaphragm. For example, the interference fringes can appear fuzzy due to movement during capturing the image. When the image is transformed into the frequency domain, it would lose some of the higher frequency components compare to a sharp image with the same number of fringes. This would lead to lower average pixel intensity and ultimately lower pressure reading.

It is desired to develop an image processing algorithm that is capable of analysis under different lighting conditions, motion induced noise, and orientation of the captured image.

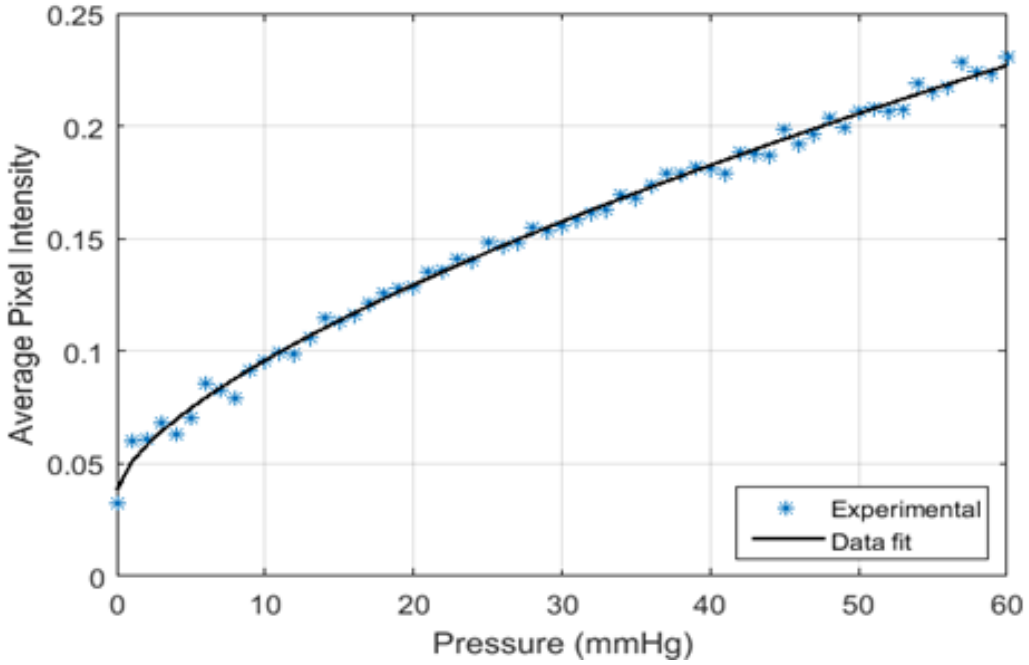

Figure 8.3: Average pixel intensity of the power spectrum of the fringe patterns as a function of applied pressure from 0-60 mmHg (1 mmHg step size).

8.3 Diaphragm Deflection Mapping

To overcome the challenges that we encountered in the previous methods of image processing, we developed another approach that relate the number fringes to the physical deflection of the diaphragm and from there determine the pressure load. As introduced in Chapter 2, the deflection of the diaphragm is unique to the pressure load and the fringe pattern is a function of the deflection profile. The idea is to first determine the maximum deflection value (at the center of the diaphragm) from a given fringe patterns using the phase equation (Equation 2.1) and then compare this value with a calibration curve to determine the pressure value.

Figure 8.4 illustrates the main image processing steps of this approach. We need to construct a calibration curve similar to the other approaches. Fringe patterns captured at known pressure loads were first analyzed in MATLAB to determine the locations of the maximum and minimum intensities, i.e., locations of the peaks and troughs. According to the phase equation, the path difference between a bright and a dark fringe is a quarter of a wavelength and between two consecutive bright fringes is a half of a wavelength. Applying this relationship with the XY-locations of the fringes, we can reconstruct the deflection profile of the diaphragm along any given cross section and determined the maximum deflection value at the center of the diaphragm. Once we have obtained all the deflection values associated with each of the pressure load, a third order polynomial curve fit was performed on the data to produce the calibration curve. We can define the sensitivity of the sensor to be the ratio of the highest deflection to highest pressure load.

Since the maximum deflection of the diaphragm can be determined from any cross section of the image, we only need to use a portion of the image. Variations in visibility of the fringes due to lighting do not change the locations of the bright and dark fringes and hence, do not affect the pressure calculation. Also, the relative distances between peaks and troughs remain relatively the same regardless if the image is blurry or not. This is a major advantage of this approach since many of our images capture in vivo have a high level of noise due to movement of the rabbits (blurry images).

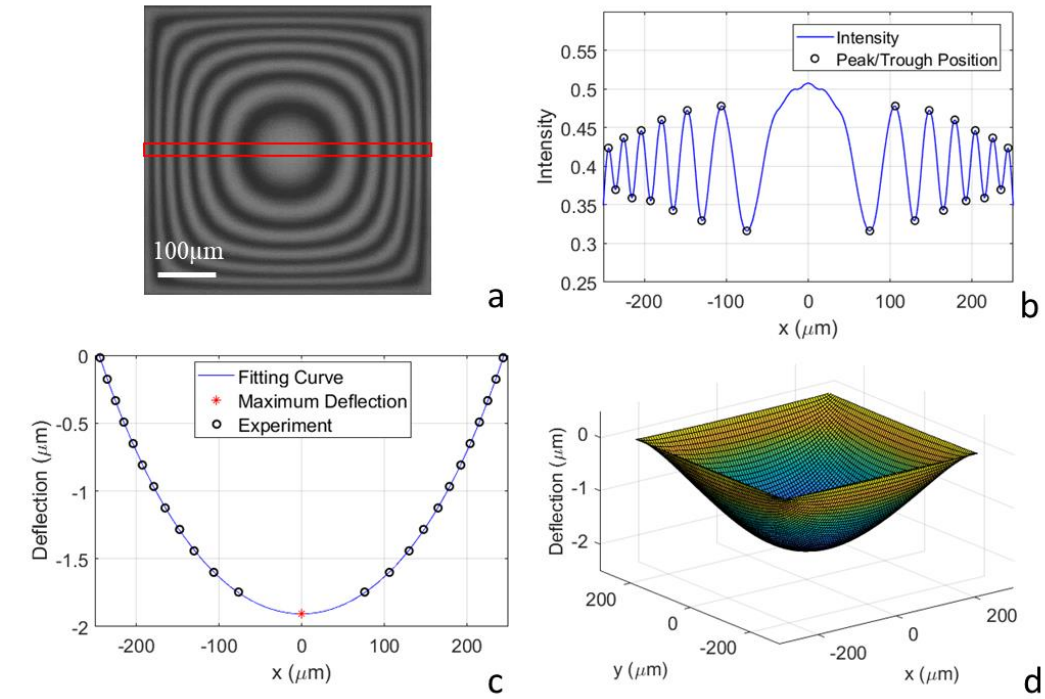

Figure 8.4: Image processing approach using diaphragm deflection: (a) isolate a cross section of the fringe pattern, (b) determine the locations of peaks and troughs, (c) map the deflection of the diaphragm along the cross section and (d) 3D reconstruction of the deflection profile of the diaphragm.

8.4 Summary

In this chapter, we introduced three different image processing approach to analyze fringe patterns. Image correlation and power spectrum analysis are simple and work well for ideal conditions. However, these two approaches suffer from effects of lighting, blurriness, and other aberrations. The last approach using diaphragm defection mapping was shown to be a much for robust technique. The implementation is more challenging; however, the algorithm can handle subpar images taken from non-ideal conditions very well and produce highly accurate results.

Chapter 9

Conclusion and Future Direction

9.1 Conclusion

In this dissertation, a proposed optical method to measuring direct intraocular pressure was studied. The motivation of the study was driven by the need to obtain frequent or semi continuous measurements of intraocular pressure to fully capture the fluctuating nature of intraocular pressure in patients with glaucoma.

First, the sensor was designed, modeled, fabricated and characterized. The design of the sensor considered parameters such as passive, sub millimeter in size, biocompatible, and implantable. From these design parameters, an interferometric approach was proposed, and the sensor was modeled to validate how well the approach fits the design constraints. Once validated, the sensor was fabricated using MEMs techniques, and characterized using in vitro bench top testing to obtain interferometric images that could be analyzed using image processing. Post processing calculations correlated interferometric images with diaphragm deflection and diaphragm deflection with pressure. Each sensor was calibrated and characterized within the physiological relevant range of 0 to 60 mmHg display high repeatability and sensitivity.

The effects of temperature, incident angle, and substrate coating thickness were evaluated due to their effect on sensor readout capability. Temperature effects show that low temperature creates artificially high-pressure readings, and high temperatures cause

the volume to increase leading to lowered sensitivity and low-pressure readings. The effects of temperature can be accounted for in computing the pressure values by isolating the offset and subtracting from the measured value. Incident angle experiment evaluated the limitations and impact of incident angle on the sensor readout. It was shown that the angle in which a reading can still be obtained is within +/- 6 degrees. Substrate coating thickness was used to determine the most optimal coating to obtain the highest fringe contrast and visibility. Several coating thicknesses were compared and found that 79 nm coating thickness yielded the highest visibility and contrast.

A handheld reader was developed in order to enable experiments to move away from benchtop testing. Several generations of the handheld reader were developed, each with new features and characteristics that enabled wireless, optical, and portable pressure measurements. The first generation very closely represented that of the benchtop testing and contained a microscope objective, CCD camera, and beam splitter. However, it was found that the stability, focus, and field of view were major concerns as to how feasible measurements can be taken. The second-generation reader incorporated a DSLR camera which enabled more stability, autofocusing, and a larger field of view making the process of taking measurements faster and easier. The third-generation reader incorporated a mobile device to truly enable patients to take pressure measurements at the convenience of their home (patient point of care). A mobile app was created to enable real time analysis and provide a pressure reading once the image has been captured.

Ex vivo studies were conducted using whole rabbit eye. Various device carriers such as an intraocular lens and capsular tension ring were experimented to determine the best implantation procedure. Initial ex vivo studies showed promising results with sensors

anchored to the intraocular lens. Ex vivo studies with sensor anchored to the capsular tension ring faced many challenges due to the limited range of the incident angle. Sensor response showed repeatability and sensitivity to changes in pressure, demonstrating strong capabilities for measuring intraocular pressure accurately and consistently.

In vivo studies were conducted using two New Zealand white rabbits to validate the implant feasibility of the sensor and provide a qualitative assessment on biocompatibility. Cataract surgery was performed to insert the intraocular lens with the attached sensor. The sensors were implanted for a period of 10 weeks. Promising results were obtained showing good correlation between the iCare tonometer and the intraocular pressure sensor. Visual assessment of biocompatibility showed no signs of infection, rejection, or toxicity surrounding the sensor.

Finally, image processing algorithms were developed and improved throughout the entirety of the dissertation as it is a critical step in converting optical images to pressure values. A custom fringe analysis algorithm processes the images by determining the fringe peaks and correlating the peaks with a diaphragm deflection profile. The diaphragm deflection is characterized and correlated with pressure output.

The IOP measurement system presented in this research offers a non-contact approach to monitor eye pressure. This eliminates the risks of transmitting infectious disease from one patient to other via the measurement device, e.g., the tip of the tonometer. Moreover, it also eliminates the risks of damaging the cornea when obtain measurement frequently that are present when using the air-puff tonometer or rebound tonometer.

9.2 Future Direction

Future directions of this project include further validating the sensor through large scale animal studies, addressing other patient demographics that may need pressure measurements, visual impairment tests, and exploring other surgical techniques.

The large-scale animal studies are necessary in order to create a statistically significant data pool to assess the sensor's consistency and repeatability across many specimens. The large-scale study should include a control and at the minimum of twelve rabbits in order to generate significant results. The large number of specimens will enable further biocompatible evaluations using histological analysis and long-term testing of the device.

Visual obstruction tests are necessary to determine the optimal location of the device. These tests are necessary to determine how the sensor obstructs vision in patients when placed in different locations of the intraocular lens. It has been a challenge to determine the most optimal location, as it has been a question of debate whether placing such a small sensor on the optical axis will obstruct or impair vision.

Other surgical techniques would also need to be determined in the future in order to impact a larger population beyond cataract patients. Surgical techniques can include using an iris claw or pin to anchor the sensor onto the iris. Another potential carrier for the sensor could also be the Boston Keratoprosthesis as patients with total corneal transplantation surgery cannot monitor their eye pressure. Integrating the sensor onto the front plate can enable direct measurements of pressure, and with better treatment, can prevent vision loss for those patients.

Overall, the field of implantable pressure sensor will continue to expand as the field of MEMS and NEMS technology continues to grow. With the population of glaucoma patients increasing over time, the need for direct, reliable pressure measurements are needed more than ever both in a laboratory setting for drug screening and discovery, as well as more informed treatment plans in clinic. The ability to track eye pressure over time would lead to a disruptive and transformative change in ophthalmology and in the scientific understanding of glaucoma.

References

[1] "What Is Glaucoma?" Ocular Blood Flow and Glaucomatous Optic Neuropathy, 2009, pp. 27–34., doi:10.1007/978-3-540-69443-4_3.

[2] Girkin, Chris. "Glaucoma: Science and Practice." Journal of Glaucoma, vol. 13, no. 1, 2004, p. 84., doi:10.1097/00061198-200402000-00016.

[3] Blumenthal, Eytan Z. "Glaucoma." Journal of Glaucoma, vol. 14, no. 3, 2005, p. 252., doi:10.1097/01.ijg.0000159133.46451.07.

[4] Broman, Aimee Teo, et al. "Estimating the Rate of Progressive Visual Field Damage in Those with Open-Angle Glaucoma, from Cross-Sectional Data." Investigative Ophthalmology & Visual Science, The Association for Research in Vision and Ophthalmology, 1 Jan. 2008, iovs.arvojournals.org/article.aspx?articleid=2125590.

[5] Harry, Quigley. "Open-Angle Glaucoma ." New England Journal of Medicine, Oxford University Press, 10.1056/NEJM199304153281507.

[6] Sommer, Alfred. "Glaucoma Risk Factors Observed in the Baltimore Eye Survey." Current Opinion in Ophthalmology, vol. 7, no. 2, 1 Apr. 1996, pp. 93–98., doi:10.1097/00055735-199604000-00016.

[7] Boland, M. V., & Quigley, H. A. (2007). Risk factors and open-angle glaucoma: Classification and application. Journal of Glaucoma, 16(4), 406-418., doi: 10.1097/IJG.0b013e31806540a1

[8] He, Mingguang. "Angle-Closure Glaucoma: Risk Factors." Pearls of Glaucoma Management, 2009, pp. 415–419., doi:10.1007/978-3-540-68240-0_54.

[9] Wilson, M. Roy, and Mark Gallardo. "Glaucoma Risk Factors: Ethnicity and Glaucoma." The Glaucoma Book, 2010, pp. 101–109., doi:10.1007/978-0-387-76700-0_10.

[10] Loewen, Nils A., and Angelo P. Tanna. "Glaucoma Risk Factors: Intraocular Pressure." Clinical Glaucoma Care, 2013, pp. 1–22., doi:10.1007/978-1-4614-4172-4_1.

[11] Brunner, Thomas. "Curing Glaucoma: A Video Message from the President." Glaucoma Research Foundation, www.glaucoma.org/about/curing-glaucoma-a-video-message-from-the-president.php.

[12] Tham, Yih-Chung, et al. “Global Prevalence of Glaucoma and Projections of Glaucoma Burden through 2040.” Ophthalmology, vol. 121, no. 11, 2014, pp. 2081–2090., doi:10.1016/j.ophtha.2014.05.013.

[13] “Glaucoma Facts and Stats.” Glaucoma Research Foundation, www.glaucoma.org/glaucoma/glaucoma-facts-and-stats.php.

[14] Fellman, Ronald. “Blindness and Glaucoma: Comparison of Patient Conditions Progressing to Blindness From Glaucoma With Patients Maintaining Vision.” Evidence-Based Eye Care, vol. 4, no. 1, 2003, pp. 14–15., doi:10.1097/00132578-200301000-00006.

[15] Malihi, Mehrdad, et al. “Long-Term Trends in Glaucoma-Related Blindness in Olmsted County, Minnesota.” Ophthalmology, vol. 121, no. 1, 2014, pp. 134–141., doi:10.1016/j.ophtha.2013.09.003.

[16] Quigley, H. A. “Glaucoma in China (and Worldwide): Changes in Established Thinking Will Decrease Preventable Blindness.” British Journal of Ophthalmology, vol. 85, no. 11, 2001, pp. 1271–1272., doi:10.1136/bjo.85.11.1271.

[17] Bourne, Rupert R. A., et al. “Number of People Blind or Visually Impaired by Glaucoma Worldwide and in World Regions 1990 – 2010: A Meta-Analysis.” Plos One, vol. 11, no. 10, 2016, doi:10.1371/journal.pone.0162229.

[18] Quigley, H A. “The Number of People with Glaucoma Worldwide in 2010 and 2020.” British Journal of Ophthalmology, vol. 90, no. 3, 2006, pp. 262–267., doi:10.1136/bjo.2005.081224.

[19] Bleau, Anne-Marie, et al. “Managing Intraocular Pressure: Innovation in Glaucoma Management.” Glaucoma - Intraocular Pressure and Aqueous Dynamics, 2016, doi:10.5772/65972.

[20] Jonas, Jost B., et al. “Intraocular Pressure and Associated Factors.” Journal of Glaucoma, vol. 20, no. 7, 2011, pp. 405–409., doi:10.1097/ijg.0b013e3181f7af9b.

[21] Prum, Bruce E. “Normal Pressure Glaucoma.” The Glaucoma Book, 2010, pp. 421–459., doi:10.1007/978-0-387-76700-0_35.

[22] Bengtsson, Boel, et al. “Fluctuation of Intraocular Pressure and Glaucoma Progression in the Early Manifest Glaucoma Trial.” Ophthalmology, vol. 114, no. 2, 2007, pp. 205–209., doi:10.1016/j.ophtha.2006.07.060.

[23] Prabhudesai, Medha. “Chapter-03 Importance of Optic Nerve Head Evaluation in Glaucoma.” Atlas of Optic Nerve Head Evaluation in Glaucoma, 2006, pp. 19–22., doi:10.5005/jp/books/10069_3.

[24] Marjanovic, Ivan. “The Optic Nerve in Glaucoma.” The Mystery of Glaucoma, 2011, doi:10.5772/19811.

[25] Burgoyne, Claude F. “Optic Nerve: The Glaucomatous Optic Nerve.” Pearls of Glaucoma Management, 2009, pp. 1–13., doi:10.1007/978-3-540-68240-0_1.

[26] Morgan, J. E. “Retinal Ganglion Cell Shrinkage in Glaucoma.” Journal of Glaucoma, vol. 11, no. 4, 2002, pp. 365–370., doi:10.1097/00061198-200208000-00015.

[27] Budak, Yasemin, and Muberra Akdog. “Retinal Ganglion Cell Death.” Glaucoma - Basic and Clinical Concepts, 2011, doi:10.5772/19003.

[28] Toris, Carol B. “Aqueous Humor Dynamics and Intraocular Pressure Elevation.” Glaucoma, 2015, pp. 47–56., doi:10.1016/b978-0-7020-5193-7.00006-6.

[29] Tan, James C.h., et al. “Changes in Aqueous Humor Dynamics with Age and Glaucoma.” Ophthalmology Research™ Mechanisms of the Glaucomas, pp. 311–327., doi:10.1007/978-1-59745-373-8_19.

[30] Reddy, Gr. “Chapter-05 Visual Field Loss in Glaucoma.” Practical Guide to Interpret Visual Fields, 2010, pp. 137–320., doi:10.5005/jp/books/11111_5.

[31] Heijl, A., and B. Bengtsson. “Early Visual Field Defects in Glaucoma: A Study of Eyes Developing Field Loss.” Glaucoma: Decision Making in Therapy, 1996, pp. 75–78., doi:10.1007/978-88-470-2196-9_12.

[32] Simmons, Steven T. “Visual Field Progression in Patients with Initially Unilateral Visual Field Loss from Chronic Open-Angle Glaucoma.” Evidence-Based Eye Care, vol. 2, no. 2, 2001, pp. 110–111., doi:10.1097/00132578-200104000-00023.

[33] Tanito, Masaki, et al. “Different Glaucoma Types and Glaucoma Surgeries among Different Age Groups.” Graefe's Archive for Clinical and Experimental Ophthalmology, 2018, doi:10.1007/s00417-018-4058-x.

[34] “What Are the Types of Glaucoma?” Johns Hopkins Medicine Health Library, www.hopkinsmedicine.org/wilmer/services/glaucoma/book/chapter_types_of_glaucoma.html.

[35] Weinreb, Robert N., et al. “The Pathophysiology and Treatment of Glaucoma.” *Jama*, vol. 311, no. 18, 2014, p. 1901., doi:10.1001/jama.2014.3192.

[36] Samples, John R., and Mary K. Wirtz. “Glaucoma Risk Factors: Family History – The Genetics of Glaucoma.” Clinical Glaucoma Care, 2013, pp. 45–56., doi:10.1007/978-1-4614-4172-4_4.

[37] Liu, Yutao, and R Rand Allingham. “Genetics of Glaucoma.” Glaucoma, 2015, pp. 291–299., doi:10.1016/b978-0-7020-5193-7.00025-x.

[38] Roy Chowdhury, Uttio, and Michael P. Fautsch. “Intracranial Pressure and Its Relationship to Glaucoma: Current Understanding and Future Directions.” Medical Hypothesis, Discovery and Innovation in Ophthalmology 4.3 (2015): 71–80. Print.

[39] Berdahl, John P, and R Rand Allingham. “Intracranial Pressure and Glaucoma.” Current Opinion in Ophthalmology, vol. 21, no. 2, 2010, pp. 106–111., doi:10.1097/icu.0b013e32833651d8.

[40] Yokoyama, Yu, and Toru Nakazawa. “Ocular Blood Flow in Myopic Glaucoma.” Myopia and Glaucoma, 2015, pp. 97–113., doi:10.1007/978-4-431-55672-5_8.

[41] Ethier, C. Ross. “Biomechanics in Glaucoma: Insights from Computational Studies.” The Proceedings of The Computational Mechanics Conference, vol. 2009.22, 2009, doi:10.1299/jsmecmd.2009.22._-5_.

[42] Bendel, Rick E., and Janet A. Betchkal. “Glaucoma Risk Factors: Sleep Apnea and Glaucoma.” The Glaucoma Book, 2010, pp. 135–137., doi:10.1007/978-0-387-76700-0_12.

[43] Morrison, John C. “Elevated Intraocular Pressure and Optic Nerve Injury Models in the Rat.” Journal of Glaucoma, vol. 14, no. 4, 2005, pp. 315–317., doi:10.1097/01.ijg.0000169410.09258.bf.

[44] Carenini, B. Boles, and B. Brogliatti. “Intraocular Pressure as a Risk Factor in Glaucoma.” Glaucoma: Decision Making in Therapy, 1996, pp. 9–14., doi:10.1007/978-88-470-2196-9_2.

[45] Bonomi, L., and M. Marraffa. “Lowering of Intraocular Pressure in the Treatment of Glaucoma.” Glaucoma: Decision Making in Therapy, 1996, pp. 101–104., doi:10.1007/978-88-470-2196-9_18.

[46] Morgan, J. E. “Retinal Ganglion Cell Shrinkage in Glaucoma.” Journal of Glaucoma, vol. 11, no. 4, 2002, pp. 365–370., doi:10.1097/00061198-200208000-00015.

[47] Pelzel, Heather R, and Robert W Nickells. “Retinal Ganglion Cell Death in Glaucoma.” Ocular Disease, 2010, pp. 207–213., doi:10.1016/b978-0-7020-2983-7.00027-9.

[48] “Glaucoma.” Lancaster's #1 Eye Surgeons and Doctors, Your Vision Is Our Passion., Eye Associates of Lancaster Ltd, www.eyeassociateslancaster.com/glaucoma-center/.

[49] “Glaucoma Newtown, Glaucoma Treatment Levittown, Total Eye Care.” Total Eye Care Centers, www.totaleyecarecenters.com/comprehensive-eye-care-levittown/glaucoma/.

[50] Agarwal, Renu et al. “Current Concepts in the Pathophysiology of Glaucoma.” Indian Journal of Ophthalmology 57.4 (2009): 257–266. PMC. Web. 19 Aug. 2018.

[51] Gemenetzi, M, et al. “Current Concepts on Primary Open-Angle Glaucoma Genetics: a Contribution to Disease Pathophysiology and Future Treatment.” Eye, vol. 26, no. 3, 2011, pp. 355–369., doi:10.1038/eye.2011.309.

[52] Hernández, Rodolfo, et al. “Screening for Open Angle Glaucoma: Systematic Review of Cost-Effectiveness Studies.” Journal of Glaucoma, vol. 17, no. 3, 2008, pp. 159–168., doi:10.1097/ijg.0b013e31814b9693.

[53] Erdurmus, Mesut, and Ramazan Yagci. “Dynamic Contour Tonometer Versus Goldmann Applanation Tonometer.” Journal of Glaucoma, vol. 15, no. 5, 2006, p. 471., doi:10.1097/01.ijg.0000212266.34982.79.

[54] Annette, Hager, et al. “Effect of Central Corneal Thickness and Corneal Hysteresis on Tonometry as Measured by Dynamic Contour Tonometry, Ocular Response Analyzer, and Goldmann Tonometry in Glaucomatous Eyes.” Journal of Glaucoma, vol. 17, no. 5, 2008, pp. 361–365., doi:10.1097/ijg.0b013e31815c3ad3.

[55] Giaconi, Joann A. “Glaucomas: Glaucoma and the Cornea.” Pearls of Glaucoma Management, 2009, pp. 363–369., doi:10.1007/978-3-540-68240-0_47.

[56] Spoerl, Eberhard, et al. “Age-Dependent Correction Factors for Goldmann Tonometry.” Journal of Glaucoma, 2012, p. 1., doi:10.1097/ijg.0b013e318252d382.

[57] Murase, Hiroki, et al. “Effects of Corneal Thickness on Intraocular Pressure Measured with Three Different Tonometers.” Japanese Journal of Ophthalmology, vol. 53, no. 1, 2009, pp. 1–6., doi:10.1007/s10384-008-0621-z.

[58] Burr JM, Botello-Pinzon, Takwiongi Y, et al. “Surveillance for Ocular Hypertension: An Evidance Synthesis and Economic Evaluation. Chapter 5: Agreement and reliability of candidate tonometers for measuring intraocular pressure.”

[59] Rapuano, Christopher J. “Increased Corneal Thickness in Patients With Ocular Hypertension.” Evidence-Based Eye Care, vol. 2, no. 4, 2001, pp. 220–221., doi:10.1097/00132578-200110000-00017.

[60] Ramdas, Wishal D. “Lifestyle and Risk of Developing Open-Angle Glaucoma.” Archives of Ophthalmology, vol. 129, no. 6, 2011, p. 767., doi:10.1001/archophthalmol.2010.373.

[61] Seibold, Leonard K, and Malik Kahook. “The Diurnal and Nocturnal Effects of Travoprost in Normal-Tension Glaucoma.” Clinical Ophthalmology, 2014, p. 2189., doi:10.2147/opth.s73125.

[62] Aptel, Florent, et al. “24-Hour Intraocular Pressure Rhythm in Patients With Untreated Primary Open Angle Glaucoma and Effects of Selective Laser Trabeculoplasty.” Journal of Glaucoma, vol. 26, no. 3, 2017, pp. 272–277., doi:10.1097/ijg.0000000000000604.

[63] Mansouri, K, and R Weinreb. “Continuous 24-Hour Intraocular Pressure Monitoring for Glaucoma - Time for a Paradigm Change.” Swiss Medical Weekly, 2012, doi:10.4414/smw.2012.13545.

[64] Coleman, Anne L, and Gergana Kodjebacheva. “Risk Factors for Glaucoma Needing More Attention.” The Open Ophthalmology Journal 3 (2009): 38–42. PMC. Web. 19 Aug. 2018.

[65] “Living With Glaucoma.” Glaucoma Research Foundation, www.glaucoma.org/treatment/questions-and-answers-living-with-glaucoma.php.

[66] Hughes, Edward, et al. “24-Hour Monitoring of Intraocular Pressure in Glaucoma Management: A Retrospective Review.” Journal of Glaucoma, vol. 12, no. 3, 2003, pp. 232–236., doi:10.1097/00061198-200306000-00009.

[67] Katuri, Kalyan C., et al. “Intraocular Pressure Monitoring Sensors.” IEEE Sensors Journal, vol. 8, no. 1, 2008, pp. 9–16., doi:10.1109/jsen.2007.912539.

[68] Yu, Lawrence, et al. “Chronically Implanted Pressure Sensors: Challenges and State of the Field.” Sensors, vol. 14, no. 11, 2014, pp. 20620–20644., doi:10.3390/s141120620.

[69] Goebel, Katja, et al. “A Continuous Monitoring of Fluctuations of the Intraocular Pressure with the Triggerfish Contact Lens.” SciVee, 2012, doi:10.4016/47447.01.

[70] Koutsonas, Antonis, et al. “Long-Term Follow-up after Implantation of a Telemetric Intraocular Pressure Sensor in Patients with Glaucoma: A Safety Report.” Clinical & Experimental Ophthalmology, vol. 46, no. 5, 2017, pp. 473–479., doi:10.1111/ceo.13100.

[71] Dunbar, Grace E, Bailey Yuguan Shen, and Ahmad A. Aref. “The Sensimed Triggerfish Contact Lens Sensor: Efficacy, Safety, and Patient Perspectives.” Clinical Ophthalmology (Auckland, N.Z.) 11 (2017): 875–882. PMC. Web. 19 Aug. 2018.

[72] Hubanova, Ralitsa, et al. “Effect of Overnight Wear of the Triggerfish®Sensor on Corneal Thickness Measured by Visante®Anterior Segment Optical Coherence Tomography.” Acta Ophthalmologica, vol. 92, no. 2, 2013, doi:10.1111/aos.12241.

[73] Chen, Guo-Zhen, et al. “Capacitive Contact Lens Sensor for Continuous Non-Invasive Intraocular Pressure Monitoring.” Sensors and Actuators A: Physical, vol. 203, 2013, pp. 112–118., doi:10.1016/j.sna.2013.08.029.

[74] Mansouri, K., and T. Shaarawy. “Continuous Intraocular Pressure Monitoring with a Wireless Ocular Telemetry Sensor: Initial Clinical Experience in Patients with Open Angle Glaucoma.” British Journal of Ophthalmology, vol. 95, no. 5, 2011, pp. 627–629., doi:10.1136/bjo.2010.192922.

[75] Huang, Yu-Chieh, et al. “A Contact Lens Sensor System with a Micro-Capacitor for Wireless Intraocular Pressure Monitoring.” 2013 Ieee Sensors, 2013, doi:10.1109/icsens.2013.6688174.

[76] Salvetat, Maria Letizia, et al. “Newer Intraocular Pressure Measurement Techniques.” Glaucoma - Intraocular Pressure and Aqueous Dynamics, 2016, doi:10.5772/66260.

[77] “Sensimed AG.” Resource Center, BioTech Gate, Apr. 2010, resourcecenter.biotechgate.com/wp-content/uploads/2011/08/is_sensimed.pdf.

[78] Smedt, Stefan De. “Noninvasive Intraocular Pressure Monitoring: Current Insights.” Clinical Ophthalmology, 2015, p. 1385., doi:10.2147/opth.s53772.

[79] Antonis Koutsonas, Peter Walter, Gernot Roessler, Niklas Plange; Implantation of a Novel Telemetric Intraocular Pressure Sensor in Patients With Glaucoma (ARGOS Study): 1-Year Results. Invest. Ophthalmol. Vis. Sci. 2015;56(2):1063-1069. doi: 10.1167/iovs.14-14925.

[80] “24-Hour IOP Monitoring: Current State and Future Directions.” Ophthalmology Management, 1 Mar. 2018, www.ophthalmologymanagement.com/supplements/2018/march-2018/glaucoma-physician/24-hour-iop-monitoring-current-state-and-future-d.

[81] “The Solution: EYEMATE.” IOP Implandata Ophthalmic Products GmbH, implandata.com/en/was-wir-machen/eyemate/.

[82] “EYEMATE Implantable Continuous Intraocular Pressure Monitor Validated in Initial Patients.” Medgadget, Medgadget, 17 Nov. 2017, www.medgadget.com/2017/11/eyemate-implantable-continuous-intraocular-pressure-monitor-validated-initial-patients.html.

[83] Mokwa, W., and U. Schnakenberg. “Micro-Transponder Systems for Medical Applications.” IEEE Transactions on Instrumentation and Measurement, vol. 50, no. 6, 2001, pp. 1551–1555., doi:10.1109/19.982943.

[84] Mokwa, W. “Medical Implants Based on Microsystems.” Measurement Science and Technology, vol. 18, no. 5, 2007, doi:10.1088/0957-0233/18/5/r01.

[85] Varel, Cagdas, et al. “Packaging for a Wireless Intraocular Pressure Sensor with a Solder-Filled Microchannel Antenna.” 2012 IEEE 25th International Conference on Micro Electro Mechanical Systems (MEMS), 2012, doi:10.1109/memsys.2012.6170350.

[86] Chow, Eric Y., et al. “A Miniature-Implantable RF-Wireless Active Glaucoma Intraocular Pressure Monitor.” IEEE Transactions on Biomedical Circuits and Systems, vol. 4, no. 6, 2010, pp. 340–349., doi:10.1109/tbcas.2010.2081364.

[87] Stangel, K., et al. “A Programmable Intraocular CMOS Pressure Sensor System Implant.” IEEE Journal of Solid-State Circuits, vol. 36, no. 7, 2001, pp. 1094–1100., doi:10.1109/4.933466.

[88] Chen, Lisa Y., et al. “Continuous Wireless Pressure Monitoring and Mapping with Ultra-Small Passive Sensors for Health Monitoring and Critical Care.” Nature Communications, vol. 5, no. 1, 2014, doi:10.1038/ncomms6028.

[89] Xue, Ning, et al. “A SU-8-Based Microfabricated Implantable Inductively Coupled Passive RF Wireless Intraocular Pressure Sensor.” Journal of Microelectromechanical Systems, vol. 21, no. 6, 2012, pp. 1338–1346., doi:10.1109/jmems.2012.2206072.

[90] Rosengren, Lars, et al. “A System for Passive Implantable Pressure Sensors.” Sensors and Actuators A: Physical, vol. 43, no. 1-3, 1994, pp. 55–58., doi:10.1016/0924-4247(93)00664-p.

[91] Ghannad-Rezaie, Mostafa, et al. “A Near-Infrared Optomechanical Intracranial Pressure Microsensor.” Journal of Microelectromechanical Systems, vol. 21, no. 1, 2012, pp. 23–33., doi:10.1109/jmems.2011.2171322.

[92] Santos, J. L., et al. “Optical Fiber Sensing with a Low-Finesse Fabry–Perot Cavity.” Applied Optics, vol. 31, no. 34, 1992, p. 7361., doi:10.1364/ao.31.007361.

[93] Eaton, W.p., and J.h. Smith. “Planar Surface-Micromachined Pressure Sensor with a Sub-Surface, Embedded Reference Pressure Cavity.” 1996, doi:10.2172/373935.

[94] Lee, Jeong Oen, et al. “Intraocular Sensors: Biocompatible Multifunctional Black-Silicon for Implantable Intraocular Sensor (Adv. Healthcare Mater. 4/2017).” Advanced Healthcare Materials, vol. 6, no. 4, 2017, doi:10.1002/adhm.201770017.

[95] Ghaed, Mohammad Hassan, et al. “Circuits for a Cubic-Millimeter Energy-Autonomous Wireless Intraocular Pressure Monitor.” IEEE Transactions on Circuits and Systems I: Regular Papers, vol. 60, no. 12, 2013, pp. 3152–3162., doi:10.1109/tcsi.2013.2265973.

[96] Rizq, R. N. “Intraocular Pressure Measurement at the Choroid Surface: a Feasibility Study with Implications for Implantable Microsystems.” British Journal of Ophthalmology, vol. 85, no. 7, 2001, pp. 868–871., doi:10.1136/bjo.85.7.868.

[97] Araci, Ismail E, et al. “An Implantable Microfluidic Device for Self-Monitoring of Intraocular Pressure.” Nature Medicine, vol. 20, no. 9, 2014, pp. 1074–1078., doi:10.1038/nm.3621.

[98] Chen, Po-Jui, et al. “Implantable Micromechanical Parylene-Based Pressure Sensors for Unpowered Intraocular Pressure Sensing.” Journal of Micromechanics and Microengineering, vol. 17, no. 10, 2007, pp. 1931–1938., doi:10.1088/0960-1317/17/10/002.

[99] Chen, Po-Jui, et al. “Microfabricated Implantable Parylene-Based Wireless Passive Intraocular Pressure Sensors.” Journal of Microelectromechanical Systems, vol. 17, no. 6, 2008, pp. 1342–1351., doi:10.1109/jmems.2008.2004945.

[100] Chen, Po-Jui, et al. “Spiral-Tube Parylene Intraocular Pressure Sensor.” 18th IEEE International Conference on Micro Electro Mechanical Systems, 2005. MEMS 2005., doi:10.1109/memsys.2005.1453929.

[101] Ghannad-Rezaie, M., et al. “A Powerless Optical Microsensor for Monitoring Intraocular Pressure with Keratoprostheses.” 2013 Transducers & Eurosensors XXVII: The 17th International Conference on Solid-State Sensors, Actuators and Microsystems, 2013, doi:10.1109/transducers.2013.6627365.

[102] Ghannad-Rezaie, Mostafa, et al. “A Near-Infrared Optomechanical Intracranial Pressure Microsensor.” Journal of Microelectromechanical Systems, vol. 21, no. 1, 2012, pp. 23–33., doi:10.1109/jmems.2011.2171322.

[103] Lee, Jeong Oen, et al. “Intraocular Sensors: Biocompatible Multifunctional Black-Silicon for Implantable Intraocular Sensor (Adv. Healthcare Mater. 4/2017).” Advanced Healthcare Materials, vol. 6, no. 4, 2017, doi:10.1002/adhm.201770017.

[104] Lee, Jeong Oen. “In Vivo Intraocular Pressure Measurements Using a Miniaturized Nanophotonics-Enhanced Sensor Implant.” 2016 Progress in Electromagnetic Research Symposium (PIERS), 2016, doi:10.1109/piers.2016.7735483.

[105] Wax, Adam. “Detecting Pre-Cancerous Cells Using Angle-Resolved Low Coherence Interferometry.” Biomedical Topical Meeting, 2004, doi:10.1364/bio.2004.sf1.

[106] Tan, Sanwu, et al. “Head/Tape Spacing Measurements for Digital Linear Tape Drives Using Three-Color Interferometry.” Tribology Transactions, vol. 43, no. 1, 2000, pp. 144–150., doi:10.1080/10402000008982324.

[107] Hastings, Jeffrey Todd, E. Britt Brockman, Ingrid L. St. Omer, and John C. Wright. System, Device, and Method for Determination of Intraocular Pressure. Brockman Holdings LLC, The University of Kentucky Research Foundation, assignee. Patent US 20110160561 A1. 30 June 2011. Print.

[108] Totsu, Kentaro, et al. "Ultra-Miniature Fiber-Optic Pressure Sensor Using White Light Interferometry." Journal of Micromechanics and Microengineering, vol. 15, no. 1, 2004, pp. 71–75., doi:10.1088/0960-1317/15/1/011.

[109] Givens, Miles Parker. Interferometry. Institute of Optics, the University of Rochester, 1967.

[110] Gilbert, Zoe. Researcher's Guide to Interferometry. Clanrye Intl, 2015.

[111] Brunner, Thomas. "Curing Glaucoma: A Video Message from the President." Glaucoma Research Foundation, www.glaucoma.org/about/curing-glaucoma-a-video-message-from-the-president.php.

[112] Tham, Yih-Chung, et al. "Global Prevalence of Glaucoma and Projections of Glaucoma Burden through 2040." Ophthalmology, vol. 121, no. 11, 2014, pp. 2081–2090., doi:10.1016/j.ophtha.2014.05.013.

[113] Born, Max, et al. Principles of Optics Electromagnetic Theory of Propagation, Interference and Diffraction of Light. Cambridge Univ. Press, 2016.

[114] Heavens, Oliver S., and Robert W. Ditchburn. Insight into Optics. Wiley, 1993.

[115] Bradt, Hale. "Multiple Telescope Interferometry." Astronomy Methods, pp. 175–217., doi:10.1017/cbo9780511802188.008.

[116] Mcmillan, T.c., and F.e. Talke. "An Investigation of the 'Take-Off' Characteristics Of Tri-Pad Sliders Using Phase Demodulated Laser Interferometry." 1997 IEEE International Magnetics Conference, doi:10.1109/intmag.1997.597410.

[117] Brezinski, Mark E. "Optical Coherence Tomography Theory." Optical Coherence Tomography, 2006, pp. 97–145., doi:10.1016/b978-012133570-0/50007-x.

[118] Wang, Tongzhou Wang Tongzhou, et al. "Label-Free Biomolecular Imaging Using Scanning Spectral Interferometry." Chinese Optics Letters, vol. 11, no. 11, 2013, pp. 111102–111105., doi:10.3788/col201311.111102.

[119] "WYKO 400 Interferometer." Precision Engineering, vol. 15, no. 4, 1993, p. 291., doi:10.1016/0141-6359(93)90118-t.

[120] Wolfle, David Henry. Types of Interferometers. 1905.

[121] Hariharan, P., “Basics of Interferometry,” Elsevier, 1991., doi: 10.1016/B978-0-12-373589-8.X5000-7

[122] Gohdssi, R., and Pinyen, L. *MEMS Material an processes*, 1st editio ed. Springer New York Dordrecht Heidelberg London, 2010.

[123] Goodwin, E., and Wyant, J. Interferometric Optical Testing. Field Guide to Interferometric Optical Testing (2006), 1–10.

[124] Paschotta, Rüdiger. “Coherence.” *Encyclopedia of Laser Physics and Technology - Quantum Cascade Lasers, QCL, Mid-Infrared, Terahertz, Semiconductor Lasers*, 13 June 2018, www.rp-photonics.com/coherence.html.

[125] Tanito, Masaki, et al. “Different Glaucoma Types and Glaucoma Surgeries among Different Age Groups.” Graefe's Archive for Clinical and Experimental Ophthalmology, 2018, doi:10.1007/s00417-018-4058-x.

[126] “What Are the Types of Glaucoma?” Johns Hopkins Medicine Health Library, www.hopkinsmedicine.org/wilmer/services/glaucoma/book/chapter_types_of_glaucoma.html.

[127] Balavalad, Kirankumar & Sheeparamatti, Basavaprabhu. (2015). A Critical Review of MEMS Capacitive Pressure Sensors. Sensors & Transducers. 187. 120-128.

[128] Norcada. Thin-film Silicon-Nitride Microscopy Windows Specification Sheet, 2018.

[129] Morrison, John C. “Elevated Intraocular Pressure and Optic Nerve Injury Models in the Rat.” Journal of Glaucoma, vol. 14, no. 4, 2005, pp. 315–317., doi:10.1097/01.ijg.0000169410.09258.bf.

[130] Carenini, B. Boles, and B. Brogliatti. “Intraocular Pressure as a Risk Factor in Glaucoma.” Glaucoma: Decision Making in Therapy, 1996, pp. 9–14., doi:10.1007/978-88-470-2196-9_2.

[131] Bonomi, L., and M. Marraffa. “Lowering of Intraocular Pressure in the Treatment of Glaucoma.” Glaucoma: Decision Making in Therapy, 1996, pp. 101–104., doi:10.1007/978-88-470-2196-9_18.

[132] Khakpour, Reza & Rastegar, Solmaz & Bahadorimehr, Alireza. (2010). Analytical comparison for square, rectangular and circular diaphragms in MEMS applications. 2010 International Conference on Electronic Devices, Systems and Applications, ICEDSA 2010 - Proceedings. 10.1109/ICEDSA.2010.5503057.

[133] Tilli, Markku. Handbook of Silicon Based MEMS Materials and Technologies. Elsevier, William Andrew, 2015.

[134] Microfabrication of large-area circular high-stress silicon nitride membranes for optomechanical applications

[135] Eaton, W. P., Bitsie, F., Smith, J. H., and Plummer, D. W. A New Analytical Solution for Diaphragm Deflection and its Application to a Surface-Micromachined Pressure Sensor. *Technical Proceedings of the 1999 International Conference on Modelling and Simulations of Microsystems*, 4 (1999), 640–643.

[136] Jindal, Sumit Kumar, and Sanjeev Kumar Raghuwanshi. "A Complete Analytical Model for Circular Diaphragm Pressure Sensor with Freely Supported Edge." *Microsystem Technologies*, vol. 21, no. 5, 2014, pp. 1073–1079., doi:10.1007/s00542-014-2144-5.

[137] Rahman, Md Mosaddequr, and Sazzadur Chowdhury. "Square Diaphragm CMUT Capacitance Calculation Using a New Deflection Shape Function." *Journal of Sensors*, vol. 2011, 2011, pp. 1–12., doi:10.1155/2011/581910.

[138] S. D. Senturia, *Microsystems Design*, Kluwer Academic, Norwell, Mass, USA, 2000.

[139] Guldin, S. 2013, Inorganic Nanoarchitectures by Organic Self-Assembly (Switzerland: Springer International Publishing)

[140] Vora, K. D., et al. "Fabrication of Support Structures to Prevent SU-8 Stiction in High Aspect Ratio Structures." *Microsystem Technologies*, vol. 13, no. 5-6, 2006, pp. 487–493., doi:10.1007/s00542-006-0201-4.

[141] Barber R L, Ghantasala M K, Divan R, Mancini D C and Harvey E C 2007 Study of stress and adhesion in SU-8 resist layers on silicon substrate *J. Micro/Nanolithogr. MEMS MOEMS* **6** 033006

[142] Hill, G.c., et al. "SU-8 MEMS Fabry-Perot Pressure Sensor." *Sensors and Actuators A: Physical*, vol. 138, no. 1, 2007, pp. 52–62., doi:10.1016/j.sna.2007.04.047.

[143] F. Niklaus, P. Enoksson, E. Kalvesten, G. Stemme, Low-temperature full wafer adhesive bonding, J. Micromech. Microeng. 11 (2001) 100-107.

[144] Yu, Liming, et al. "Adhesive Bonding with SU-8 at Wafer Level for Microfluidic Devices." *Journal of Physics: Conference Series*, vol. 34, 2006, pp. 776–781., doi:10.1088/1742-6596/34/1/128.

[145] Conradie E H and Moore D F 2002 SU-8 thick photoresist processing as a functional material for MEMS applications *J. Micromech. Microeng.* **12** 368–74

[146] Hwang K Y, Park C S, Kim J H, Suh K Y, Cho E C and Huh N 2010 The effects of adhesion energy on the fabrication of high-aspect-ratio SU-8 microstructures *J. Micromech. Microeng.* **20** 117001

[147] Norcada. Thin-film Silicon-Nitride Microscopy Windows Specification Sheet, 2018.

[148] Zeniieh, Dani, et al. "Parylene-C as High Performance Encapsulation Material for Implantable Sensors." *Procedia Engineering*, vol. 87, 2014, pp. 1398–1401., doi:10.1016/j.proeng.2014.11.704.

[149] Lee, A., et al. "Fabrication of Slender Elastic Shells by the Coating of Curved Surfaces." *Nature Communications*, vol. 7, 2016, p. 11155., doi:10.1038/ncomms11155.

[150] Phan, Alex, et al. "Design of an Optical Pressure Measurement System for Intraocular Pressure Monitoring." *IEEE Sensors Journal*, vol. 18, no. 1, 2018, pp. 61–68., doi:10.1109/jsen.2017.2767539.

[151] *Laser Safety Facts*, www.lasersafetyfacts.com/laserclasses.html.

[152] Chhablani, Jay, Simon Kaja, and Vinay A Shah. "Smartphones in Ophthalmology." *Indian Journal of Ophthalmology* 60.2 (2012): 127–131. *PMC*. Web. 20 Aug. 2018.

[153] SMith, Scott D. "Anterior Segment OCT and Angle Closure." *Review of Ophthalmology*, 17 July 2007, www.reviewofophthalmology.com/article/anterior-segment-oct-and-angle-closure.

[154] "Cataracts." *National Eye Institute*, U.S. Department of Health and Human Services, nei.nih.gov/eyedata/cataract.

[155] "How To Improve Your Odds Of Successful Cataract Surgery." *LifeExtension.com*, www.lifeextension.com/magazine/2015/11/how-to-improve-your-odds-of-successful-cataract-surgery/page-01.

[156] *VisioNavigaid Phacoemulsification*, www.visionavigaid.com/index.php?page_name=phacoemulsification&page_id=1198.

[157] Eleftheriadis, H. "Interlenticular Opacification in Piggyback AcrySof Intraocular Lenses: Explantation Technique and Laboratory Investigations." *British Journal of Ophthalmology*, vol. 85, no. 7, 2001, pp. 830–836., doi:10.1136/bjo.85.7.830.

[158] Hennig, A, et al. "Foldable vs Rigid Lenses after Phacoemulsification for Cataract Surgery: a Randomised Controlled Trial." *Eye*, vol. 28, no. 5, 2014, pp. 567–575., doi:10.1038/eye.2014.26.

[159] Hara, T, et al. "Equator ring for maintenance of the completely circular contour of the capsular bag equator after cataract removal." *Ophthalmic Surg.* 1991 Jun; 22(6):358-9.

[160] Tribus, Claudia et al. "Indications and Clinical Outcome of Capsular Tension Ring (CTR) Implantation: A Review of 9528 Cataract Surgeries." *Clinical ophthalmology (Auckland, N.Z.)* 1.1 (2007): 65–69. Print.

[161] Ma, Xiao, and Zhaohui Li. "Capsular Tension Ring Implantation after Lens Extraction for Management of Subluxated Cataracts." *International Journal of Clinical and Experimental Pathology* 7.7 (2014): 3733–3738. Print.

[162] Nakakura, Shunsuke. "Icare® Rebound Tonometers: Review of Their Characteristics and Ease of Use." *Clinical Ophthalmology,* Volume 12, 2018, pp. 1245–1253., doi:10.2147/opth.s163092.

[163] Ma, Di, et al. "Repeatability, Reproducibility and Agreement of Intraocular Pressure Measurement in Rabbits by the TonoVet and Tono-Pen." *Scientific Reports*, vol. 6, no. 1, 2016, doi:10.1038/srep35187.

[164] Zhang, Hong, et al. "Validation of Rebound Tonometry for Intraocular Pressure Measurement in the Rabbit." *Experimental Eye Research*, vol. 121, 2014, pp. 86–93., doi:10.1016/j.exer.2014.02.004.

[165] Löbler, Marian, et al. "Suitability and Calibration of a Rebound Tonometer to Measure IOP in Rabbit and Pig Eyes." Veterinary Ophthalmology, vol. 14, no. 1, 2011, pp. 66–68., doi:10.1111/j.1463-5224.2010.00794.x.

[166] Medexsupply.com - Alcon Monarch II IOL Delivery System

[167] Maloney, John M., et al. "In Vivo Biostability of CVD Silicon Oxide and Silicon Nitride Films." *MRS Proceedings*, vol. 872, 2005, doi:10.1557/proc-872-j14.3.